Master's thesis

NTNU
Norwegian University of Science and Technology
Faculty of Information Technology and Electrical Engineering
Department of Electric Power Engineering

Arne Filip Nygaard

Optimization of Zero-Emission Power Devices for an Electric Aircraft

Master's thesis in Energy and Environmental Engineering
Supervisor: Roy Nilsen
Co-supervisor: Kristen Wagelid Jomås
June 2021

NTNU
Norwegian University of Science and Technology

Arne Filip Nygaard

Optimization of Zero-Emission Power Devices for an Electric Aircraft

Master's thesis in Energy and Environmental Engineering
Supervisor: Roy Nilsen
Co-supervisor: Kristen Wagelid Jomås
June 2021

Norwegian University of Science and Technology
Faculty of Information Technology and Electrical Engineering
Department of Electric Power Engineering

NTNU
Norwegian University of
Science and Technology

Preface

This is a Master's thesis at NTNU as part of the study program Energy and Environmental Engineering at the Department of Electric Power Engineering. The work was carried out during the spring semester of 2021 in collaboration with Rolls-Royce Electrical Norway AS (RREN). This thesis is a continuation of the specialization project performed during the autumn semester of 2020. The initial request from RREN was to investigate power balancing and switching conditions of fuel cells, batteries and supercapacitors in a typical hybrid-electrical flight operation. The problem description was further developed in collaboration with Prof. Roy Nilsen and RREN.

I would like to thank my supervisor Prof. Roy Nilsen from NTNU and co-supervisor Kristen Wagelid Jomås from RREN for their guidance throughout the project. Their knowledge and industry experience have been valuable and helped making reasonable assumptions for the thesis. I greatly appreciate the participation and contributions from Kristen Wagelid Jomås, Andrea Bocchese and Børge Noddeland from RREN and Simon Clark and Michael Gerhardt from SINTEF Industry related to our bi-weekly meetings and discussions throughout the work.

As an electrical engineer, it has been both interesting and challenging exploring new academic fields such as electrochemistry and aeronautics. Particularly, getting into the complexity of fuel cell systems has been demanding. The competence of Simon Clark and Michael Gerhardt have been very helpful in this context. Similarly, Andrea Bocchese has contributed with valuable insight on basic flight mechanics. Hopefully, this work can enlighten some of the key opportunities and challenges we face in the transition towards zero-emission aviation. The thesis is primarily targeting researchers and industry within fuel cell-electric transport, and aviation applications in particular. The reader is assumed to possess fundamental knowledge within electrical engineering and electrochemistry.

Stavanger, 2021-06-21

Arne Filip Nygaard

Abstract

To reach the climate goals of carbon neutrality within 2050, also the aviation sector must replace fossil fuels with more sustainable alternatives. By utilizing fuel cell-powered propulsion systems, the climate impact will be reduced to a minimum. Proton exchange membrane fuel cells are currently regarded as one of the most economic and climate-friendly options for the electrification of the commuter and regional aircraft segments. There exists several aircraft projects combining such fuel cells with batteries in hybrid energy systems. These power devices should be optimized to meet the strict aircraft requirements and compete with conventional propulsion systems.

Fundamental theory on the fuel cell and its surrounding components are investigated to form the foundation of this work. In order to perform an accurate optimization, numerical models of the power devices have be developed to represent appropriate high-performance devices. Similarly, the power profiles of specific flight missions have been modelled based on logging data from a regional, reference aircraft. Four flight missions were investigated and a 526 km route was used as the reference profile. By utilizing these models, the power requirements, the energy consumption and the operational conditions of the fuel cell and the battery are dynamically updated to find the optimal power balancing. The key performance indicators are restricted to the weight and costs of the power devices and the hydrogen fuel. A voltage and temperature-driven degradation model is used to estimate the fuel cell lifetime based on how the device is operated for different sizing scenarios. This lifetime is used to calculate the total investment costs based on the number of required reinvestments throughout a time period of 15 years. By calculating the corresponding battery investments and fuel costs, based on the level of hybridization and the fuel cell oversizing, the optimal costs can be estimated. For weight optimization, also the hydrogen tank and the heat exchanger requirements are included. In order to combine the economic and technical performance indicators, the costs are weighted against an estimated aircraft payload capacity. Increasing the energy system weight will, thus, limit the available capacity for passengers. The optimal sizing and hybridization can be seen as the case that gives the lowest total costs per available seat.

Little differences were found between a fuel cell only configuration and the combination with small battery packs for power boosting, neither in terms of weight or costs. For the most promising hybridization cases, a FC oversizing of 40-60% was found optimal. Improvements in the FC performance were also found to be possible by increasing the platinum loading in the cells. For the 526 km reference flight, weighted costs of the fuel cell only configuration were found to be optimal. Hybridization with 10% and 20% battery power gave 0.3% and 1.7% higher weighted costs, respectively. The corresponding numbers were 2.3% and 6.5% for a shorter flight of 187 km. Contrarily, a longer flight of 1093 km found its optimality in an 80% fuel cell and 20% battery

power share, with a 4% reduction compared to fuel cell only-propulsion.

To enable further conclusions, the faster dynamics, switching conditions and response time of the energy system are discussed with basis in existing literature and basic tests in Simulink®. Based on a literature research, the high frequency ripple currents caused by the switching of power electronic converters are found to be of negligible concern for the fuel cell performance, compared to the impact of slower dynamics. Fuel cell systems are likely to be capable of meeting key aircraft response time requirements, but may operate more efficiently if hybridized with batteries or other faster-responding devices. With these remarks, the 80% fuel cell and 20% battery hybridization, with a 56% fuel cell oversizing, is suggested to be the most promising overall alternative for the regional aircraft segment with the given power devices.

Sammendrag

For å nå klimamålene om karbonnøytralitet innen 2050, må også luftfartssektoren erstatte fossilt drivstoff med mer bærekraftige alternativer. Flyindustrien viser spesiell interesse for hydrogen på grunn av grunnstoffets høye gravimetriske energitetthet. Ved å benytte brenselcelle-drevne fremdriftssystemer, vil klimapåvirkningen bli redusert til et minimumsnivå. Brenselceller med protonledende membraner, såkalte PEM brenselceller, fremstår som den mest lovende brenselcelle-teknologien for kortdistanse og regionale passasjerfly. Det pågår flere flyprosjekter hvor brenselceller kombineres med batterier i hybridsystemer. Kombinasjonen av disse kraftkildene bør optimeres for å tilfredsstille strenge flykrav og konkurrere med konvensjonelle fremdriftssystemer.

Grunnleggende teori knyttet til brenselcelle-systemer er presentert for å legge grunnlaget for oppgaven. For å kunne utføre en nøyaktig optimalisering, har numeriske modeller for kraftkildene blitt utviklet for å representere høyytelses-enheter. På samme måte har kraftprofilene knyttet til spesifikke flyvninger blitt modellert basert på loggdata fra et regionalt referansefly. Fire ulike flyruter er undersøkt, hvorav en 526 km lang rute er brukt som referanseflyvning. Ved å bruke disse modellene kan kraftbehovet, energibruken og driftsforholdene for brenselcella og batteriet oppdateres dynamisk for å finne den optimale kraftfordelingen. Nøkkelindikatorer er begrenset til vekt og kostnader knyttet til kraftkildene og drivstoff. En spenning- og temperaturavhengig levetidsmodell er brukt for å estimere brenselcellas levetid basert på hvordan den er lastet for ulike scenarioer. Denne levetiden brukes til å beregne de totale investeringskostnadene basert på den nødvendige antallet reinvesteringer i løpet av analyseperioden på 15 år. Ved å beregene de tilsvarende batteri-investeringene og drivstoffkostnadene, basert på graden av hybridisering og overdimensjonering av brenselcella, kan de totale kostnadene bli estimert. For optimalisering på vekt vil også hydrogentanken og varmeveksler-behovet blir inkludert. For å kombinere økonomiske og tekniske nøkkelindikatorer kan kostnadene blir vektet mot en estimert nyttelastkapasitet. En økende vekt på energisystemet vil begrense denne kapasiteten og dermed begrense antallet passasjerer. Den optimale dimensjoneringen og hybridiseringen kan da uttrykkes som det scenarioet som gir lavest kostnader per tilgjengelige flysete.
Kun små forskjeller ble funnet mellom ren brenselcelledrift og hybridisering med små batterier, både for vekt og kostnader. For de mest lovende hybrid-scenarioene var en overdimensjonering av brenselcella på 40-60% optimal. Ytelsesforbedringer er også vist å være oppnåelig ved å øke platinum-innholdet i cellene. For den 526 kilometer lange referanseflyvningen var det ren brenselcelledrift som ga de laveste, vektede kostnadene. Hybridisering med 10% og 20% batterikraft ga henholdsvis 0.3% og 1.7% høyere vektede kostnader. De tilsvarende verdiene var 2.3% og 6.5% for en kortere flyvning på 187 km. I motsetning, for en flyvning på 1093 km var den en kraftfordeling på 80% for brenselcella og 20% for batteriet som ga den laveste, vektede kostnaden, med en 4% reduksjon sammenlignet med ren brenselcelle-drift.

For å muliggjøre videre konklusjoner, har høyfrekvente varisjoner, svitsjing og responstid blir diskutert i sammenheng med energisystemet basert på eksisterende litteratur og tester i Simulink®. Basert på litteraturstudier, fremstår den høyfrekvente strømrippelen fra omformere som lite bekymringsverdig for ytelsen til brenselcella, sammenlignet med tregere variasjoner. Brenselcellesystemet kan forventes å tilfredsstille flyrelaterte responstids-krav, men kan operere med høyere effektivitet hvis det er hybridisert med batterier eller andre enheter med rask responstid. Med disse bemerkningene fremstår en hybrid med 80% brenselcelle- og 20% batteri-kraft, med en 56% overdimensjonering på brenselcella, som den mest lovende kombinasjonen for regionale passasjerfly, med de gitte kraftenhetene.

Contents

Preface i
Abstract ii
Sammendrag iv

1 Introduction **2**
1.1 Background 2
1.2 Objectives 3
1.3 Approach 4
1.4 Contributions 5
1.5 Limitations 6
1.6 Outline 6

2 Theoretical Background **8**
2.1 Mission Profile 8
2.1.1 Flight Mechanics 8
2.1.2 Electric Propulsion 9
2.2 Hydrogen Storage 10
2.2.1 Compressed Hydrogen 10
2.2.2 Liquid Hydrogen 11
2.2.3 Tank Design 12
2.3 Fuel Cell Theory 13
2.3.1 Principles and Structure 13
2.3.2 Voltage Characteristics 14
2.3.3 Operating Pressure 17
2.3.4 Operating Temperature 18
2.3.5 Efficiency 18
2.3.6 Heat and Water Management 19
2.3.7 Air Compression System 22
2.3.8 Degradation and Operational Limits 24
2.3.9 Transient Characteristics 26
2.3.10 Hybridization 29

2.4 Battery Theory . . . 31
2.5 Fuel Cell Modelling . . . 32
2.6 Aircraft Powertrain . . . 33
2.6.1 Distribution System . . . 33
2.6.2 Power Electronic Converters . . . 33
2.6.3 Powertrain Topology . . . 35
2.6.4 Electrical Loads . . . 36
2.7 Investment Costs Calculation . . . 36

3 Modelling Approach **37**
3.1 Mission Profile for Regional Aircraft . . . 37
3.1.1 Reference Aircraft Specifications . . . 38
3.2 Fuel Cell Modelling . . . 40
3.2.1 Polarization Curve . . . 40
3.2.2 Lifetime Calculations . . . 43
3.2.3 Cooling System . . . 47
3.2.4 Air Compression Model . . . 51
3.3 Hydrogen Tanks Sizing . . . 54
3.4 Battery Modelling . . . 56
3.5 Energy and Power Calculation . . . 59
3.6 Powertrain Topology . . . 60
3.7 Costs Calculation . . . 61
3.7.1 Lifetime Estimations . . . 61
3.7.2 Model Parameters . . . 62
3.7.3 Cost per Available Seat Kilometer . . . 63

4 Simulation Model **65**
4.1 Power Ramp Case . . . 66
4.2 Load Loss Case . . . 66
4.3 Mission Profile Simulation . . . 66

5 Optimization Model **68**
5.1 Optimization Model Development . . . 68
5.1.1 Mass Optimization . . . 69
5.1.2 Hybridization . . . 70
5.2 Optimization Approach . . . 72
5.2.1 Optimization On Constant Power . . . 73
5.2.2 Optimization On Mission Profile . . . 74

6 Mass Optimization **77**
6.1 Optimization On Mission Profile . . . 77
6.1.1 FC Only Case . . . 77
6.1.2 Hybrid Case . . . 79
6.2 Device Characteristics . . . 81

7 Cost Optimization **85**
7.1 Lifetime and Investment Costs . . . 85
7.1.1 Investment Costs . . . 85
7.1.2 Platinum Loading . . . 87
7.2 Fuel Costs . . . 89
7.3 Cost per Available Seat Kilometer . . . 92
7.4 Actual Payload Estimation . . . 98

8 Testing and Discussion **100**
8.1 Dynamics and Response Time . . . 100
8.1.1 Power Ramp Case . . . 100
8.1.2 Load Loss Case . . . 102
8.1.3 Switching Conditions and Fast Dynamics . . . 102
8.2 Power Balancing . . . 103
8.3 Additional Discussion . . . 104

9 Conclusion **106**
9.1 Conclusion . . . 106
9.2 Recommendations for Further Work . . . 108

A Acronyms **110**

B Theoretical Background **111**
B.1 Degradation and Operational Limits . . . 111

C Modelling and Simulation **113**
C.1 Simulation Model . . . 113
C.1.1 Fuel Cell System . . . 113
C.1.2 Boost Converter . . . 117
C.1.3 Battery . . . 118
C.1.4 Mission Profile . . . 119
C.2 Lifetime Calculations . . . 119

D Optimization Results **121**
D.1 Optimization on Constant Power 121
D.2 Optimization on Mission Profile 123
D.2.1 FC Only Case 123
D.2.2 Hybrid Case 126
D.2.3 Cost per Available Seat Kilometer 129

E Simulations **131**
E.1 Power Balance Simulations 131

F Numerical Code **134**
F.1 Mission Profile Calculation 134
F.2 Optimization Scripts 136
F.2.1 Battery Sizing Script 145

Bibliography **147**

Chapter 1

Introduction

1.1 Background

Civil aviation is responsible for above 13% of the transport related CO_2 emissions in Europe [1]. This makes it the second largest source of greenhouse gas emissions within the transport sector. Other warming effects, such as the formation of condensation trails, are reported to almost double the overall impact on climate changes [2]. Noise and NO_x pollution are also unwanted side effects of direct combustion. Through the Green Deal, the EU has set a target to achieve carbon neutrality within 2050 [3]. To reach this target, also the aircraft industry must find alternatives to conventional fossil fuels.

Aviation brings different requirements than land vehicles regarding weight, size and reliability. The relatively low energy density of state-of-the-art batteries limits the application of battery-powered all-electric aircraft (AEA) to a few passengers for short-range flights [2]. Even with significant technology developments, batteries will be greatly inferior to conventional jet fuel with respect to energy density. Another concern is the limited charging capacity at airports and the corresponding risk of long downtime between flights [1]. These are important reasons why the industry has increased its engagement in hydrogen as a potential energy carrier for aviation.

Hydrogen has an energy density of about a hundred times that of state-of-the-art batteries. Recently, Airbus announced three zero-emission aircraft concepts with hydrogen as the primary energy source [4]. The conceptual designs base their propulsion on direct combustion in modified turbines. In 2020, ZeroAvia performed the first fully electric commercial-scale flight in the UK with their six-seater aircraft [5]. They base their propulsion on electricity generated from proton exchange membrane fuel cells (PEMFCs) on-board. In 2020, a fact-based study prepared by McKinsey & Company for the EU showed potentials of reducing the aviation climate impact by 50-75% with hydrogen combustion, and 75-90% with fuel cell (FC) propulsion [3]. The latter technology was found to be the most climate-friendly and economic option in the commuter

and regional aircraft segments. This work also focuses on the complete elimination of direct combustion by utilizing FCs for electric propulsion.

Two essential challenges, limiting the wide-scale commercialization of PEMFCs, are the high costs and the restricted lifetime [6]. The U.S. Department of Energy (DOE) have announced an ultimate target durability of 8000 hours and a cost of 30$/kW for fuel cell systems (FCSs) for transport applications [6]. In 2015, the reported durability and cost were 3900 hours and 53$/kW, respectively [6]. For aviation specifically, another concern is that peripheral components such as compressors, cooling systems and heavy hydrogen tanks are restricting the effective power-to-weight ratio of FC-powered propulsion systems. To achieve technically and economically competitive alternatives to conventional aircraft, these challenges must be overcome. By investigating the relevant power devices and their surrounding components, the energy system can be optimized on important key performance indicators (KPIs) such as weight and costs.

Prior studies have investigated the design and sizing of PEMFCs [7] and the hybridization with batteries [8] for medium- and long-range flight profiles. Both state-of-the-art technology and possible future developments are investigated. Also Kammermann et al. [9] presented a feasibility study for an AEA based on weight, volume and reliability requirements. The paper analyzes electric propulsion from battery and FC technologies with basis in a regional turboprop aircraft. No focus is put on the dynamic operation of the whole FCS and the implication of fast load variations and switching conditions. Neither are any non-technical KPIs considered in the optimizations, neglecting the importance of the FC costs and lifetime.

The regional aircraft segment appears to be a promising first step towards FC-powered propulsion. To supplement the scarce literature and highlight new essential aspects related to FC-powered aircraft, the design and optimization of the power devices for such applications should be more thoroughly investigated.

1.2 Objectives

To make justified decisions and substantial discussions on the energy system of a FC-powered aircraft, both qualitative and quantitative considerations must be made. Thus, the main objectives of this thesis are to:

1. Find the optimal hybridization and sizing of PEMFCs and batteries for an electric aircraft based on technical and economic considerations.

2. Investigate and test the power balancing and switching conditions of the optimal energy system.

1.3 Approach

Initially, the most relevant theory and preliminaries are presented to form the basis of the modelling and to justify important choices and assumptions. To enable valuable considerations on an appropriate mission profile, a reference aircraft has been chosen. By using flight mechanics theory and open-source logging data, power profiles and environmental conditions have been estimated for real flights carried out by this aircraft. Similarly, the power devices have been modelled based on existing, high-performance devices to achieve good compliance with state-of-the-art products. MATLAB® has been used to implement numerical models for the various components of the system. These models have also been implemented in Simulink®, enabling a more graphic representation and simplifying system changes for relevant test cases. The numerical models have been used to optimize and evaluate the power devices on some key performance indicators such as mass, lifetime and costs. A schematic overview of a possible energy and propulsion system is illustrated in Fig. 1.1.

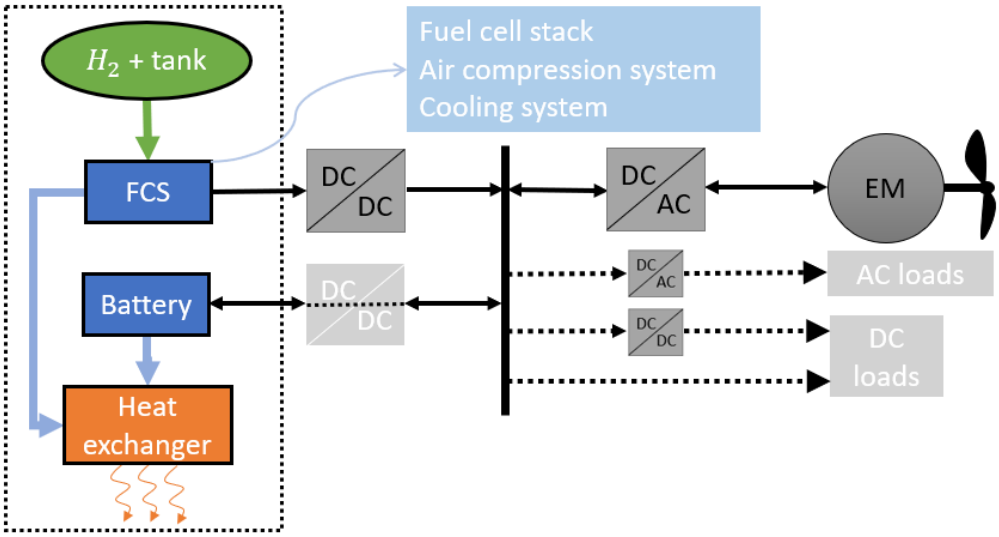

Figure 1.1: Schematic overview of the energy and propulsion system. The colored blocks within the marked area represent the hydrogen tank, the fuel cell system (FCS), the battery and the heat exchanger. These are the main components used in the optimization.

Only the colored components in the marked area are subject to the optimization algorithm. These components will be referred to as the *energy system*. The main optimization approach is illustrated by Fig. 1.2 and will be more thoroughly explained in Section 5.2.2.

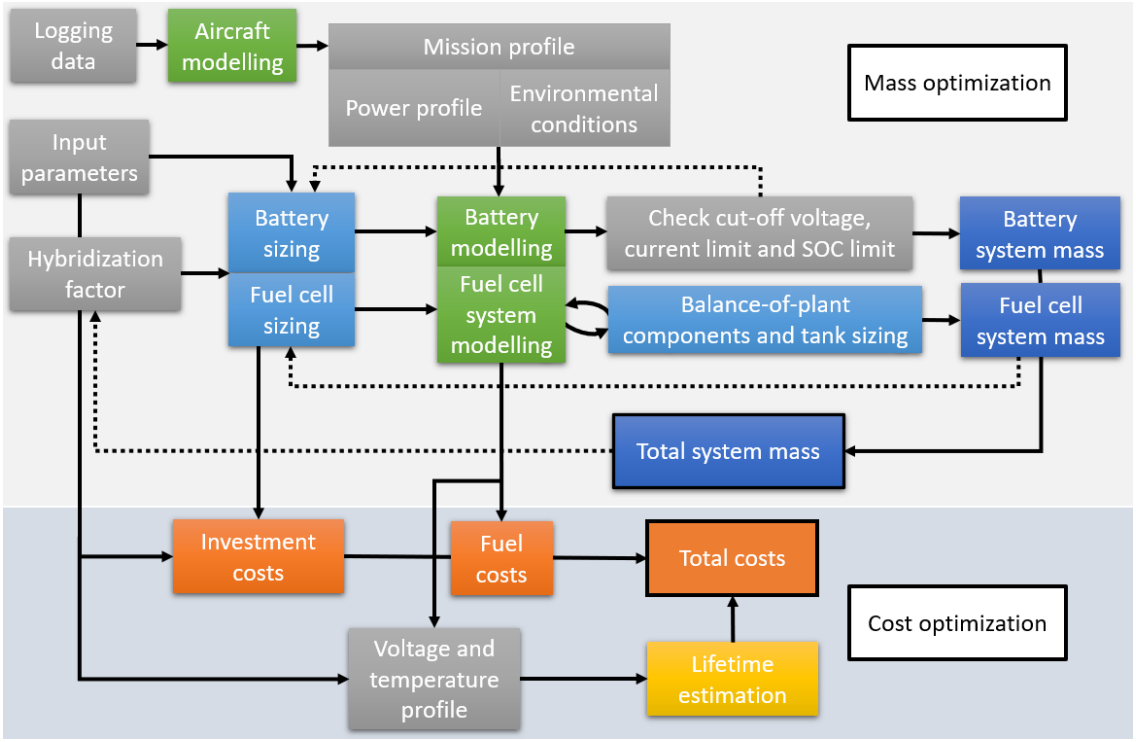

Figure 1.2: Schematic overview of the mass- and cost-optimizations.

1.4 Contributions

The main contributions of this work are listed below:

- A FC model, dynamically compatible with a semi-empirical degradation model, has been developed. The model explicitly expresses important design parameters and enables dynamic operation with changing temperature and pressure.
- Little work known to the author exists on optimization of the energy system of FC-powered aircraft. The existing literature is mainly limited to optimizations with linear power and energy densities, often neglecting the complication of balance-of-plants components, the non-linearity of hydrogen storage and the influence of heat generation. This work also makes qualitative considerations on how transient requirements and dynamic conditions may affect the system performance.
- The optimization approach enables assessment of various flight missions based on open-source logging data. Important aircraft parameters can be adjusted to model changes in the aircraft design and weight.

1.5 Limitations

Important limitations are listed below:

- **Power device optimization:** The evaluated power devices are limited to the PEMFC and lithium-ion battery technologies as they represent the industry standard in terms of FC-powered aircraft projects. For the numerical optimization of the power devices, the system topology and power electronic converters are not considered. Neither are the implications of dynamic conditions due to high uncertainty in quantified impact.
- **Mission profile:** The optimization is performed considering different specific mission profiles, rather than aircraft certification specifications.
- **Change of volume**: The change in power requirement caused by changes in volume is not considered in the optimization. This could be added by estimating an appropriate drag contribution induced by any unrestrained volume additions, but would also require specific knowledge and assumptions on the aircraft design.
- **Verification**: No experimental verification is performed. The testing and evaluation of the energy system are limited to numerical calculations, simulations and relevant literature.

1.6 Outline

Chapter 2 - Theoretical background: The most relevant theory from the preceding specialization project is supplemented with new material to form the theoretical basis of this thesis. This includes theory on flight mechanics, hydrogen storage, FCs, batteries and key components in the aircraft electrical distribution system. The main focus is on the FC theory and its balance-of-plant components.

Chapter 3 - Modelling Approach: The component modelling, key parameters and important choices are presented. When appropriate, submodel results are included to illustrate relevant concepts.

Chapter 4 - Simulation Model: The implementation of the numerical component submodels in Simulink® is presented and two basic power ramp and a load loss cases are introduced.

Chapter 5 - Optimization Model: The optimization approach used for power balancing and device sizing is presented. An effort is made to show the development from an inital model that was found to have certain shortcomings.

Chapter 6 - Mass Optimization: The optimal FC sizing and battery hybridization are investigated with respect to the mass of the energy system.

Chapter 7 - Cost Optimization: The optimal FC sizing and battery hybridization are investigated with respect to the investment costs of the power devices and the fuel costs. The technical and economic KPIs are connected by assumptions on the aircraft payload capacity. Based on the energy system mass for some of the promising cases, the actual aircraft payload capacity is estimated by comparison with the conventional reference aircraft.

Chapter 8 - Discussion and Testing: The energy system is discussed with basis in the literature and the results. A power ramp and a load loss cases are tested in Simulink®, mainly to illustrate typical transient response challenges that must be overcome by the energy system.

Chapter 2

Theoretical Background

2.1 Mission Profile

A typical flight can be divided into several phases, characterized by their thrust profile. The thrust required during takeoff and climb is significantly larger than that of the remaining flight phases, and will define the maximum power requirement of the engines [10]. Due to the relatively long time spent at cruising altitude and speed, the cruise phase will normally make up a great share of the total energy consumption, despite a lower average power. During descent, approach and landing phases the power requirement will normally decrease further [8, 10].

2.1.1 Flight Mechanics

The motion of an aircraft can be described by the forces acting in the vertical and the horizontal directions, as depicted in Fig. 2.1. The thrust, T, represents the propulsive force of the propellers, while G, F_D and F_L represent the gravitational force, the drag force and the lift force, respectively.

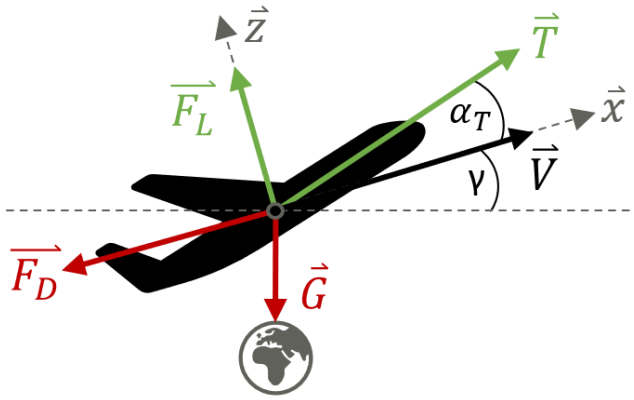

Figure 2.1: Forces acting on the aircraft body to be overcome by the thrust of the engines or propellers.

The corresponding expressions can be formulated as in (2.1-2.5) [10]. The angles γ and α represent the flight path angle and the angle of attack, respectively. Both the drag and the lift force depend on the square of the airspeed V as well as their respective coefficients, C_D and C_L.

$$\sum F_X = m \cdot \frac{dV}{dt} = T \cdot cos(\alpha_T) - F_D - m \cdot g \cdot sin(\gamma) \tag{2.1}$$

$$\sum F_Z = m \cdot V \cdot \frac{d\gamma}{dt} = T \cdot sin(\alpha_T) + F_L - m \cdot g \cdot cos(\gamma) \tag{2.2}$$

$$F_D = \frac{1}{2} \cdot \rho_{air} \cdot V^2 \cdot C_D \cdot A_{wing} \tag{2.3}$$

$$F_L = \frac{1}{2} \cdot \rho_{air} \cdot V^2 \cdot C_L \cdot A_{wing} \tag{2.4}$$

$$C_D = C_{D_0} + \frac{C_L^2}{\pi \cdot A \cdot e} \tag{2.5}$$

For conventional aircraft, the angle of attack in normally small [10]. By assuming a cambered airfoil design, lift is produced without a geometric attack angle. With $\frac{d\gamma}{dt} = 0$ and $\alpha = 0$, the aircraft weight is balanced by the lift force and the lift coefficient can be calculated as a function of the airspeed and the flight path angle. With these assumptions, the thrust equations simplify to

$$T = m \cdot \frac{dV}{dt} + \frac{1}{2} \cdot \rho_{air} \cdot V^2 \cdot C_D \cdot A_{wing} + m \cdot g \cdot sin(\gamma) \tag{2.6}$$

with $C_D = C_{D_0} + \frac{C_L^2}{\pi \cdot A \cdot e}$ and $C_L = \frac{2 \cdot m \cdot g \cdot cos(\gamma)}{\rho_{air} \cdot V^2 \cdot A_{wing}}$.
Both the aspect ratio A and the Oswald factor e are given by the aircraft design [10]. The zero-lift drag, C_{D_0}, represents the constant part of the drag coefficient and will also depend on the aircraft design. The zero-lift drag will change during the flight, inter alia when the landing gear is extended. The air density can be estimated as a function of the altitude, as in (2.7).

$$\rho_{air} = \frac{P_{h_0} \cdot M}{R \cdot T_{h_0}} \left(1 - \frac{L_T \cdot h}{T_{h_0}}\right)^{\frac{g \cdot M}{R \cdot L_T} - 1} \tag{2.7}$$

Here, P_{h_0} and T_{h_0} are the sea-level standard pressure and temperature, respectively. M is the molar mass of dry air, R is the ideal gas constant, L_T is the temperature lapse rate, h is the altitude and g is the gravitational acceleration.

2.1.2 Electric Propulsion

The thrust requirement can be translated to power by (2.8) [10].

$$P = T \cdot V \tag{2.8}$$

Due to the propeller efficiency, the actual power required at the shaft will be higher than what is given by the thrust and speed profiles. This speed dependent efficiency can be approximated by using the thrust coefficient, c_T, and the Froude propeller efficiency, η_F, presented in [11].

$$c_T = \frac{T}{0.5 \cdot \rho_{air} \cdot \vec{V}^2 \cdot A_{prop}} \tag{2.9}$$

$$\eta_F = \frac{2}{1 + \sqrt{1 + c_T}} \tag{2.10}$$

The propeller area A_{prop} can be obtained from the datasheet of the aircraft. By taking the motor efficiency η_{mot} into account, the power to deliver to the motors can be calculated as,

$$P_{rq} = \frac{T \cdot V}{\eta_F \cdot \eta_{mot}} \tag{2.11}$$

2.2 Hydrogen Storage

Despite having a very high gravimetric energy density, the volumetric density of hydrogen is far inferior to that of traditional jet fuel. For transport applications, hydrogen is typically highly compressed to limit the fuel tank size. Aviation brings even stronger space restrictions and may require liquefied storage at 20 K (-253°C). The gravimetric energy density of hydrogen is 33.3 kWh/kg, while the volumetric density will vary with temperature and pressure. Table 2.1 shows the properties of jet fuel and hydrogen under different conditions [12].

Table 2.1: Hydrogen and jet fuel specifications.

	Pressure [bar]	**Temp. [°C]**	**Density [kg/m^3]**	**Energy density [kWh/kg]**	**Energy density [kWh/L]**
H_2	Atm.	Amb.	0.089	33.3	0.003
H_2 (comp.)	350	Amb.	23	33.3	0.77
H_2 (comp.)	700	Amb.	42	33.3	1.40
H_2 (liq.)	Low	-253	71	33.3	2.36
Jet fuel	Atm.	Amb.	867	12.0	10.4

2.2.1 Compressed Hydrogen

Compressed storage is the most commercially mature method of storing hydrogen for transport applications. A challenge with compressed hydrogen storage is the weight of the required tank. Pressurized tanks are classified based on the materials and construction. Type I is an all-metal construction with a typical pressure of 300 bar and type IV is an all-composite construction

typically at 700 bar [13]. These types represent the two extremes, with type II and III being something in-between. Composite constructions are normally relatively expensive, but offer better gravimetric densities [13]. The type IV tank is illustrated in Fig. 2.2 and is used in the commercialized passenger vehicle, Toyota Mirai.

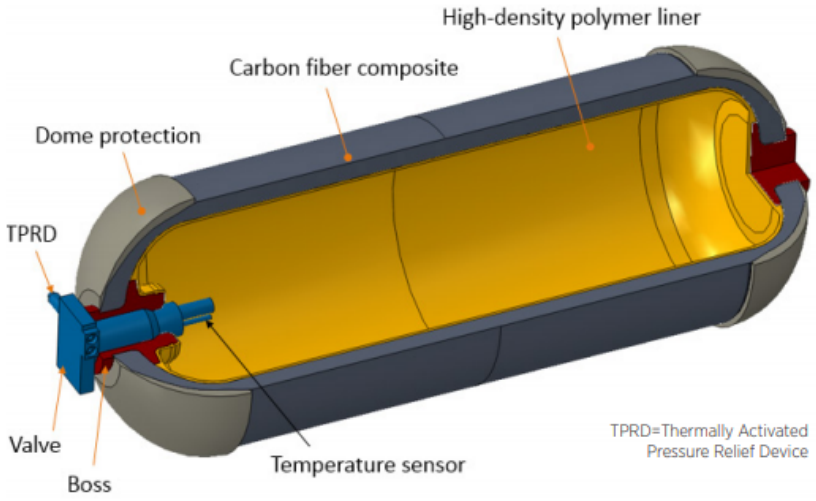

Figure 2.2: Type IV compressed hydrogen tank. Reprinted from [14].

The tanks of the Toyota Mirai have a gravimetric density of 5.7 wt%. This means that the storage capacity of 5 kg of hydrogen requires a tank weight of about 88 kg. Research is ongoing to increase this *weight efficiency*, but it still remains one of the main barriers for hydrogen in energy-intensive applications like aviation. DOE operates with an ultimate target of 6.5 wt%[1] for light-duty vehicles [15]. For larger vehicles, higher weight efficiencies can be expected. Already in 2018, Hexagon delivered tanks for fast ferry applications at above 8 wt% [16]. Both Zero-Avia and Universal Hydrogen are expected to base their initial hydrogen aircraft projects on compressed storage. An important reason for this is probably the technological level of readiness. Compressing the hydrogen also requires far less energy than liquefying it. Theoretically, isothermal compression from 1 to 800 bar requires 2.21 kWh/kg H_2 [17]. In [18], an actual compression work range of 2-4 kWh/kg is put forward for 350 bar tanks. This equals to between 6-12% of the H_2 LHV energy content.

2.2.2 Liquid Hydrogen

The corresponding liquefaction requires 3.23 kWh/kg H_2, theoretically [17]. However, the actual work of the liquefaction will be much higher. In 2019, SINTEF and NTNU presented a state-of-the-art liquefaction energy of about 10-12 kWh/kg and a long-term identified potential of almost halving this requirement [19]. The current estimate gives a liquefaction energy of about 30-36% of the H_2 LHV energy. To limit the pressure rise caused by heat transfer from the ambient,

[1] kg H_2/kg system including tank, valves, regulators and all other components.

cryogenic tanks must be appropriately insulated. If the boil-off rate exceeds the continuous energy requirement, some fuel must be released through a relief valve [13]. Alternatively, the hydrogen must be cooled actively, which will bring weight and parasitic losses. Still, liquefied storage may enable the use of cryogenic cooling circuits that can increase the efficiency of the propulsion system dramatically [20, 21]. As aircraft operate intensively with little downtime and require high energy density storage, aviation may be one of the most convenient applications for liquid hydrogen (LH_2) [13]. The weight efficiency of LH_2 tanks can be expected to be higher than compressed tanks due to the higher H_2 density and, thus, reduced tank surface area. Also, the tank walls do not have to withstand the same pressure levels, but the insulation will add some volume and weight.

2.2.3 Tank Design

The largest tank volume to tank area is achieved by a spherical geometry. For cryogenic storage, such a design will therefore minimize both the tank area and the required tank insulation. Compressed tanks are normally designed as high-pressure gas cylinders. Based on the energy requirement of the FC, the inner volume requirement of a tank can be calculated as,

$$V_{tank,i} = V_{H_2} = \frac{m_{H_2}}{\rho_{H_2}} = \frac{E_{rq}}{\omega_{H_2} \cdot \eta \cdot \rho_{H_2}} \tag{2.12}$$

where E_{rq} is the FC energy requirement, η is the FC efficiency, ω_{H_2} is the gravimetric energy density of hydrogen and ρ_{H_2} is the density of hydrogen. By using the geometrical properties of a sphere, the area A_{tank} and the tank mass can be calculated as

$$m_{tank,sph} = \varrho_{tank,sph} \cdot A_{tank} = \varrho_{tank,sph} \cdot 4\pi \left(\left(\frac{3 \cdot V_{tank}}{4\pi} \right)^{1/3} + r_w \right)^2 \tag{2.13}$$

where ϱ_{tank} is the area-specific tank mass and r_w is the thickness of the insulated tank walls. If the area-specific tank mass is estimated based on the inner tank volume, r_w can be assumed equal to zero for the calculation of the tank mass. Similarly, the area and mass of a cylindrical tank can be calculated by (2.14) under the assumption of an optimized height to radius ratio[2].

$$m_{tank,cyl} = \varrho_{tank,cyl} \cdot A_{tank} = \varrho_{tank,cyl} \cdot 6\pi \left(\frac{V_{tank}}{2\pi} \right)^{2/3} \tag{2.14}$$

Most larger transport aircraft store their fuel in integral tanks. This means that the fuel is stored in sealed areas inside the aircraft structure, such as the wings. For hydrogen aircraft, common ways of storing the fuel may need to be reconsidered to meet the requirements of compressed or cryogenic storage.

[2] The surface area of a cylinder is minimized when $r = h/2$.

2.3 Fuel Cell Theory

The characteristics of PEMFCs were reviewed in the project preceding this work [22]. In this section, the most relevant findings are supplemented with new material appropriate for the purpose of this thesis. Unless otherwise stated, the PEMFC will be the FC technology of interest for the rest of the report.

2.3.1 Principles and Structure

The FC converts chemical energy to electricity through electrochemical reactions. A FC stack consists of multiple cells to produce suitable voltage levels, as illustrated in Fig. 2.3. The key part of the each cell is often referred to as the membrane electrode assembly (MEA), where the anode and the cathode are separated by a polymer electrolyte membrane [23]. The electrodes are normally carbon-based, while Nafion is one of the most widely used membrane polymers [23]. The current per unit area of the cell surface, the current density, is often used to describe the rate of charge transfer. Large cell areas will, thus, allow a higher electrical current.

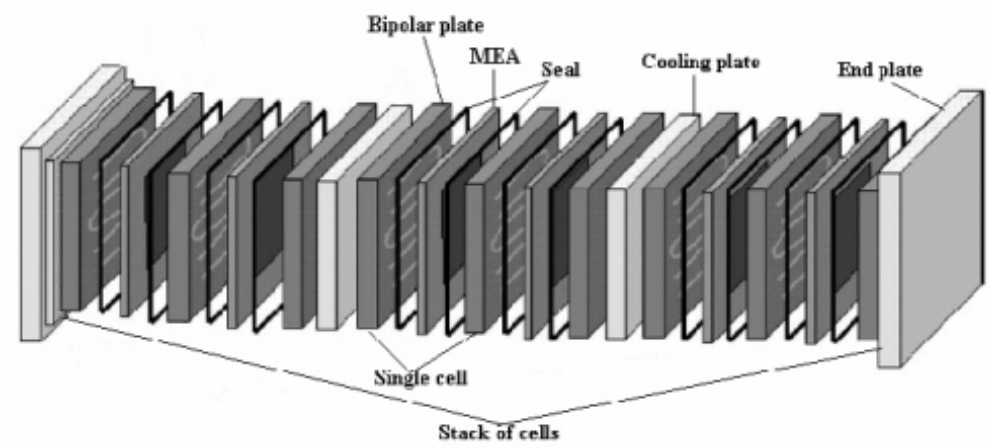

Figure 2.3: PEMFC stack. Reprinted from [23].

FCs use platinum (Pt) as catalyst for the splitting of the reactants. To reduce the required Pt loading, small particles can be placed on larger supporting particles based on carbon. In this way, the catalyst is well spread out and the active surface may be sufficient even with limited amounts of Pt [23]. As shown in Fig. 2.4, hydrogen molecules are split at the anode surface. The protons travel through the electrolyte to react with the oxidant at the cathode side, while the electrons pass through an external circuit. There are many similarities to conventional battery cells, but an important difference is that the reactants are supplied externally.

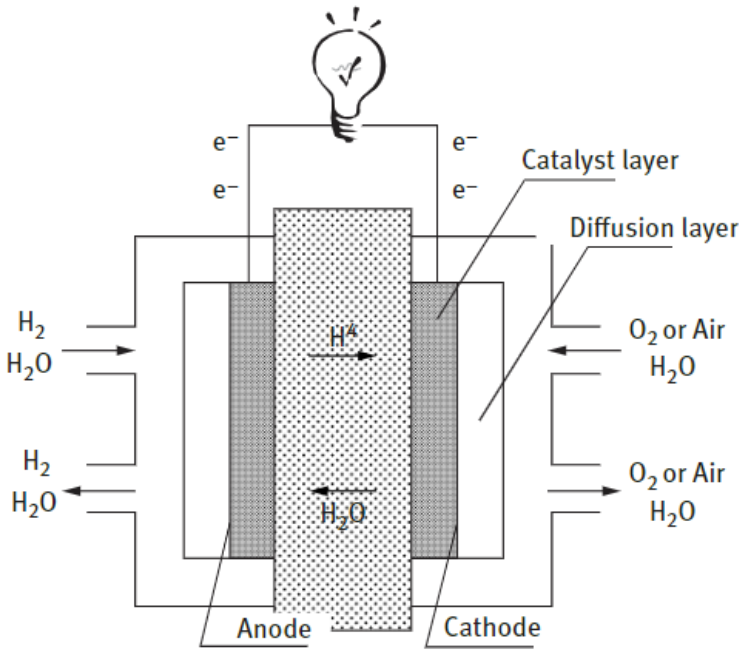

Figure 2.4: PEMFC principle. Reprinted from [24].

When hydrogen is used as the fuel and oxygen as the oxidant, the anode and cathode reactions are described by (2.15) and (2.16), respectively [23].

$$H_2 \rightarrow 2H^+ + 2e^- \tag{2.15}$$

$$0.5O_2 + 2H^+ + 2e^- \rightarrow H_2O \tag{2.16}$$

The reactants reach the electrodes of the cell through the gas channels in the bipolar plates [24]. The gas diffusion layer (GDL) connects the bipolar plate to the catalyst layer and ensures sufficient diffusion of the reactant gases [23]. The splitting of the reactants causes activation losses that reduces the performance of each cell [23]. In addition, there are losses related to the flow of protons through the membrane and the flow of electrons [23]. The magnitude of these losses will depend on the cell design, the materials used and operational parameters such as humidification level and temperature [23].

2.3.2 Voltage Characteristics

A FC is often characterized by its polarization curve and power curve, as depicted in Fig. 2.5.

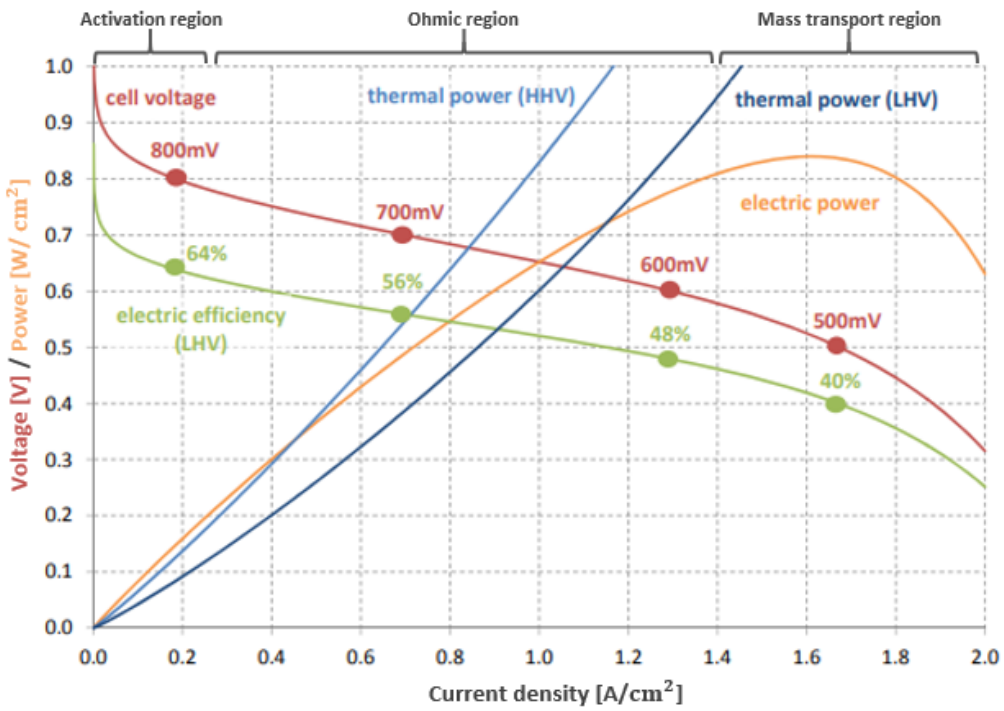

Figure 2.5: Typical voltage, power and efficiency curves for proton-exchange membrane fuel cells. Modified and reprinted from [25].

The polarization curve is divided into three distinct regions, given by the dominating voltage losses:

- **Activation region**: Voltage losses related to reduction of oxygen and oxidation of hydrogen at the cathode and anode, respectively.
- **Ohmic region**: Voltage losses related to the conduction of ions and electrons. The voltage and current have a close to linear relationship in this region.
- **Mass transport region**: Voltage losses related to decreased reactant concentrations at the electrodes. Occurs at high current densities.

The cell voltage can be expressed as [23],

$$E_{cell} = E_{OCV} - \Delta E_{act} - \Delta E_{ohmic} - \Delta E_{con} \tag{2.17}$$

where E_{OCV}, ΔE_{act}, ΔE_{ohmic} and E_{con} represent the open-circuit voltage (OCV), the activation, ohmic and concentration losses, respectively. The theoretical OCV can be expressed as [23],

$$E_{OCV,th} = 1.229 - 0.85 \cdot 10^{-3}(T - 298.15) + \frac{RT}{4F} ln\left(P_{O_2}(P_{H_2})^2\right) \tag{2.18}$$

where

T = cell temperature [K]
P_{H_2} = partial pressure of H_2 [atm.]
P_{O_2} = partial pressure of O_2 [atm.]
R = universal gas constant [J/(K·mol)]
F = Faraday's constant [C/mol]

Due to irreversible losses from hydrogen crossover, internal currents and parasitic oxidation reactions, the actual OCV voltage will be lower [23]. There are various ways to express the remaining voltage terms mathematically, depending on the desired level of detail and the objective of the analysis. In [7], an approximate analytical expression, based on physical parameters, is used to limit the computational cost and to allow estimations of the impact of development in FC materials. The polarization curve in Fig. 2.5 is based on an empirical equation with physical background [25]. The former approach requires data on physical properties like the cathode catalyst layer (CCL) and membrane thickness, while the latter obtains empirical coefficients without expressing such physical properties explicitly. As the activation losses are dominated by the oxygen reduction reaction (ORR) at the cathode, it can be estimated with at first order Tafel equation [23, 26],

$$\Delta E_{act} \approx \eta_{ORR} = \frac{RT}{\alpha F} ln\left(\frac{i + i_x}{i_{0,s} \cdot ECSA \cdot L_{Pt} \cdot 10}\right) \tag{2.19}$$

where
α = cathodic charge transfer coefficient
i = current density [A/cm^2]
i_x = current density of H_2 crossover [A/cm^2]
$i_{0,s}$ = specific exchange current density [A/cm^2]
$ECSA$ = electrochemically active surface area [m^2/g$_{Pt}$]
L_{Pt} = platinum loading [mg$_{Pt}$/cm^2]

The expression enables sensitivity on the the Pt loading, which represents a large share of the FC cost and is essential for the catalytic activity at the cathode. Another advantage is the explicitly expressed relation between the electrochemically active surface area (ECSA) and the ORR potential, which can be useful for ECSA loss related lifetime calculations. Similarly, the oxygen concentration losses can be estimated for the same purpose. For hydrogen/air FCs, the decreased concentration of oxygen at the catalyst surface will cause significant losses at high current densities. The corresponding losses can be expressed as [27],

$$\Delta E_{con} \approx \Delta U_{O2-tx} = \frac{RT}{F} \cdot \left(\frac{1}{4} + \frac{\gamma}{\alpha}\right) \cdot ln\left(\frac{p_{O2,ch} - \frac{RT}{4F} \cdot R_T \cdot i}{p_{O2,ch}}\right) \tag{2.20}$$

where γ is the kinetic order of the ORR and $p_{O2,ch}$ is the oxygen partial pressure in the channel. R_T, the oxygen transport resistance, represents the depletion of O_2 pressure between the channel and the catalyst [27]. In [26], a linear relationship was suggested between the oxygen transport resistance and the inverse ECSA. The resistance can be divided into a pressure-independent term R_{NP} and a pressure-dependent term R_P [28],

$$R_T = R_P + R_{NP} = R_P + R_{Knudsen} + \frac{R_{Pt}}{f} \tag{2.21}$$

where $R_{Knudsen}$ represents the Knudsen diffusion resistance and R_{Pt} represents the resistance at the platinum surface with $f = L_{Pt} \cdot ECSA \cdot 10$. The voltage loss in (2.20), which actually is a correction term for the OCV and the ORR voltage, is derived in [27]. The term will typically have little influence in the operation range presented in commercial datasheets, such as that of the PowerCellution P-stack [29], but will catch the effect of ECSA loss at high current densities. The impact of operating pressure and temperature can be implicitly adjusted for through α and $i_{0,s}$, as in (2.22) and (2.23), respectively [30, 31].

$$\alpha = 0.495 + 2.3 \cdot 10^{-3}(T - 300) \tag{2.22}$$

$$i_{0,s} = i^*_{0,s}\left(\frac{P_{O_2}}{P^*_{O_2}}\right)^{\gamma} exp\left(\frac{-E_c^{rev}}{RT}\left(1 - \frac{T}{T^*}\right)\right) \tag{2.23}$$

Here, $i^*_{0,s}$ is the specific exchange current density normalized to the reference temperature T^* and oxygen partial pressure $P^*_{O_2}$. E_c^{rev} represents the activation energy of the ORR at the reversible cell potential [31]. The ohmic losses in the stack is normally modelled as a simple resistive term, which is dominated by the ionic resistance in the electrolyte [23],

$$\Delta E_{ohmic} = R_{ohm} \cdot i. \tag{2.24}$$

2.3.3 Operating Pressure

For hydrogen/air FCs, both ambient and pressurized operation are common. The performance of the stack can be improved at elevated pressures, expressed through the OCV (2.18) and the exchange current density (2.23). This gain will at some point be equalized by the parasitic power losses of the compressor. In addition, pressurized operation may also complicate the water management [32]. As the fuel is normally supplied as pure hydrogen from compressed tanks, it do not require any compression work before entering the stack. If the fuel is supplied in a closed loop system, a recirculating pump can be used to account for the pressure drop between the inlet and the outlet of the stack. For the cathode side, a blower or a compressor must be utilized to feed the required air flow at the desired inlet pressure [32]. The FC can be operated at ambient conditions at the outlet or at pressurized levels, typically up to a few bars [32]. For ele-

vated applications, such as aviation, the ambient pressure will vary significantly. In such cases, pressurized operation can prevent a degraded stack performance at typical cruise altitudes. For systems where air is used as the oxidant, a high stoichiometry[3] is required due to the low concentration of oxygen in air. This is to ensure a high oxygen concentration and to help remove exhaust water from the cells [32]. It will also improve the dynamic capabilities of the system. While pure hydrogen is typically supplied with an excess ratio between 1 and 1.2, the air excess ratio can be as high as 2-2.5 [32]. Also here, there will be a trade-off between the performance gain of an increased air flow rate and power consumption of the compressor. A higher excess ratio may often be used at low loads than at high loads [25].

2.3.4 Operating Temperature

Low temperature PEMFCs are normally operated below 90°C [23]. In most cases, an increased operating temperature will increase the stack performance [23]. The ionic conductivity is improved and the exchange current density is higher, but an increased temperature also results in a lower theoretical potential and a higher Tafel slope [33]. As the stack temperature will also affect the efficiency of the cooling system, the operating temperature should be chosen based on the full system design. Another consideration is how the temperature-driven degradation affects the lifetime of the FC. Elevated temperatures are known to accelerate degradation mechanisms such as platinum dissolution and carbon corrosion [34].

2.3.5 Efficiency

The efficiency of each cell can be expressed as,

$$\eta_{el,LHV} = \frac{V_{cell}}{1.253V} \tag{2.25}$$

where $1.253V$ is the hydrogen lower heating value (LHV) voltage equivalent [25]. It is apparent that the cell efficiency will suffer at increased current densities, as illustrated in Fig. 2.5. The electric efficiency of the whole FC stack is found by calculating the average voltage of the N cells put in series. The FC stack is only the main component of a larger system. Balance-of-plant (BoP) components such as the air compressor, the humidifier, the fuel supply and the thermal system will also consume energy. This means the overall FCS efficiency will be different from that of the stack. By also considering the utilization factor of the hydrogen fuel, the FCS efficiency can be expressed as,

$$\eta_{fcs,el} = \frac{P_{net,output}}{P_{fuel,input}}, \; P_{net} = P_{gross} - P_{bop} \tag{2.26}$$

[3] Air excess ratio.

where P_{bop} represents the power consumption of the BoP components [25]. Figure 2.6 illustrates the difference between the stack efficiency and the overall FCS efficiency for a typical FCS.

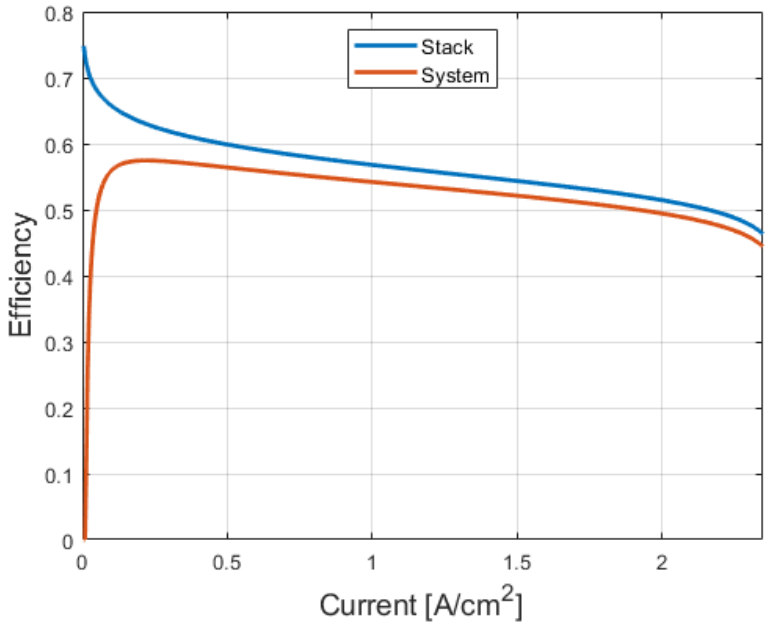

Figure 2.6: Typical fuel cell stack and system efficiencies. System efficiency includes the parasitic losses of the balance-of-plant components.

Due to the power consumption of the BoP components, the overall efficiency will be low if the FC is operated at very low power levels.

2.3.6 Heat and Water Management

The mass flow rate of water generation from the FC can be calculated as [32],

$$\dot{m}_{H_2O} = \frac{N_{cells} \cdot I_{fc}}{2F} \cdot M_{H_2O} \tag{2.27}$$

where

N_{cells} = number of cells
I_{fc} = FC current [A]
F = Faraday's constant [C/mol]
M_{H_2O} = molar mass of water [kg/mol]

The water byproduct may be reused for both humidification and cooling purposes [35]. Another possibility is to use part of the waste water as service water, which may reduce the aircraft

takeoff weight [1]. For low power applications, natural convection or air cooling may be sufficient. The FC air flow can also be used to remove some heat from the stack. The hydrogen and air flow into the FC can be calculated as in (2.28) and (2.29), respectively [32, 35].

$$\dot{m}_{H_2} = \frac{N_{cells} \cdot I_{fc}}{2F} \cdot \lambda_{H_2} \cdot M_{H_2} \tag{2.28}$$

$$\dot{m}_{air} = \frac{N_{cells} \cdot I_{fc}}{4F} \cdot \frac{\lambda_{O_2} \cdot M_{air}}{0.21} \tag{2.29}$$

Here,

λ_{H_2} = H_2 stoichiometry
M_{H_2} = molar mass of H_2 [kg/mol]
λ_{O_2} = oxygen stoichiometry
M_{air} = molar mass of air [kg/mol]

For high power FC stacks, particularly for transport applications, liquid cooling is most often used for heat removal [36]. Liquid cooling gives a high cooling capability with flexible control, but also brings weight, volume and parasitic power losses [36]. The heat generation from the FC stack can be calculated as [36],

$$Q_{therm,HHV} = (V_{HHV} - V_{cell}) \cdot I_{fc} \cdot N_{cells} \tag{2.30a}$$

$$Q_{therm,LHV} = (V_{LHV} - V_{cell}) \cdot I_{fc} \cdot N_{cells} \tag{2.30b}$$

where V_{HHV} = 1.481V and V_{LHV} = 1.253V are the voltage equivalents of the hydrogen higher heating value (HHV) and the LHV, respectively. The LHV is used if all water is assumed to be vapor at the FC outlet. The heat to be removed by the coolant can be calculated as [25],

$$Q_{cool} = Q_{therm,HHV} - Q_{dis} - Q_{exhaust} \tag{2.31}$$

where Q_{dis} is the heat dissipated through the stack surface and $Q_{exhaust}$ is the differences between outlet and inlet gas enthalpy. Further, the coolant flow rate can be calculated as [35],

$$\dot{m}_{coolant} = \frac{Q_{cool}}{c_{p,c} \cdot \Delta T} \tag{2.32}$$

where $\Delta T = T_{cool,out} - T_{cool,in}$. A large ΔT reduces the required flow rate of the coolant, but results in a less uniform temperature in the FC stack [35]. The coolant temperature increase is typically $\leq$ 10K [25, 35]. As the size of the heat exchanger (HEX) depends on the temperature difference between the ambient air and the coolant, a higher FC operating temperature can limit the component size [35]. The pumping power related to the coolant system should be considered, as it will limit the net power supply from the FC. One way to express this power is

[37],

$$P_{pump} = \frac{\Delta p_{fric} \cdot \dot{m}_{coolant}}{\eta_{pump} \cdot \rho_{coolant}} \tag{2.33}$$

where

Δp_{fric} = frictional pressure loss [Pa]
η_{pump} = pump efficiency
$\rho_{coolant}$ = the density of the coolant [kg/m^3]

Due to the low operating temperature of the FC, either cooling fans or large radiator surface areas are required to transfer all heat to the ambient [38]. Note that for aviation some of the waste heat from the FC can also be utilized in the environmental control system and the wing ice protection system [1]. A heat accumulation in the FC stack can be expressed as,

$$\Delta T_{cell} = \int_{t_1}^{t_2} \frac{Q_{net}}{m_{fc} \cdot c_{p,fc}} dt \tag{2.34}$$

where Q_{net} is the net heat generation, m_{fc} is the FC mass and $c_{p,fc}$ is the specific heat capacity of the FC stack. When the stack temperature increases, the heat transfer capability will increase due to higher temperature differences between the stack, coolant and the ambient.

Heat Exchanger

The heat rejected from the FC to the coolant must be rejected to the ambient air by the use of HEXs. Compact heat exchangers (CHEs), characterized by a small size and a high performance, are often used for aircraft applications [39]. As for the FC cooling channels, the HEX will bring a significant pressure drop related to the heat transfer between the coolant and the ambient air. The HEXs can be cooled by inlet ducts utilizing the airspeed. In this way, large cooling fans can be avoided, but the air ducts will bring a parasitic drag to the aircraft [40]. Figure 2.7 illustrates the conceptual double-loop cooling system where the FCS heat is rejected to the ducted ambient air through a HEX.

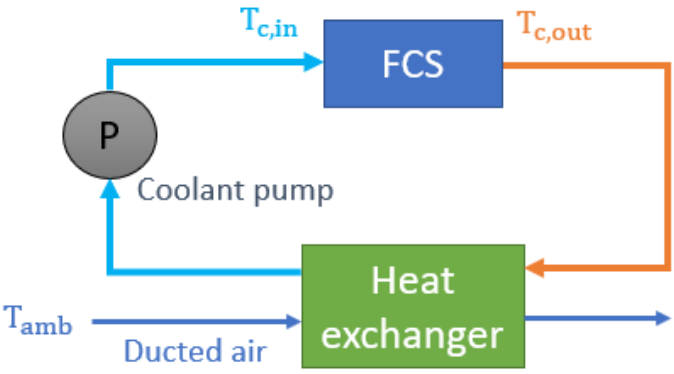

Figure 2.7: Cooling system illustration.

The required HEX suraface area can be estimated by the heat rejection requirement, the heat transfer coefficient and the temperature difference between the coolant and the ambient air, as expressed in (2.35) [41].

$$A_{rad} = \frac{Q_{rad}}{U_{rad} \cdot \Delta T_{HEX}} \tag{2.35}$$

To achieve compact radiators it will therefore be beneficial to use materials and designs that contribute to high heat transfer coefficients and to allow high coolant temperatures to increase the heat flux.

2.3.7 Air Compression System

A FC can be operated at different pressure levels. By increasing the operating pressure, a potential gain can be achieved, as depicted in Fig. 2.8.

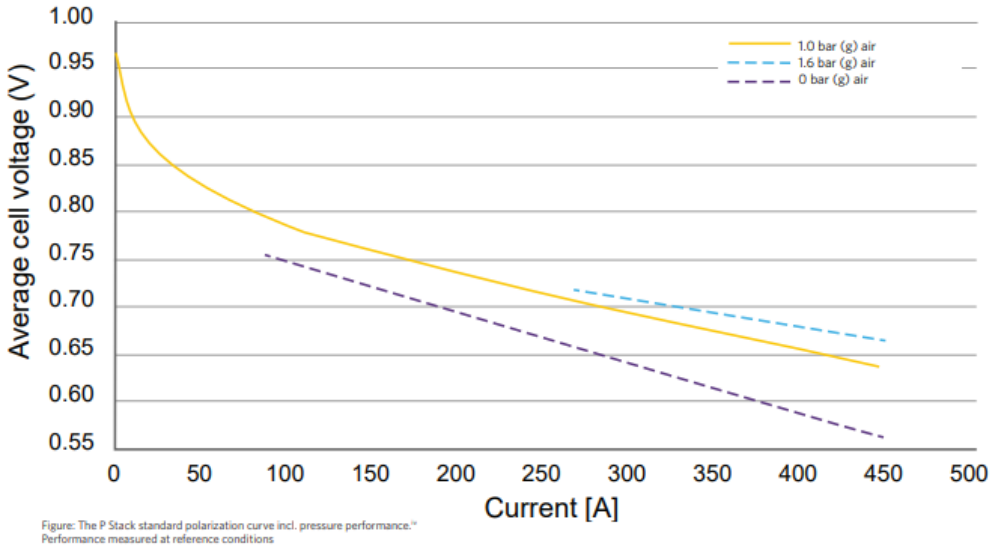

Figure 2.8: Polarization curve for the PowerCellution P stack from PowerCell Sweden [29].

For H_2/O_2 FCs, both reactants are normally stored at elevated pressure levels. In this case, the FC can be operated above ambient pressure without the need for compression. In most applications, it will be more practical to use oxygen from air than to store pure oxygen in tanks [35]. For H_2/air FCs, the oxidant will be at ambient pressure. Thus, there will be a trade-off between the potential gain of compression and the parasitic power losses related to the air compressor. The Toyota Mirai utilizes pressurized systems to increase its power response and efficiency. Such systems are typically operated in a range between ambient pressure and 3 bars [32]. The required compression work may be significantly larger at cruise altitudes than at ground-level. Due to the degraded FC performance at lower operating pressures, air compressors are important components for high altitude applications, in particular. The environmental conditions at altitudes up to 11,000 meters can be estimated by (2.36) and (2.37), where T_{amb} and P_{amb} represents the ambient temperature and pressure, respectively [42].

$$T_{amb} = T_{h_0} + L_T \cdot h \tag{2.36}$$

$$P_{amb} = P_{h_0}\left(\frac{T_{amb}(h)}{T_{h_0}}\right)^{-\frac{g}{L_T \cdot R_{spec}}} \approx P_{h_0}\left(\frac{T_{amb}}{T_{h_0}}\right)^{-5.256} \tag{2.37}$$

Here, R_{spec} is the specific gas constant of dry air. The power consumption associated with adiabatic air compression between two pressure levels, and the corresponding outlet temperature, can be expressed as in (2.38) and (2.39), respectively [35].

$$P_{comp} = \frac{\dot{m}_{air} \cdot c_p \cdot T_1}{\eta_{comp}}\left(\left(\frac{P_2}{P_1}\right)^{\frac{k-1}{k}} - 1\right) \tag{2.38}$$

$$T_2 = T_1 + \frac{T_1}{\eta_{comp}}\left(\left(\frac{P_2}{P_1}\right)^{\frac{k-1}{k}} - 1\right) \tag{2.39}$$

where

$\dot{m}_{air}$	=	air flow rate [kg/s]
c_p	=	specific heat capacity, air [J/(kg·K)
T_1	=	air temperature before compression [K]
T_2	=	air temperature after compression [K]
η_{comp}	=	compressor efficiency
P_1	=	air pressure before compression [Pa]
P_2	=	air pressure after compression [Pa]
$k =$	=	specific heats ratio (k=1.4 for diatomic gases [35])

Positive displacement compressors or centrifugal compressors are typically applicable for pressurized systems [35]. These types of compressors have different pressure-flow characteristics.

The characteristics are not considered in detail in this work. For pressurized systems, where the outlet air pressure is higher than the ambient pressure, a turbine or an expander can be utilized to extract energy from the exhaust [35]. The FC outlet pressure P_{out} will be slightly lower than the inlet pressure due to the pressure drop inside the stack. The power extracted from the exhaust air can be calculated as [35],

$$P_{exp} = \dot{m}_{air} \cdot c_p \cdot T_{out} \left(1 - \left(\frac{P_0}{P_{out}}\right)^{\frac{k-1}{k}}\right) \eta_{exp} \tag{2.40}$$

where T_{out} is the exhaust air temperature, P_0 is the ambient pressure and η_{exp} is the expander efficiency. A FCS where the compressor and the expander are mounted to the same shaft is illustrated in Fig. 2.9. Due to inefficiencies, only parts of the compression work can be harvested by the expander [35].

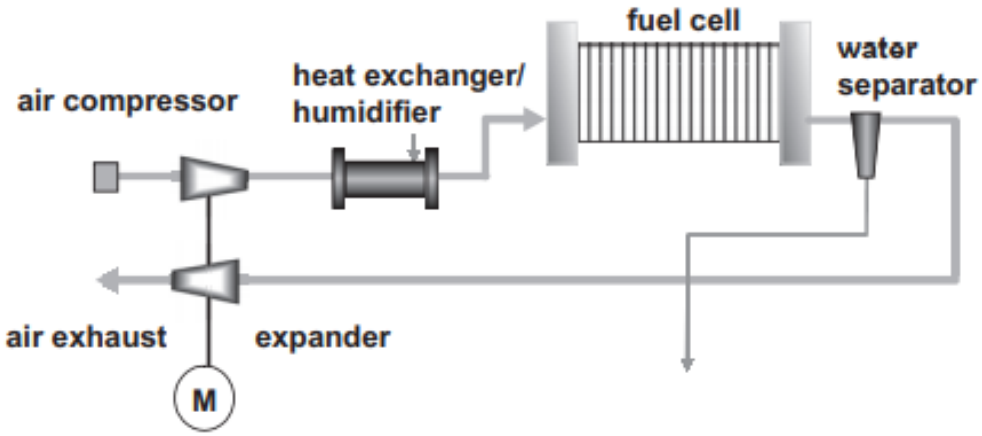

Figure 2.9: Fuel cell system with a combined compressor and expander for the air supply subsystem. Reprinted from [35].

The air supply subsystem also plays an important role for the operational limits of the FC.

2.3.8 Degradation and Operational Limits

The FC humidification and the gas supply are mechanisms that are sensitive to the FC power slope. If the requested power from the load changes too fast, the air supply to the cathode may be insufficient and cause oxygen depletion [43]. Such conditions should be avoided even for brief periods [44]. This means that the response time of the FCS will be highly dependent on the air supply from the compressor of the system. DOE reports transient time responses of 1s for 10%-90% air flows from transportation compressors [45]. The mechanical dynamics of state-of-the-art compressors in FC road vehicles are also suggested to be of this magnitude [46]. A possible way to avoid depletion is to adjust the flow rate of the fuels to a fixed level that ensures

fuel excess at all points of operation [43]. However, this will result in a high parasitic BoP power and, thus, a poor utilization of the fuels [43]. To ensure reliability, efficiency and high lifetime for FCs in a dynamic environment, the current slope has to be controlled and limited [43]. The supply of hydrogen and oxygen will usually be regulated by a current control loop, where the required fuel supply is calculated from the same current reference as the one going to the power converter [43]. PowerCell Sweden reports a 13 kW/s ramp-up speed limit on their 100-kW FCS [47].

FCs are typically suggested to operate with cell voltages of about 0.6 V to 0.9 V. Low cell voltages facilitate production of hydrogen peroxide, which has a degrading effect on the membrane [48]. This means that the FC power range should have both an upper and a lower bound. In [49], the FCS is designed to operated between 20 and 60 kW. If the load power decreases beyond the lower bound, the FCS can be put into idling mode to prevent undesirable cell voltages [50]. High cell potentials and temperatures are shown to accelerate the loss of ECSA due to carbon corrosion, Ostwald ripening and Pt dissolution [28]. Loss of ECSA is one of the main FC degradation mechanisms. It is an important metric in the technical stack targets set by DOE due to its close relation to the power and efficiency losses [51]. The loss of ECSA reduces the cell performance, primarily due to increased activation losses [28]. At high current densities, also the increase in oxygen transport resistance due to ECSA loss is reported to affect voltage losses significantly [26]. The FC end-of-life (EoL) criteria is normally defined at a 10% power loss for the FCS [23].

Further elaboration on FC degradation can be found in Appendix B.1. A schematic overview of catalyst and membrane degradation mechanisms are given in Fig. 2.10.

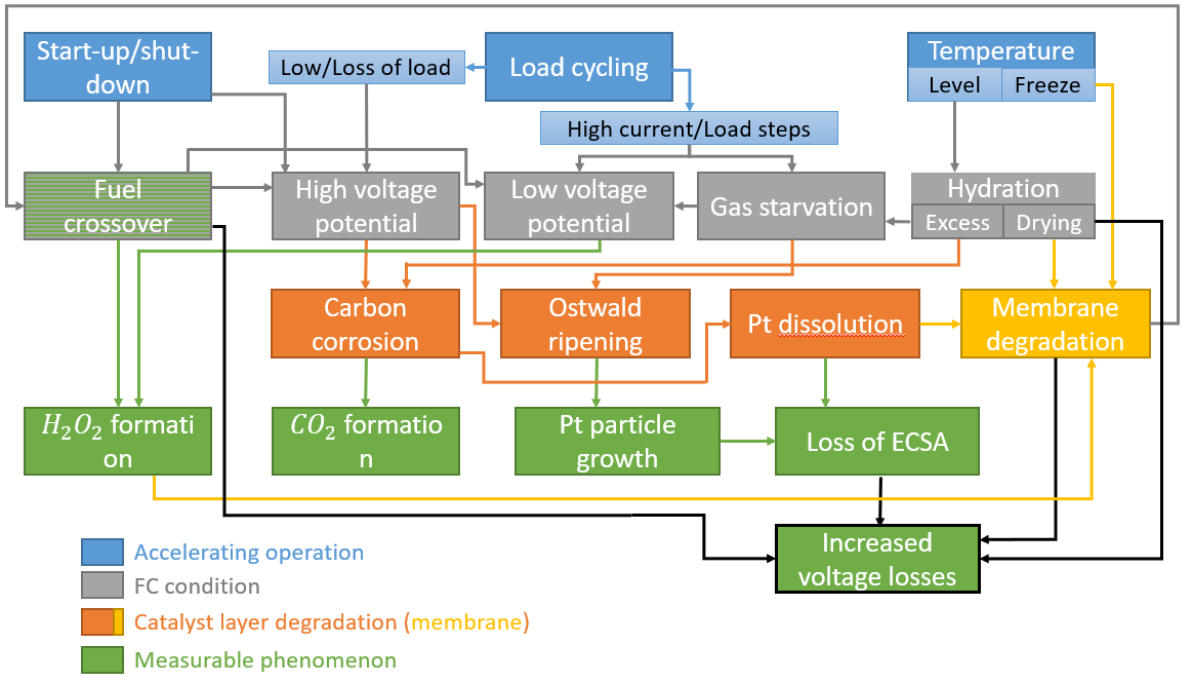

Figure 2.10: Overview of the degradation of the catalyst layer and the membrane of a fuel cell (FC) stack. Notice the interconnection between different degradation modes and FC conditions, that further accelerates and amplifies their effects on the FC. Reprinted from [22].

2.3.9 Transient Characteristics

The impedance of the FC is frequency-dependent. This means that the steady-state polarization curve will not be representative for the FC operation during transients. Figure 2.11 depicts a typical equivalent electrical circuit (EEC) for a FC.

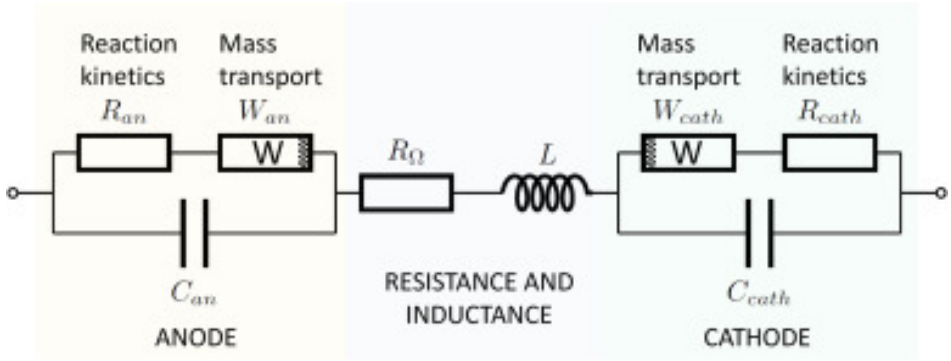

Figure 2.11: Equivalent electrical circuit including electrode impedances, ohmic resistance and cable inductance. Reprinted from [52].

At the electrodes, the activation potential and the mass transport losses are represented by resistors and Warburg elements, respectively. These processes possess varying time constants. The

two capacitors at the electrodes model the double-layer phenomena between the electrodes and the electrolyte. Unlike the instantaneous ohmic response, the activation and mass transport will, thus, depend on the time constants given by the equivalent capacitors and the respective equivalent resistances [53]. Due to these time constants, the cell resistance is approximated to R_Ω at very high frequencies. This equivalent resistance is dominated by the protonic resistance in the FC membrane [23]. Also the equivalent inductor, primarily given by the surrounding circuitry, may affect the impedance at such frequencies. Knowledge about the inductive part of the impedance can be valuable for the design of the converter inductor. Typical FC impedance characteristics are illustrated in Fig. 2.12, where the frequency of the electrochemical impedance spectroscopy (EIS) is increasing from right to left.

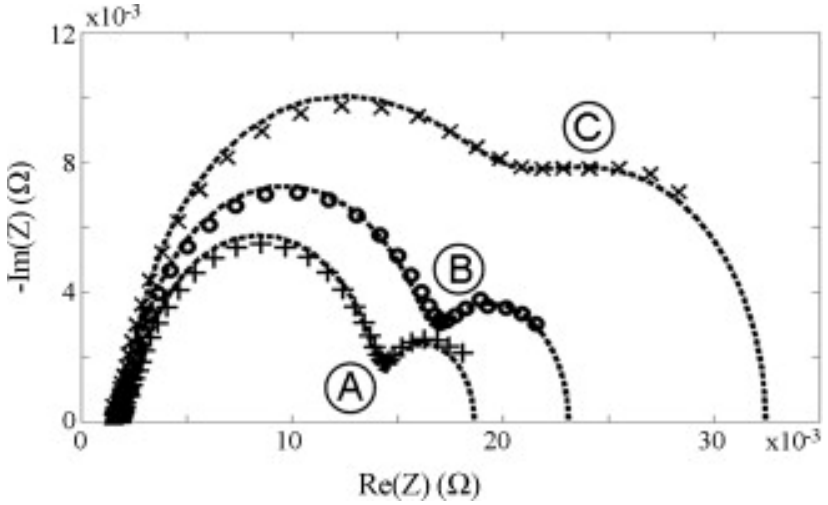

Figure 2.12: Proton exchange membrane fuel cell impedance spectrum at different air flow rates: (A) 0.61 ml/min, (B) 0.51 ml/min and (C) 0.32 ml/min. Reprinted from [54].

At the highest frequencies, the impedance moves towards the ohmic resistance. For decreasing frequencies, the impedance moves towards the steady-state resistance. For the frequencies in-between, capacitive contributions can be seen due to the double-layer capacitance, forming semi-circles characterized by the corresponding time constants. These impedance spectra also illustrate how the resistance increases as the air flow rate decreases.

To limit the number of cells, and account for the current dependency of the FC voltage, DC-DC converters are normally used to step the voltage up or down. The switching frequency of such converters will normally range from a few kHz to hundreds of kHz. Already at a few kHz, the effect of the double-layer capacitance minimizes the electrochemical resistance and limits the voltage loss to that of the ohmic region. In [55], the *working voltage* of the FC is expressed as,

$$V_w = E - \eta - Ri \tag{2.41}$$

where the overvoltage caused by electrochemical reactions $\eta \approx \eta(I_{avg})$. This assumption implies that the high frequency ripple caused by the DC-DC converter will mainly affect the ohmic

voltage losses. For the concentration losses, this assumption is reasonable as mass transport is too slow to be activated at such frequencies [56]. The activation overpotential relates to faster electrochemical processes and may be significant at low switching frequencies [56, 57]. As the protonic resistance dominates the ohmic region, heating and mechanical deterioration of the membrane may be consequences of operating with a high ripple content at high switching frequencies. This concern is also addressed in the literature. A literature review was performed in the work preceeding this thesis regarding the impact of both high and low frequency current ripple [22]. The key findings are summarized below.

Current Ripple from Switching Devices

In [57, 58, 59], current ripple of higher frequencies ($\geq$ 1 kHz) are studied. Conversely, lower frequency current ripple ($<$ 1 kHz) are studied in [57, 60, 61]. In general, the current ripple typically imposed by grid-connected inverters (~100 Hz) appears to be of more concern than the switching ripple from DC-DC converters [53]. The double-layer phenomena of the FC is shown to filter the high frequencies [57, 59]. These frequencies are not filtered by the membrane and a slight influence on FC lifetime is shown even for frequencies in the kHz range [58, 59]. For lower frequencies, the impact on lifetime and performance are found to be more profound. Experimental tests show accelerated degradation of the cathode catalyst and a complicated diffusion of the oxidant at the cathode surface [60, 61]. The same frequencies have also been shown to give a dramatic decrease in the utilization of the fuel gases, which leads to low operating efficiencies [61]. Fontes et al. [57] concludes that the electrochemical processes can be decoupled from the high frequency current ripple, while electrochemical interaction must be expected for low frequency oscillations. The tolerance of the double-layer capacitor and the degrading effect on the membrane should still be kept in mind [57, 59].

Despite extensive research, no good quantification of the high frequency current ripple limit has been obtained in this work. According to Gemmen, the impact from frequencies above 1250 Hz are insignificant except at very high ripple factors. Wahdame et al. [58] experienced no significant FC degradation with 1 kHz $\pm$10% current oscillations. Contrarily, in [62], a ripple limitation of 2% was determined in collaboration with IFE[4] for a marine PEMFC application. However, this was only meant as a general guideline to guarantee a low impact on the FC health [62]. Low weight and volume of the filtering inductor is particularly important in aviation. As the high frequency current ripple is believed to have a very small impact on the FC lifetime, a less conservative ripple constraint can be expected to give a better overall cost benefit for such applications. To make good choices when designing the DC-DC converter, more specific testing on the possible degradation of the FC membrane should be performed.

At lower frequencies, both FC lifetime and performance are significantly affected. This means that current ripple below the kHz-range, and fast load changes, should not propagate to the FC.

[4] IFE = Institutt for energiteknikk (Institute for Energy Technology).

Normally, bulky capacitors are used as passive filters at the DC-link to mitigate the low frequency current ripple. Faster-responding power devices such as supercapacitors and, possibly, batteries can also be utilized for the same purpose [63]. Thus, such devices may compensate for the slow dynamics of the FCS and allow a more efficient and favourable operation.

2.3.10 Hybridization

There exists various energy storage (ES) devices offering characteristics that can complement FCs in an energy system. Batteries and supercapacitors (SCs) are two promising technologies in this context. Unlike FCs, batteries and SCs do not rely on external reactant supply. Batteries store energy chemically in the electrodes. The time constants in the electrochemical processes limits their response time compared to SCs, but is superior to that of FCs. Like conventional capacitors, SCs store energy in an electric field between its two electrodes. This results in an almost instantaneous power response. The absence of cyclical chemical reactions also gives SCs a durability superior to that of batteries and FCs. To prevent reactant starvation in the FC during power transients, Fig. 2.13 depicts a possible energy management strategy where the FC only covers the lowest frequencies.

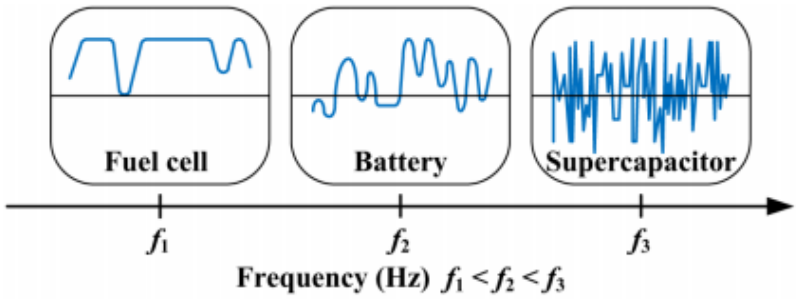

Figure 2.13: Energy management strategy for a fuel cell, battery and supercapacitor hybrid system. Reprinted from [64].

There are various levels of hybridization that can be adopted in a vehicle. A *light hybridization* represents one end of the scale. In this context, this implies only sizing the ES device to account for the FCS response time, cold start assistance and energy recovery [46]. Such an ES device must have a high power capability rather than energy capacity. Light hybridization is used in the Toyota Mirai where the FCS is the primary power source. Conversely, the FCS can be used solely as a *range extender* for battery-electric, or other, vehicles. In this case, the FCS is not the primary power device, but provides energy support to the hybrid system [46]. For aircraft applications, the power requirement during the takeoff and the initial climb can be more than twice the average power [10]. If the FCS is only sized at a power level between average power and peak power, the ES devices must also be sized to match a significant energy requirement [35]. The HY4 aircraft combines a FC with a 45 kW battery to supply a 80 kW engine [21]. With

an energy capacity of 21 kWh, the battery is capable of providing peak power during takeoff and climb. Typical power and energy density ranges of FCSs, batteries, supercapacitors and capacitors are illustrated in Fig. 2.14.

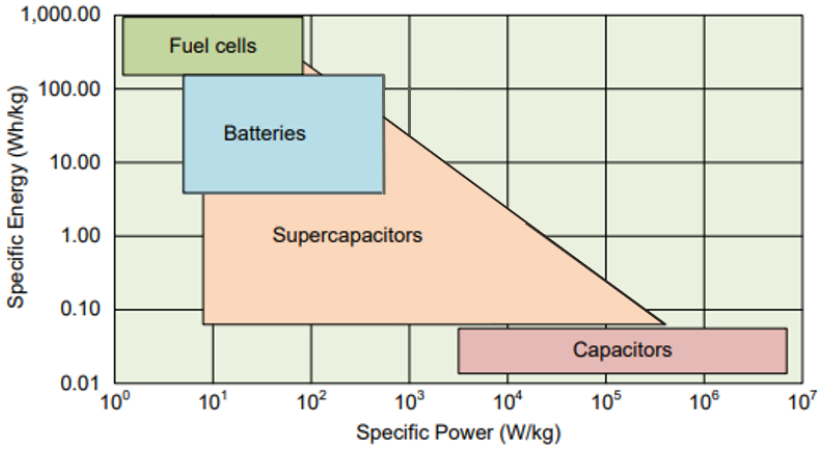

Figure 2.14: Energy storage specifications. Modified and reprinted from [65].

Due to large technology developments the latest years, the illustration is not accurate for state-of-the-art devices, but shows the classical trends. The FC stack used in the Toyota Mirai delivers about 2 kW/kg, while PowerCell Sweden offer industry leading power densities of almost 3 kW/kg [29]. As illustrated in Fig. 2.15, these densities are not representative for the whole FCS.

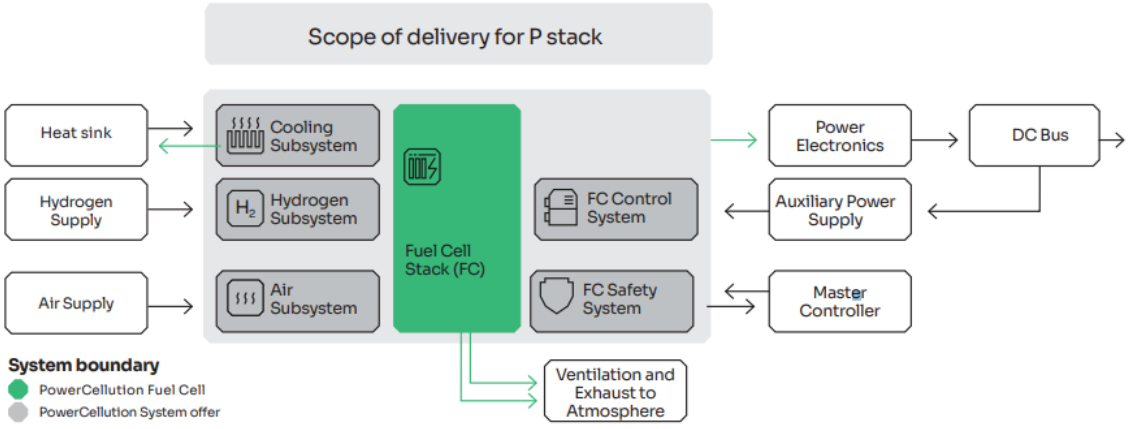

Figure 2.15: Fuel cell system boundaries. Reprinted from [29].

In [7], also the peripheral equipment of the FCS is included in the reported power density of 1.6 kW/kg. This is similar to the power density targets of 1.50 kW/kg for commuter aircraft and 1.75 kW/kg for regional aircraft forwarded in a recent EU case study[5] [3]. The same study also reports the state-of-the-art power density to be 750 W/kg on system level. The energy content

[5]Prepared by McKinsey & Company for the Clean Sky 2 JU and Fuel Cells and Hydrogen 2 JU.

will be decided by the stored hydrogen fuel. Due to the corresponding storage requirements, the effective energy density will be heavily dependent on the weight of the fuel tank.

Different types of batteries offer different characteristics, with a trade-off between energy and power density [65]. The application of providing power support during demanding flight phases may benefit from a high power density to energy density ratio. The Li-ion batteries used in the 2015 Airbus E-fan AEA have an energy density of 207 Wh/kg [65]. The energy density of the HY4 aircraft battery is 161.5 Wh/kg. The corresponding specifications for the FC and the compressed hydrogen storage are 450 W/kg and 2.01 kWh/kg, respectively [21].

2.4 Battery Theory

This means that the response time will not be delayed by the slowness in peripheral components. Battery modules usually consists of numbers of cells stacked in series and parallel to achieve appropriate voltage and capacity levels, respectively. Multiple modules may further be connected and encased in housings together with sensors, battery management systems (BMSs) and thermal management systems (TMSs) to form complete battery systems. For transport applications, the combined modules and circuitry is often referred to as a *battery pack*. The majority of battery packs used in electric vehicles (EVs) today are based on lithium-ion cells. This technology has experienced rapid improvements in both performance and costs the last decade. Different Li-ion chemistries possess different attributes. In 2018, Hentunen et al. published a report investigating both the technical and economic characteristics of common chemistries [66]. These characteristics are summarized in Fig. 2.16.

	Lithium Iron Phosphate	Lithium Manganese Oxide	Lithium Titanate	Lithium Cobalt Oxide	Lithium Nickel Cobalt Aluminum	Lithium Nickel Manganese Cobalt
Cathode chemistry descriptor	LFP	LMO	LTO	LCO	NCA	NMC
Specific energy (Wh/kg)	80–130	105–120	70	120–150	80–220	140–180
Energy density (Wh/L)	220–250	250–265	130	250–450	210–600	325
Specific power (W/kg)	1400–2400	1000	750	600	1500–1900	500–3000
Power density (W/L)	4500	2000	1400	1200–3000	4000–5000	6500
Volts (per cell) (V)	3.2–3.3	3.8	2.2–2.3	3.6–3.8	3.6	3.6–3.7
Cycle life	1000–2000	>500	>4000	>700	>1000	1000–4000
Self-discharge (% per month)	<1%	5%	2–10%	1–5%	2–10%	1%
Cost (per kWh)	$400–$1200	$400–$900	$600–$2000	$250–$450	$600–$1000	$500–$900
Operating temperature range (°C)	−20 to +60	−20 to +60	−40 to +55	−20 to +60	−20 to +60	−20 to +55

Figure 2.16: Lithium-ion battery chemistry specifications. Reprinted from [66]

Lithium Nickel Cobalt Aluminium (NCA) represents a chemistry with both a competitive specific energy and specific power. This chemistry is currently used in such as Tesla's EVs. Lithium Iron Phosphate (LFP) is another chemistry with relatively high power capabilities and better safety properties than the former chemistry [66]. The choice of chemistry will be a trade-off between energy, power, durability, safety and cost. If a battery is to be used in a light hybridization, the power capabilities may be more important than the specific energy, while the energy requirement may be more crucial when the battery is the main energy device.

The efficiency of Li-ion batteries is decided by the charge or discharge rate, the OCV and the internal resistance.

2.5 Fuel Cell Modelling

There exists various dynamic PEMFC models with different degrees of complexity. In Simulink®, there is a generic FC model in the Simscape library. This model uses a simple equivalent circuit to represent the polarization curve of a FC stack specified by experimentally obtained parameters. The model can be appropriate for average modelling, but less suitable for high frequency modelling. Another drawback is that important parameters like temperature, pressure and ECSA are not explicitly expressed. In the work preceding this thesis, this was found to be an

obstacle in the connection with a dynamic degradation model. In general, the parameter inputs give little freedom in performing influential parameter sensitivities and are difficult to obtain for state-of-the-art devices.

The latter is also a challenge when using extensive impedance models. By using electrical equivalent circuit (EEC) models with inductive and capacitive elements, high frequency phenomena can be modelled as discussed in Section 2.3.9. Such lumped-element models are relatively slow and, thus, not optimal for power balancing calculations. More appropriately, they can be used for evaluating the effect of transient conditions and ripple currents. The lumped-model parameters may typically be obtained from experimental testing and EIS. Such data exist in the literature, but rarely for high-performance state-of-the-art FCs. Open-source data on such devices are normally limited to polarization curves, performance data and operating limits. The FC modelling approach of this work is presented in Section 3.2.

2.6 Aircraft Powertrain

2.6.1 Distribution System

Conventionally, the electrical distribution systems of aircraft are based on AC. Due to the proposed use of DC energy sources for AEAs, DC distribution systems bring advantages. Large rectifiers from the energy sources are avoided and reactive power overrating is unnecessary for the DC-DC converters. Even for small short-range aircraft, the electric propulsion power requirement may be several MWs. This means that HVDC grids may be necessary to limit the current levels for AEA applications. In [1], DC voltages up to 3 kV are investigated for a typical regional AEA. With higher voltage levels, reduced weight and losses in the internal transmission system can be achieved. Simultaneously, requirements towards semiconducting devices and high insulation are increased [1]. Another interesting opportunity possibly enabled by the cryogenic hydrogen storage is superconductivity. Superconductivity requires extremely low temperatures, but is expected to enable a significantly reduced weight and increased efficiency of the electrical system [20]. The technology is currently at a low readiness level [1, 20].

2.6.2 Power Electronic Converters

The electrical power system of an AEA requires several converters and inverters. A converter of special interest is the DC-DC step-up converter required between the FC and the DC-link.

The FC converter can be unidirectional as no charging is expected. The simplest topology is the boost converter. For this converter topology, the FC current ripple will be decided by the switching frequency and the size of the input inductor. A faster switching and a large inductor will reduce the ripple content, but penalize the switching losses and the converter size, respectively. With certain topologies, above half the converter mass can be assigned to the power

inductor [67]. The design will be a trade-off between converter size, switching losses and component degradation and power losses induced by the ripple. Ripple limitation can efficiently be achieved by utilizing a multiphase interleaved boost converter. When several legs are switched with an equal phase shift, ripple cancellation is achieved. In addition to reducing the sizes of the passive components, increased reliability and efficiency can be obtained with an interleaved topology.

A concern is whether the converter should be galvanic isolated or not. In [62], a non-isolated multiphase boost topology is chosen for a hydrogen ferry application. The improved safety and reliability achieved by galvanic isolation are deemed too small to justify the corresponding implications of isolating the converter. Still, aviation poses different requirements than marine applications. Non-isolated topologies are advantageous with respect to weight, but brings increased needs for filtering of electromagnetic interference (EMI) [1]. Common mode (CM) noise, and to which extent semiconductors and other sensitive components are affected by the cosmic radiation, the temperature and the pressure conditions at high altitudes, are important design considerations. CM noise can typically propagate all the way from the electrical motors to the FCs, giving incentives for limiting the length of the circulations paths in the power system [68]. Depending on the frequency and the amplitude of the CM noise, reduction measures may be necessary to prevent a degraded FC performance.

Efforts must be made investigate the most beneficial converter topologies for the overall system. In [69], a 100 kW SiC boost converter for high-performance automotive application achieves a power density above 25 kW/kg. To realize this, a switching frequency of 100 kHz is utilized. Warncke et al. reports about 8.3 kW/kg for a 24 kW buck-boost converter for a more-electric aircraft application by using switching frequencies in the 100-300 kHz range [67]. The same converter power density is reported in [21].

In the case of ES devices, bidirectional converters are required unless the devices are to be directly shunted to the DC bus. This is to enable charging from excess FC power or braking power at the DC-link. Connecting ES devices through converters increases the power flow controllability and prevents SOC dependent DC-link voltages. Still, direct shunting may simplify the energy management and limit the additional cost and weight of large DC-link capacitors and DC-DC converters.

Inverters are required for the propulsion loads. This means that these devices must be designed for the bulk power generation from the energy devices. In [21], converter power densities and efficiencies of 8.3 kW/kg and 98% are presented. NASA is sponsoring inverter projects for high-voltage DC distribution systems in electric aircraft with power density targets of 19 kW/kg and 26 kW/kg[6] and efficiency goals of at least 99% [70]. Achieving such performances is essential to enable electric aviation on the MW-scale.

[6] With cryogenic cooling.

2.6.3 Powertrain Topology

There are various ways to set up a hybrid power system. In the case of a FC and battery hybrid, one can separate between two typical configurations. While FCs experience large output voltage variation from no load to full power, batteries have more constant voltage curves. This means that batteries do not necessarily require DC-DC converters, but may be shunted directly to the DC-link. This can be regarded as a passive battery hybrid. In the opposite case, both power devices are connected to the DC-link through converters and can be actively controlled. With the passive battery configuration, the DC-link voltage will depend on the battery SOC. It is therefore important that the system can tolerate the corresponding variations in the DC-link voltage. A clear advantage is that an extra converter can be omitted, which will reduce the system size and weight. Still, this configuration does not allow for directly controlling the battery power output. Including a separate converter between the DC-link and the battery will enable a more controllable power sharing between the power devices and ensure a SOC independent DC-link voltage. In both cases, a protection circuit should be included to prevent over-voltages at the DC-link in the case of failures or load loss. Typically, excess energy will be dissipated in a resistive break in such cases. With batteries, or other energy storage devices, in the system, parts of this energy can be harvested instead. Unwanted heat generation in the braking resistor can, thus, be limited. However, there will be restrictions given by the battery capacity, SOC and charging capability. Figure 2.17 illustrates how a FC-battery hybrid drive system can be realized with a passive battery configuration.

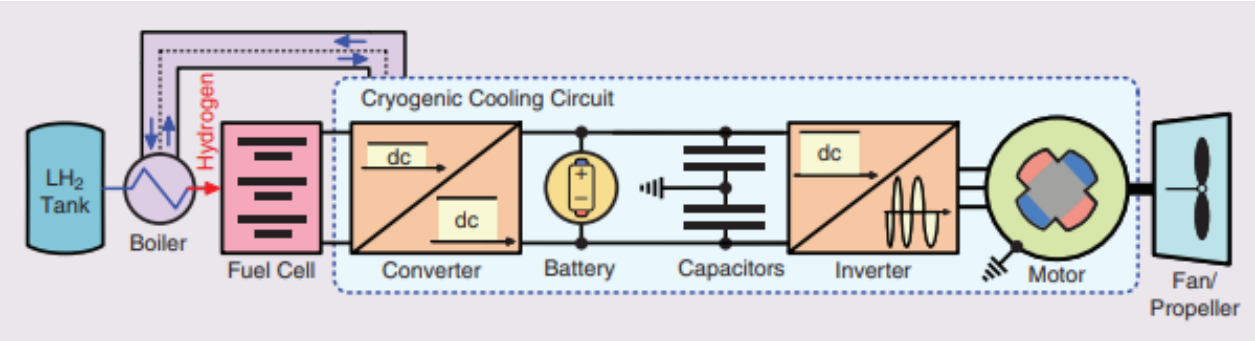

Figure 2.17: Generic fuel cell-battery hybrid powertrain with a passive battery configuration. Reprinted from [21].

The configuration also highlights the cryogenic cooling opportunity enabled by LH_2 storage. Using the chilled fuel to achieve superconducting power conversion and transmission can increase the system efficiency and, thus, reduce power losses and lower the parasitic weight of the aircraft cooling system. This may be a necessity to enable FC-powered propulsion for larger aircraft segments [3, 21].

The transition to electric propulsion enables the opportunity of distributed power generation and propulsion, unlike conventional bulky gas turbines. This means that significant changes

can be done to the aircraft design to optimize the electrical system topology and the aircraft aerodynamics. The aircraft drag can be reduced with smaller distributed nacelles and flexible wing designs [71]. Other benefits of distributed propulsion are increased reliability due to high redundancy, reduced noise and better vehicle control [72]. The latter suggests that electric aviation can enable shorter runway requirements for takeoff and landing [73].

To meet the power requirement of large propulsion systems, multiple stacks are needed. Depending on the application and each FC stack configuration, the FC architecture can be either series-distributed, parallel-distributed or a combinations of the two. An parallel configuration allows for the use of a common compressor, lowering the system size and weight [74]. With a series configurations, higher voltage levels and power outputs can be achieved [74].

2.6.4 Electrical Loads

The propulsion system is the dominating load of regional aircraft. High power density, efficiency and reliability are important design considerations for electric aircraft. Due to their high power density, permanent-magnet synchronous motors (PMSMs) are good alternatives for aviation. State-of-the-art motors are typically in the range of 5 kW/kg with efficiencies of 95% [21, 20]. NASA is sponsoring MW-level electric motor developments with power density targets of 13 kW/kg, while still achieving efficiencies above 96% [70].

All larger aircraft have significant non-propulsive loads, such as refrigeration, climate control, communication and lighting. A large share of this *hotel load* is assigned to cabin pressurizing and de-icing of the wings and nacelles [73]. In this work, the focus is limited to the load of the aircraft propulsion system.

2.7 Investment Costs Calculation

Power devices for aviation comes with large investment costs. To make useful economic estimations, the lifetime of the various components should be considered. By defining a time horizon T for the analysis, all relevant investments and residual values can be included and appropriately discounted. Assuming an initial investment cost K_0, a constant discount rate r and an estimated component lifetime L, the total investment is given as,

$$K_{tot} = K_0 \sum_{n=0}^{N-1} (1+r)^{-nL} - K_0 \frac{l}{L} \cdot (1+r)^{-T} \tag{2.42}$$

where N is the number of component investments required throughout the period and l is the remaining lifetime of the final component.

Chapter 3

Modelling Approach

3.1 Mission Profile for Regional Aircraft

In this report, the De Havilland Canada DHC-8 - Q300, hereafter referred to as *Dash 8*, is used as the reference aircraft. This is a 50-56 passenger regional turboprop aircraft, powered by two engines of about 1800 kW each [75]. The reference aircraft is chosen with the intention of addressing an aircraft segment where the energy density of batteries are likely to be insufficient and where FCSs will not be too heavy [3]. FCSs are highlighted as particularly suitable for this aircraft segment [3]. It is also an aircraft type currently being the basis of Universal Hydrogen's FC-electric aircraft project [76].

There exists advanced analytical tools for aircraft modelling, such as Piano, which can be valuable for detailed aircraft analyses. In this work, open-source historical flight data is preferred to ensure accessibility for possible further works. This also allows to study how varous aircraft parameters and different speed and altitude profiles affect the power profile of the flight, which can be valuable for electric aircraft design considerations. Another advantage of the approach is that it enables dynamic estimation of the environmental conditions[1]. The flight tracker, FlightAware.com, is used to obtain speed and altitude data for a typical flight mission. Together with the thrust equations presented in Section 2.1, an approximated mission profile can be calculated for the Dash 8. The chosen reference flight is between the two New Zealand cities of Auckland and Woodbourne. This route is chosen as it is one of the commercial routes operated by the reference aircraft where the logging data has a relatively high resolution. In addition, the flight has an appropriate range of just above 500 kilometres. Figure 3.1 shows the altitude and speed profile of a specific flight based on logging data.

[1] Environmental conditions such as air temperature, pressure and humidity influence the performance of the FCS and the aircraft cooling system.

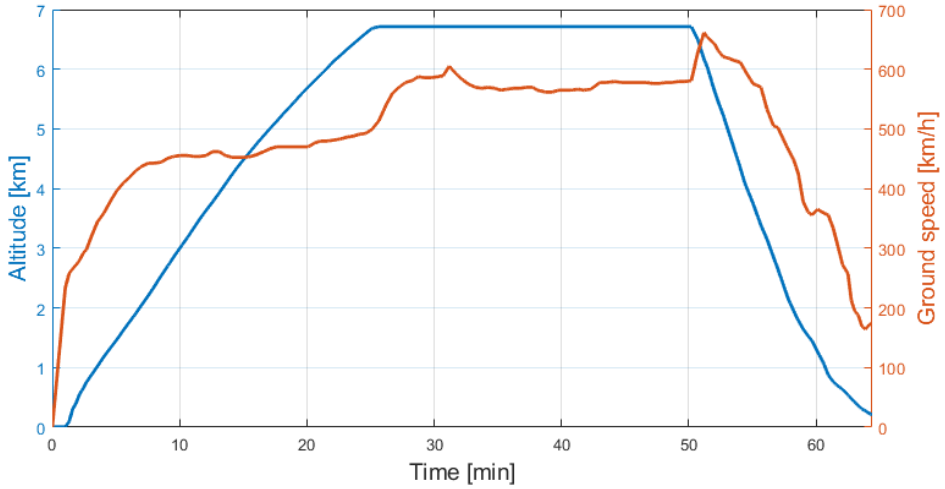

Figure 3.1: Reference flight logging data.

The reference flight represents a medium-range mission for the reference aircraft. Flight data are also obtained for a short-range, a long-range and a *standard profile* to be used throughout this work. The standard profile is developed by evaluating a large number of flights from appropriate turbo-prop aircraft in [10]. The distance and flight time of all four mission profiles are specified in Tab. 3.1. Unless otherwise stated, calculations are based on the reference mission between Auckland and Woodbourne.

Table 3.1: Mission profiles used in calculations.

Mission profile	Range	Distance	Time
Auckland-Woodbourne	Medium	526 km	~80 min
Newman-Perth	Long	1093 km	~150 min
Bodø-Evenes	Short	187 km	~30 min
Standard profile	Medium	407 km	~60 min

3.1.1 Reference Aircraft Specifications

Some aircraft specific parameters are required to perform power calculations. It can be challenging to find good data on the zero-lift drag of a specific aircraft. Also, it is reasonable to believe that an electric modification of an existing turboprop aircraft would bring certain changes in the zero-lift drag. If these changes are to be evaluated, the drag contribution from various parts, such as the wings, tails, fuselage and nacelles, should be considered in detail. This works limits itself to zero-lift drag estimations found in the literature. The same goes for the Oswald efficiency number. In [77], the zero-lift drag is estimated to be 0.027403 for the ATR-72. This aircraft is slightly larger than the reference aircraft, but can be expected to be in the same range. The corresponding Oswald efficiency number used is 0.75. In [78], the Dash 8 is estimated to

have a zero-lift drag of 0.02 by assuming a Oswald efficiency number of 0.85. These numbers are also coherent with the values of similar aircraft based on flight tests [79]. For simplicity, the Oswald efficiency number and the zero-lift drag are assumed to be 0.85 and 0.02, respectively, throughout the whole flight mission. The aspect ratio, wing area and propeller area of the reference aircraft are obtained from datasheets and presented in Tab. 3.2.

Table 3.2: Key parameters of the reference aircraft, Dash 8 Q300.

Technical	**Values**	**Weights**	**Values** [75]
Aspect ratio	13.36 [80]	Max. takeoff weight	19,505 kg
Oswald factor	0.85	Max. landing weight	19,050 kg
Zero-lift drag	0.02	Max. zero fuel weight	17,920 kg
Wingspan (net)	56.20 m^2 [75]	Max. payload	6,124 kg
Propeller diameter	3.96 m [81]	Fuel capacity	3,160 L (~2,500 kg)

Figure 3.2 shows the power profile calculated from the logging data[2].

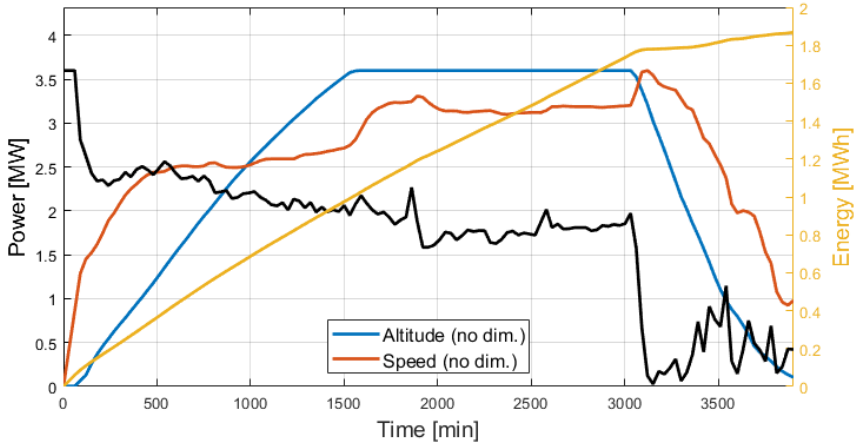

Figure 3.2: Reference flight mission profile.

The accumulated energy consumption throughout the flight is also illustrated. For the takeoff phase, which lacks logging data, full power is assumed for 60 seconds. To avoid large power spikes from inaccurate logging data, particularly during the climb phase, all logging points are averaged with a sampling time of 30 seconds. This makes the approach suitable for power balance calculations, but not evaluation of faster system dynamics. The resulting power profile is coherent with the expectations of a high power output during takeoff and initial climb that gradually decreases to a cruise power level of about 50% [10]. This mission profile will be used a the reference case for the rest of this work. Note that the mission profile only represents a typical, averaged case for the reference aircraft, which will vary from flight to flight. When changing

[2]The relevant numerical script can be found in Appendix F.1.

to a fully electric propulsion system, the aerodynamic efficiency could possibly change significantly through radical design changes, such as distributed propulsion [3]. Possible changes to the aerodynamic performance is not considered for the power calculations in this work.

3.2 Fuel Cell Modelling

3.2.1 Polarization Curve

There are different ways to model the VI characteristics of PEMFCs. To get a good model of a specific FC stack, experimental testing should be performed to obtain relevant parameters. In this work, no experimental testing is performed and an alternative approach must be applied.

To get a representation of a state-of-the-art high-performance FC stack, the datasheet of the 125-kW PowerCellution P stack is used as a reference stack [29]. Several such stacks are required to meet the aircraft power demand. Together with the voltage expressions presented in Section 2.3.2, the reference stack polarization curve is approximated by a combination of values from the literature and curve fitting. This procedure gives a close approximation of the real stack under the reference conditions, but may diverge from the real stack performance beyond these conditions. Furthermore, the mass transport region is not defined for the reference stack and must be estimated by the relations given in the literature.

For the crossover current density, the Pt loading and the ECSA, 5 mA/cm^2, 0.4 mg$_{Pt}$/cm^2 and 50 m^2/g$_{Pt}$ are chosen as default values by suggestions from SINTEF. A similar ECSA and Pt loading are presented in [27]. The active cell area of the reference stack must be estimated as it is not revealed in the datasheet. One of its predecessors, the EVO 2 stack, has a reported active area of 300 cm^2, a nominal stack power of 101 kW and a Pt loading of 0.35 mg/cm^2 [82, 83]. The 2017 Toyota Mirai stack, has been suggested to have an active area of 237 cm^2, a Pt loading of 0.3 mg/cm^2 and a nominal output power of 114 kW [84]. Based on the high Pt loading of the reference stack, an active cell area of 180 cm^2 is assumed for this thesis. This means that the rated current point of 450 A will correspond to a current density of 2.5 A/cm^2. A such high current density operation can be justified by the high Pt loading and the elevated operating pressures and temperature. Possible operation between 2.4-3.0 A/cm^2 has been suggested for the new Toyota Mirai stack, despite a lower Pt loading [85].

The oxygen transport resistance used for estimating the concentration losses at the cathode is chosen based on the experimental tests in [26] and [27]. In this way, the relation to ECSA loss can also be estimated for lifetime calculations. To adjust for the higher Pt loading in this work compared to [26], the transport resistances are scaled with a constant factor to achieve R$_T$ = 200 s/m at reference conditions, as was found in [27]. The resulting relation between the transport resistance, ECSA and operating pressure is illustrated in Fig. 3.3.

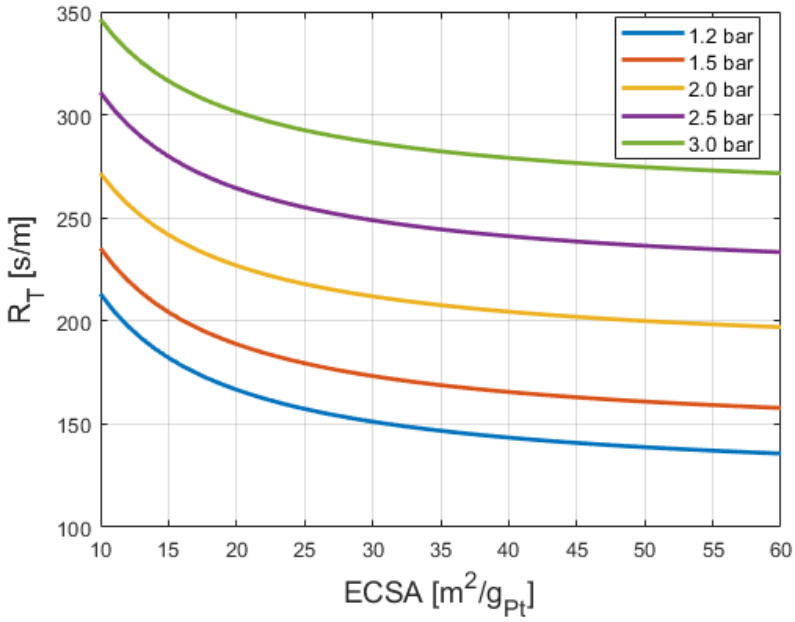

Figure 3.3: Oxygen transport resistance as a function of ECSA. Produced based on values from [26] and [27].

The oxygen transport resistance increases for higher cathode pressures. The resistance value are set by interpolating between the relevant pressure levels. For the reference operating conditions, with an absolute pressure of about 2.013 bar, R_P+$R_{Knudsen}$ = 94.34 s/m and R_{Pt} = 1846.9 s/m are used. One of the most difficult parameters to set is the exchange current density. This parameter, as well as the ohmic cell resistance, is decided by fitting[3] the model polarization curve to the reference stack curve. At reference conditions[4] the best fit is achieved at $i^*_{0,s} = 1.86 \cdot 10^{-6}$ and $R_\Omega = 0.018\ \Omega cm^2$. When fitting the parameters for both the reference pressure, 0 bar(g) and 1.6 bar(g), the overall best fit is achieved with $i^*_{0,s} = 1.78 \cdot 10^{-6}$ and $R_\Omega = 0.016\ \Omega cm^2$. The specific exchange current density and ohmic resistance found by fitting the reference conditions polarization curve are used for the model to achieve the best possible compliance with the reference stack at reference conditions. All relevant parameters are listed in Tab. 3.3.

[3] Using least squares error to fit curves.

[4] Reference conditions: 80°C operating temperature, 2.013 bar(a) cathode pressure.

Table 3.3: Fuel cell model parameters at reference conditions.

Reference case	Value	Unit
T^*	353.15	K
$P^*_{O_2}$	201.3	kPa
$i^*_{0,s}$	1.86e-6	A/cm^2
i_x	5e-3	A/cm^2
L_{Pt}	0.4	mg_{Pt}/cm^2
ECSA	50	m^2/g_{Pt}
γ	0.54	
A_{cell}	180	cm^2
R_{ohm}	0.0180	Ωcm^2
E^{rev}_c	67	kJ/mol
$R_P + R_{Knudsen}$	94.34	s/m
R_{Pt}	1846.9	s/m

Figure 3.4 shows how the polarization curve of the model compares to the reference FC stack at different operating pressures.

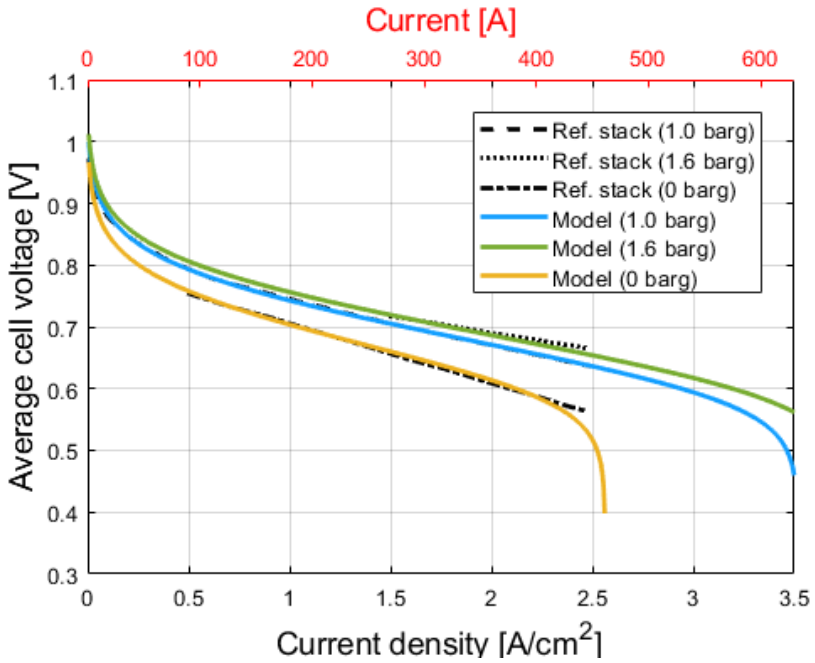

Figure 3.4: Polarization curve comparison between the proposed model and the reference fuel cell stack. Reference stack curves obtained from [29].

At reference conditions, 1 bar(g) and 80°C, the fit is very good. The model follows the reference stack curves quite closely also at ambient conditions and at 1.6 bar(g). At low operating pressure

the oxygen transport resistance appears to be a bit conservative, such that the mass transport region is reached at lower current densities than for the reference stack. At higher pressures the model present a slightly steeper slope in the ohmic region compared to the reference stack. These small deviations are not unexpected as the model parameters are mainly obtained from available data in the literature, and not the reference stack specifically. To achieve good compliance with the characteristics of a particular stack, a more detailed datasheet is required. Such data is obtained from circumstantial testing and will often be confidential, particularly for state-of-the-art products. Still, using the reference stack as a basis for curve fitting ensures that calculations in this work are within the typical range of high performance FC stacks, at least at reference conditions. In addition, the described approach should be valuable for future works where stack parameters can be obtained at a higher accuracy by experimental testing. Particularly, the model compliance with the reference stack is uncertain beyond the maximum current density point of 2.5 A/cm^2, as no data is presented in this region for the reference stack. Normally, it is desirable to operated outside the mass transport region during normal operation. In the case of FC-powered aviation, it could still be valuable to investigate how much power the FC can deliver during emergencies by entering this region. Similarly, conventional aircraft engines may operate with an increased performance during emergency situations at the expense of the engine lifetime [86].

With this estimated model, a FCS[5] with a fresh FC stack will have the specifications listed in Tab. 3.4 given the conditions and design of the reference stack[6].

Table 3.4: Power and efficiency specifications of the reference FC stack and the complete FCS at different altitudes.

		Sea-level	Cruise-level
	FC	FCS	FCS
Nominal power	130.3 kW	120.0 kW	109.64 kW
Max. power	149.7 kW	134.8 kW	121.5 kW
Peak efficiency	79.7%	62.7%	62.3%
Nominal efficiency	50.8%	46.8%	42.7%
Max. power efficiency	44.7%	40.1%	36.1%

3.2.2 Lifetime Calculations

FCs suffer from degradation mechanisms as described in Section 2.3.8. Early EoL will lead to increased costs due to numerous FC replacements. The durability is therefore a very important measure for the commercial feasibility of the FCs. FCH JU[7] have estimates on state-of-the-art

[5] The BoP components will be introduced in the following sections.

[6] 455 cells, 180 cm^2 cell area, 80°C operating temperature and 2.013 bar(a) cathode pressure.

[7] The Fuel Cells and Hydrogen Joint Undertaking.

and future targets for FCS lifetime in electric aircraft [87]. The 2017 estimate is a 5000 hours durability, while the targets for 2024 and 2030 are 15 000 and 20 000 hours, respectively. An operational life of 20 000 hours is also estimated for the reference stack by the manufacturer [29]. In this work, to evaluate the effect of the operating conditions, the semi-empirical model proposed by Kneer et al. [28] is used as a basis for degradation calculations. The model is derived with the assumption that loss of ECSA is the main driver for the FC voltage and power degradation. The main stressors were found to be the temperature, the relative humidity and the upper voltage potential [28]. In this work, the relative humidity is assumed constantly kept at standard conditions, such that the explicit variation in ECSA loss rate is limited to the operating temperature and voltage level. The impact of the two stressors are weighted by (3.1) and (3.2), respectively.

$$k_T = k_{T_0} \cdot exp\left(\frac{E_A}{R} \cdot \left(\frac{1}{T} - \frac{1}{298}\right)\right) \tag{3.1}$$

$$k_U = k_{U_0} \cdot exp\left(-0.5\frac{2F}{RT}(0.98 - V_{cell})\right) \tag{3.2}$$

The activation energy term, E_A = 28.6 kJ/mol, is based on [28], while the values for k_{T_0} and k_{U_0} typically are determined experimentally. The temperature-driven loss, expressed by k_T, follows a typical Arrhenius type dependence as suggested in the literature [23, 28]. The voltage-driven loss, expressed by k_U, follows a similar exponential increase, penalizing operation at high cell voltages. The corresponding ECSA loss is expressed as,

$$\frac{\Delta ECSA}{\Delta t} = (k_U + k_T)\frac{ECSA}{3600} \tag{3.3}$$

with a resolution of Δt. When the characteristics of the FCS are known, the voltage profile can be calculated as a function of the power profile. For the temperature, information about the cooling system is needed to acquire the FC temperature profile for each flight mission. If the cooling system is sized for the maximum power output, the operating temperature can be kept close to constant throughout all flight phases. To limit the size and parasitic losses related to cooling, elevated stack temperatures may be accepted during certain flight phases. Initially, the values for the ECSA loss parameters k_{T_0} and k_{U_0} are set to 1e-4 and 1e-5, respectively, to reflect experimental data measured at SINTEF. The estimation of these values will vary depending on the relevant FCS. The voltage and power degradation after 2500 operating hours at three different temperatures are depicted in Fig. 3.5, with the initial loss parameters.

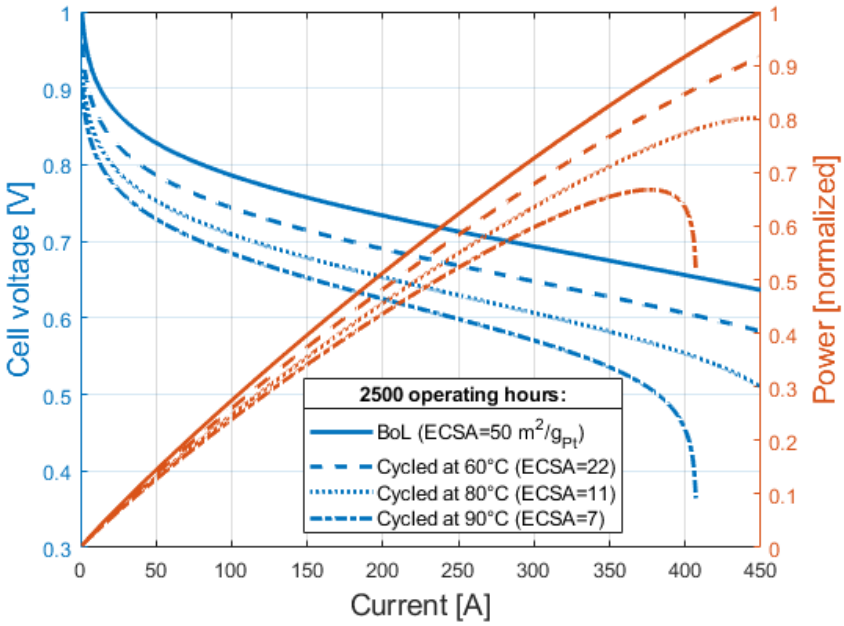

Figure 3.5: Voltage and power degradation after 2500 operating hours when cycled at 0.6V and different constant temperatures.

The EoL criteria is met at around a 60-65% ECSA loss in all cases. Given the ECSA loss rate and its estimated effect on the FC performance, the FC operating lifetime can be predicted as a function of both the operating temperature and the cell voltage. This is illustrated in Fig. 3.6 with the initial loss parameters[8].

[8]The translation from ECSA loss to operating lifetime is explained in Appendix C.2.

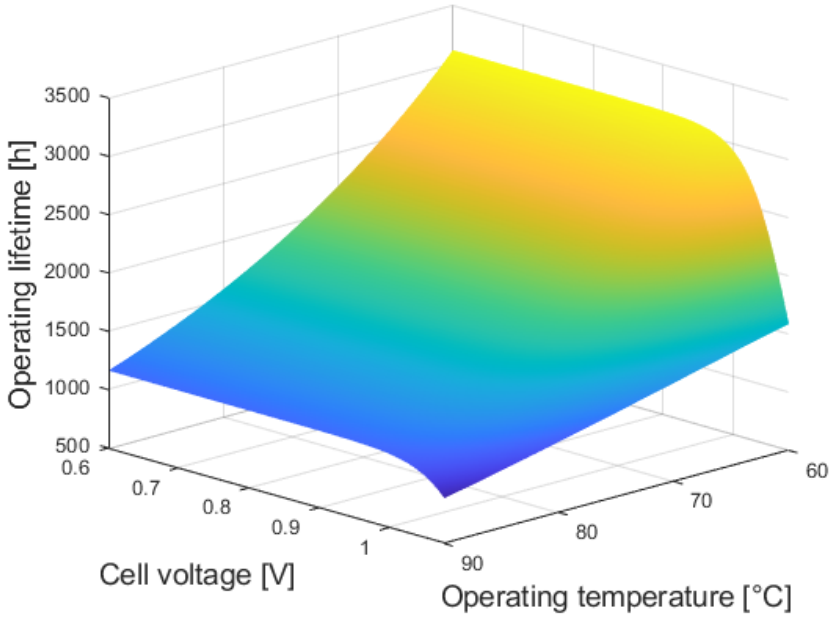

Figure 3.6: Operating lifetime sensitivity on temperature and cell voltage. Temperature-driven and voltage-driven loss parameters constantly kept at 1e-4 and 1e-5, respectively.

With the given parameters, the temperature-driven losses are much more prominent than the voltage-driven losses for the relevant voltage range. Even at low temperatures and beneficial voltage levels, these parameters lead to EoL within less than 3500 operating hours. This predicted lifetime is in the range of less modern FC stacks or for use in automotive applications [87]. The degradation model is indeed developed with automotive applications in mind [28]. Even though aviation is a relatively demanding application, it can be expected to have a more continuous power request and less start/stop cycles than a passenger car. In addition, for redundancy and scalability the complete power system will consist of several FC stacks. This yields a flexibility to keep some stacks in idling mode rather than operating all of them at high voltage levels during low power flight phases. It is therefore reasonable to believe that the temperature-driven losses will be dominant for the purpose of aircraft propulsion. This means that the degradation rate will be very sensitive to the choice of the temperature-driven loss parameter k_{T_0}. This sensitivity on the operating lifetime of the FCs is illustrated in Fig. 3.7.

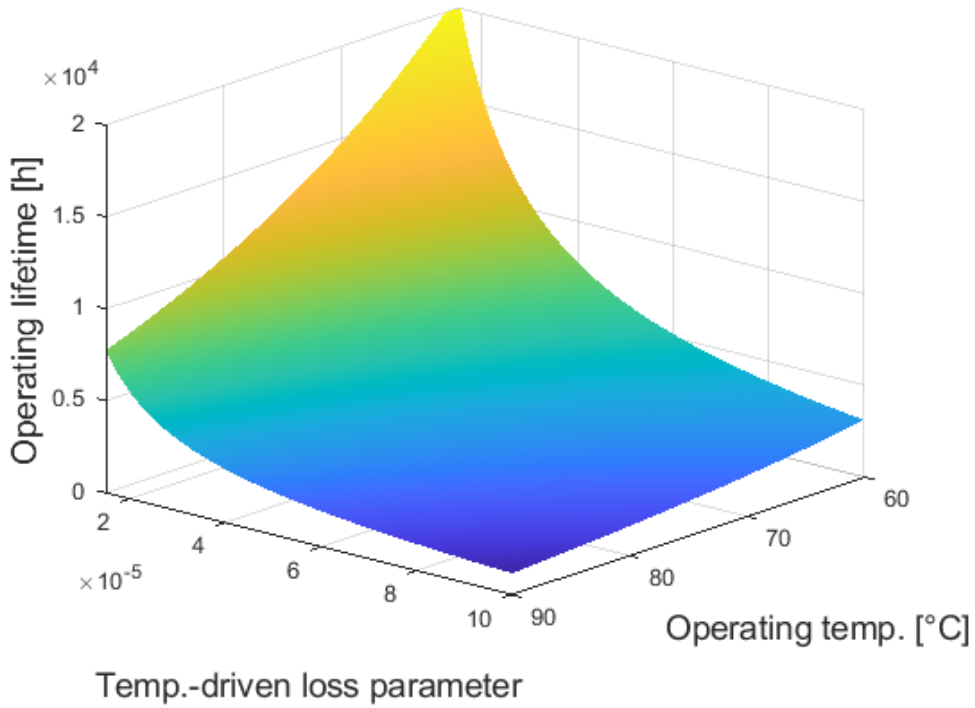

Figure 3.7: Operating lifetime sensitivity on temperature and temperature-driven loss parameter. The cell voltage is constantly kept at 0.6V.

Here, k_{U_0} is kept as a tenth of k_{T_0} throughout the whole sensitivity range, $k_{T_0} \in [1.5 \cdot 10^{-5}, 10^{-4}]$, yielding a negligible impact for the relevant cell voltage levels. At 60°C, the temperature-driven loss parameter must be reduced to 18% of the initial value to achieve the target lifetime of 20 000 operating hours. This value will give an operating lifetime of 10 800 and 8100 hours at 80°C and 90°C, respectively. For the rest of this work, a temperature-driven loss parameter of $5 \cdot 10^{-5}$ will be used, as it gives operating lifetimes within the expected range for state-of-the-art FCs in aircraft applications. The voltage-driven loss parameter is kept at 10^{-5}. It is evident that the loss rate increases significantly at higher operating temperatures. This should be considered when sizing the cooling system.

3.2.3 Cooling System

FCS Cooling Loop

To make calculations on the parasitic power losses related to cooling of the FCS, some assumptions must be made regarding the frictional pressure loss of the cooling system. As the reference FC is a stack module only, no information is given regarding the cooling system. In the datasheet of the Nedstack FCS 10-XXL stack, such information is given [88]. For the use of glysantin coolant, the pressure drop in the cooling system is limited to 0.45 bar. For simplicity, this pressure drop is considered representative also for the reference stack at a nominal power

level, with a linear relation to the coolant mass flow rate. This means that the pumping power requirement for the FC cooling loop will vary with the square of the coolant mass flow rate. The coolant temperature difference between inlet and the outlet of the FC is kept at maximum 10°C to prevent a poor temperature distribution and the corresponding consequences on the FC durability and performance [37]. The coolant pump is assumed to operate with a constant efficiency of 58% [37].

The highest heat generation will occur during the power intensive takeoff and initial climb. As the FC operates at relatively low temperatures, the natural convection will be quite low compared to conventional combustion engines. The maximum coolant outlet temperature is 90°C [29]. A classical 50/50 WEG[9] coolant has a density and specific heat capacity of about 1036 kg/m^3 and 3.53 kJ/(kg·K) at 80°C, respectively [25]. At increased stack temperatures, the constraint $\Delta T \leq 10$°C limits the heat rejection from the stack to the coolant. However, the heat transfer between the coolant and the ambient air will be improved. By using the above assumptions, the required coolant flow and the pump power requirement for the FC cooling loop can be calculated. Figure 3.8 shows the FCS power and heat generation, and the corresponding cooling requirements, based on the FC operating current density.

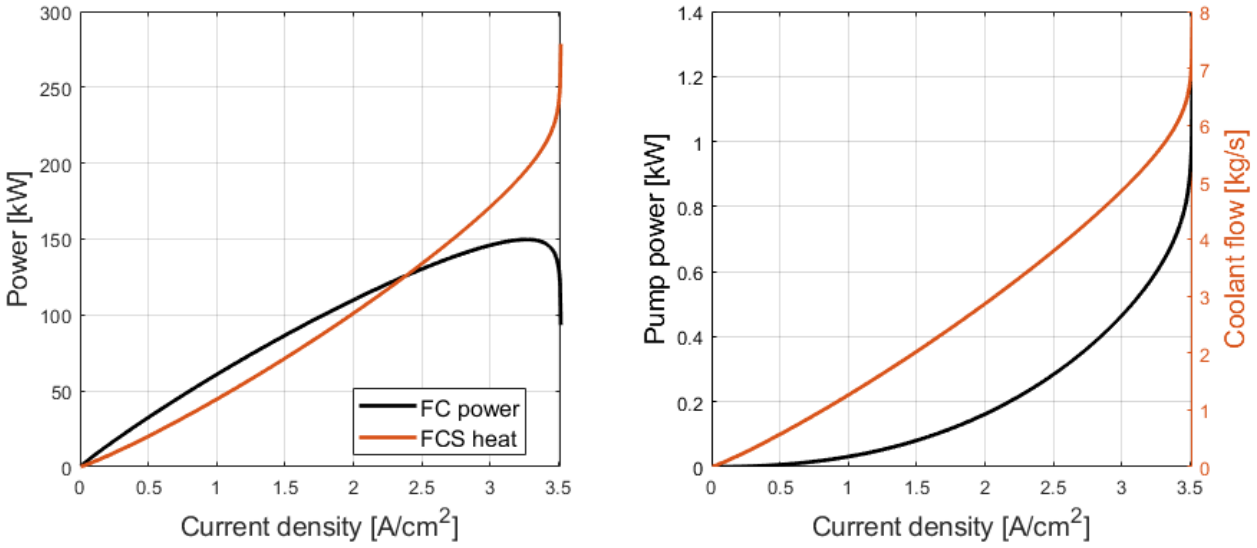

Figure 3.8: FC power output and heat generation, and the corresponding coolant flow and pumping power requirements, based on the FC operating point.

For completeness, the HEX requirement should also be considered.

Heat Exchanger

A complete representation of the entire cooling system brings very high complexity [39]. Still, it is difficult to make good evaluations on the FCS without considering how to reject all the

[9] Water-Ethylene glycol with at 50/50 volume concentration.

excessive heat. In [89], the thermal management system (TMS) of an AEA are explored. One of the investigated aircraft, the PEGASUS EAP, has similar dimensions and specifications as the reference aircraft in this work. A linear relation is developed between the mass of the TMS and the aircraft heat generation [89],

$$m_{HEX} = 0.407 \cdot 10^{-3} \cdot Q_{HEX} + 1.504 \tag{3.4}$$

This relation is adopted and used in this work to represent the HEX requirement towards the ambient air. In the sensitivity studies performed in [89], the linear trend was found to be reasonable as long as the coolant inlet temperature was kept above 60°C[10]. A complete analysis should examine the impact of environmental conditions and the airspeed of the aircraft in more detail. These effects can be dramatic on the performance of the cooling system [89].

Cooling System Specifications

It is desirable to express the power density of the cooling system as a function of the heat power generation, such that it profits from a more efficient FCS. The Ballard FC VeloCity-HD, the PowerCellution Heavy Duty System 100 and the PowerCell MS-100 are all examples of state-of-the-art high performance FCSs with net output powers of 100 kW [90, 91, 47]. The maximum heat generation from these FCSs are listed to be 150 kW. Only the Ballard FCS explicitly specifies its cooling system, including coolant pump, piping, control valve and freeze protection, with a combined weight of 44 kg. In comparison, the maximum heat output of each reference FCS is estimated to 142 kW[11] This heat generation occurs at the manufacturer's rated current and at the maximum cruising altitude[12]. Using data from these comparable FCSs to obtain a cooling system power density of 3.41 kW_{heat}/kg should therefore be appropriate for the reference FCS cooling loop. This part of the cooling system is assumed to be unaffected by the operating temperature of the FC stack due to the $\Delta T_{coolant} \leq 10^{\circ}C$ requirement. In reality, a higher operating temperature would lower the active cooling requirement to some extent, due to an increased natural convection.

On the other hand, the HEX is subject to important design considerations. Even though higher operating temperatures accelerate certain FC degradation mechanisms, the cooling system must be optimized to limit the overall size and weight [3]. The highest FC power requirement occurs when the ambient temperature is the highest and the airspeed is the lowest. Thus, it may be beneficial to sacrifice some elevated operating temperatures during takeoff to avoid too much oversizing of the HEX. A higher operating temperature and downsizing of the cooling system are highlighted as important focus areas for the FC manufacturers [3]. An important trade-off is how the increased FC operating temperature affects the expected lifetime of the de-

[10] With a worst-case ambient temperature of 40°C.

[11] Heat generation limited to FC stack and compression system.

[12] Assuming inefficiencies in the FCS are directly translated to heat.

vice. In Fig. 3.9, the impact of spending a fraction of the flight at 90°C is estimated by the lifetime model with 80°C as the standard temperature.

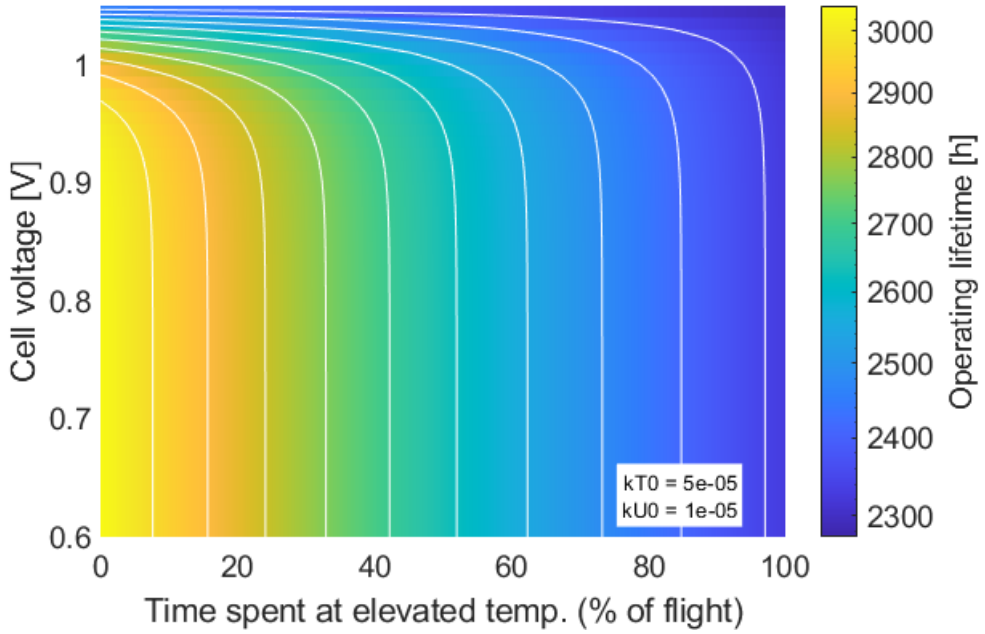

Figure 3.9: Operating lifetime sensitivity on cell voltage and flight fraction spent at elevated temperature (i.e. 90°C). The reference temperature of 80°C is assumed when not elevated.

The increased degradation is small for shorter periods at the maximum operating temperature. To adjust for how the temperature difference ΔT_{HEX} between the ambient air and the liquid coolant influences the cooling system, the HEX mass requirement is scaled as in (3.5). From (2.35), this is valid under the assumption of a constant heat transfer coefficient and a linear relationship between the weight and the surface area.

$$m_{HEX} = \left(0.407 \cdot 10^{-3} \cdot Q_{rad} + 1.504\right) \cdot \frac{\Delta T_{HEX,ref}}{\Delta T_{HEX}} \tag{3.5}$$

Here, $\Delta T_{HEX,ref} = (80°C - 40°C)$ and ΔT_{HEX} will depend on the temperatures of the FC stack[13] and the ambient air. At an elevated operating temperature of 90°C and a worst-case ambient temperature of 40°C, the heat rejection requirement translates to a 47 kg HEX for each FC stack[14]. With the reference temperature of 80°C, the corresponding mass is 59 kg. If the FC is sized to operate at its maximum power point (MPP) during takeoff, an 83 kg HEX would be required to reject all heat. The weight profit of increasing the FC operating temperature is translated to the HEX only, not the FC cooling loop. Keep in mind that the FC cooling system should be dimensioned for the heat generation towards EoL, which will be significantly higher than for

[13] Coolant outlet temperature assumed equal to stack temperature.
[14] Assuming maximum cruise altitude operation at manufacturer's rated current.

the fresh FC. The linear HEX power density will be 2.39 kW_{heat}/kg (3.03 kW_{heat}/kg[15]). Adding the FC cooling subsystem to the calculation, the overall cooling system will have a power density of 1.37 kW_{heat}/kg (1.56 kW_{heat}/kg). This is in the same range as the oil-air heat exchanger reported in [92].

3.2.4 Air Compression Model

The U.S. Department of Energy (DoE) have developed technical targets for air compression systems for transportation FCSs [45]. For 2020, the listed compressor and expander efficiency targets are 75% and 80% at full air flow, respectively. The corresponding combined efficiency of the motor and motor controller is 90%. The efficiencies will decrease at lower air flows, but these target efficiencies are expected for the whole flow range in this work to limit the complexity. It is important that the compressor can ensure sufficient operating pressures despite changing environmental conditions. Figure 3.10 shows the possible effect of not pressurizing the system at different altitudes.

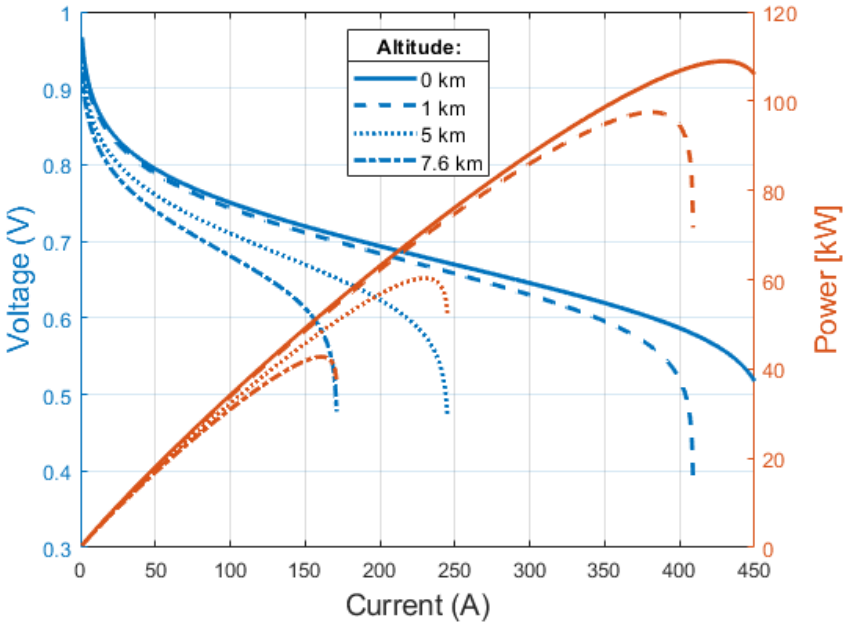

Figure 3.10: Modelled effect of operating with a non-pressurized system at elevated altitudes on voltage and power curves.

The low concentrations of oxygen will lead to significantly worse performance, particularly at high current densities. Note that at such low operating pressures, the validity of the FC model is uncertain. Still, the mass transport losses related to low oxygen concentrations at the catalyst are increasing at low pressure levels, as expected. The operation at high altitudes has been

[15] If elevated temperature is allowed during takeoff.

shown to have severe degrading effects on the stack performance, even at relatively low altitudes [93, 94]. To avoid this performance degradation, a pressurized system where the compressor ensures a constant air pressure will be assumed for this work. The maximum cruise altitude of the reference aircraft is 7620 m [75]. At such altitudes, the ambient pressure is about 0.38 bar based on (2.37) and the ISA[16] standard. Given that the polarization curves of the reference FC stack are obtained at a standard atmospheric pressure of 1.013 bar, the ambient air must be compressed from 0.38 bar to 2.013 bar to achieve the 1.0 bar(g) performance in the datasheet [29]. In addition, the compressor must account for the internal air pressure drop in the FC stack. The pressure drop is modelled by the oxygen transport resistance as described in [27]. In this way, the pressure drop has a linear relation with the stack current, ranging from 0 at zero power to 0.49 bar at the maximum power point (MPP). In reality, the relation between the pressure drop and the current is not necessarily linear, particularly not at higher current densities. Figure 3.11a shows the compressor power, the expander power, the net FC output power and the system efficiency[17] for increasing altitudes at the MPP. Figure 3.11b shows the gross and net power output and the corresponding stack and FCS efficiencies at the maximum cruising altitude and the reference FC operating pressure.

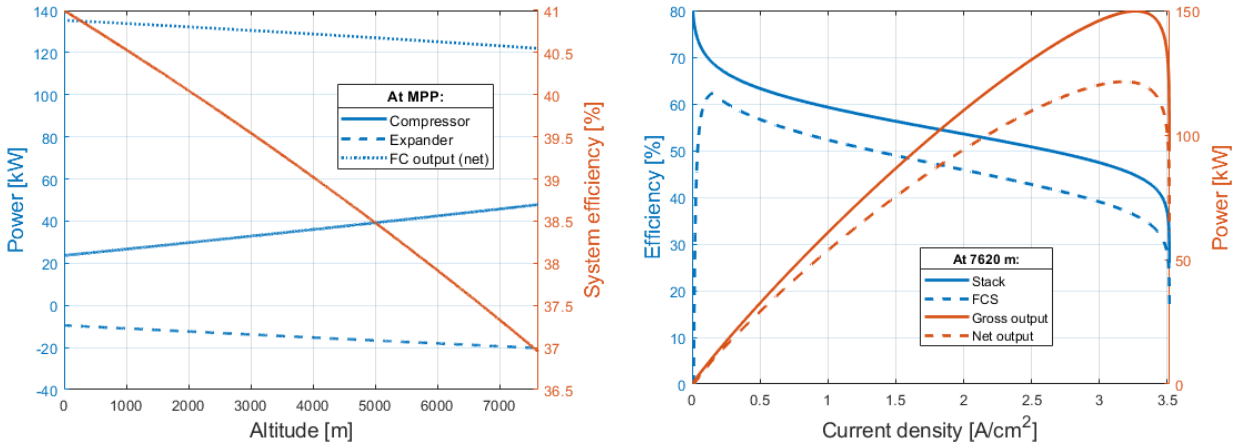

(a) Air compression at increasing altitudes.

(b) Operation at maximum cruising altitude.

Figure 3.11: The impact of elevated altitudes on the fuel cell stack and system.

The system efficiency suffers significantly from the compression requirement at high altitudes. For a specific FCS, tests should be performed to find an optimal trade-off between the compression work requirement and acceptable operating pressures during the different flight phases. These tests should not only consider the operating efficiency, but also the impact low oxygen concentrations will have on the FC lifetime and the dynamic response time. In this work, the reference pressure is assumed optimal for all flight phases.

[16] ISA = International Standard Atmosphere.

[17] The system efficiency is here solely based on the FC stack and the parasitic power consumption of the compression system.

At full power, maximum altitude and an air excess ratio λ=2.0, about 18.4% of the gross FC power is consumed by the compression system. At sea level, the same number is around 9.5%. DoE targets a 10% power consumption from the air compression at full FC power for transportation FCSs operating at 2.5 bar [45]. This indicates that the compressor and expander calculation model is in the right range for transport applications. Some variations is expected depending on the design and efficiency of the components. To achieve an accurate model for a specific FCS, the system should be tested for the relevant operating range and at different ambient conditions. When compressing air from ambient pressure to 2.013 bar, the air temperature will be above the FC operating temperature if no heat is removed. Instead of modelling the heat rejection in a dedicated air intercooler, the heat generation of the compressor is added to the FC heat load based on the compressor efficiency, in this work.

Dimensioning Criteria

The DoE air compression targets for FC transport applications suggest an air compression system weight of 15 kg for a 80-kW FCS with a net input power of 8 kW, yielding a power density of 0.533 kW/kg [45]. The comparable FCS in the Toyota Mirai possess a compressor with a maximum power output of 20 kW [95]. A comparison with automotive applications should be carefully conducted due to the altitude requirements of aviation. Automotive FCSs will also have a more fluctuating power requirement and may operate with very high air flow stoichiometries to avoid oxygen depletion at the cathode [46]. The nominal operating pressure of different FC stacks will also vary, such that comparisons may be inadequate. Figure 3.12 shows the compressor power requirement for different scenarios throughout the mission profile with a constant air stoichiometry of 2.0. The effect of allowing a decreased stoichiometry of 1.5 at maximum power is also illustrated.

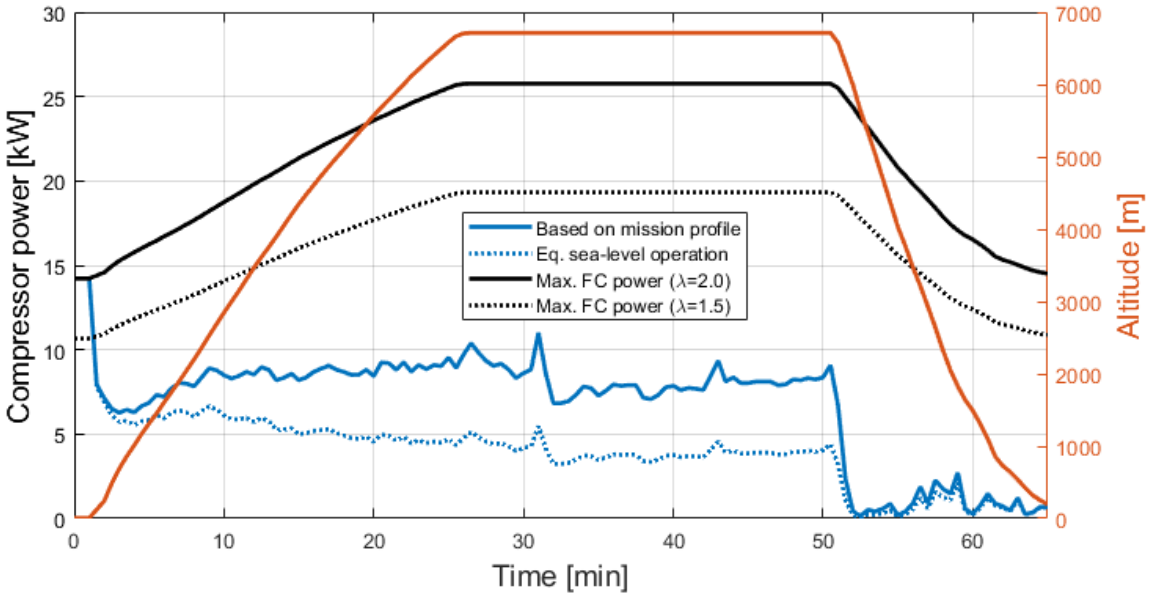

Figure 3.12: Compression system power requirement based on different dimensioning scenarios.

The most conservative dimensioning approach is demanding the maximum aircraft power at the maximum cruise altitude. This is illustrated by the solid black line for the reference mission profile. The actual compression power requirement for the reference flight is represented by the solid blue line. Due to the decreased compressor efficiency at low power levels, one should be careful with oversizing the device [45]. For the optimization model in this work, the dimensioning criteria is given by the specific mission profile and a stoichiometry $\lambda = 2.0$. Thus, it can be expected that the compressor can operate beyond the mission profile power curve in the case of emergencies, if the air stoichiometry is lowered. Note that a final compression system dimensioning should consider power and response time requirements given by aircraft regulations.

3.3 Hydrogen Tanks Sizing

In this work, both compressed storage in cylindrical tanks and cryogenic storage in spherical tanks are considered. The two storage technologies are hereafter simply referred to as cryogenic (cryo.) and compressed (comp.) storage. If not explicitly stated, compressed storage is used as the basis for calculations. This technology is assumed have a potential of commercialization within a shorter time frame than cryogenic storage. Note that as the industry turn towards larger aircraft and longer ranges in the future, the gain of cryogenic storage will increase [3]. For all calculations, tanks with an area-specific mass of 64.3 kg/m^2 are assumed[18]. This is not necessarily representative for an optimized cryogenic tank, which may vary highly depending on

[18]Estimated based on the 700 bar Toyota Mirai tank [13].

the insulation requirement. Investigating material technology and tank optimization in relation to cryogenic tanks are interesting and important parts of enabling hydrogen aviation. In [96], this is investigated with considerations on both geometrical, mechanical and thermal aspects. However, the area-specific mass of the tank wall is assumed constant in this work to limit the complexity. Figure 3.13 illustrates how a higher weight efficiency can be achieved by cryogenic storage in spherical tanks compared to compressed tanks with cylindrical geometries.

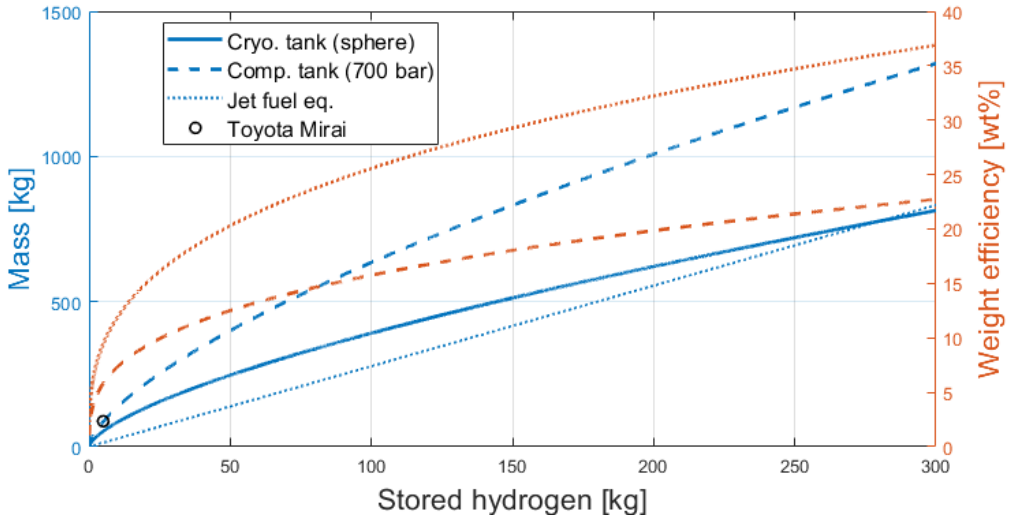

Figure 3.13: Comparison of cryogenic tanks with spherical design and 700 bar compressed tanks with cylindrical design. The Toyota Mirai tank mass and the mass of the jet fuel equivalent energy are illustrated as benchmarks.

Despite using a conservative area-specific mass equal to that of the Toyota Mirai tank in these calculations, the cryogenic tanks have a significantly higher weight efficiency due to the reduced surface area compared to compressed tanks. The mass of the 700 bar tanks used in the Toyota Mirai and the jet fuel equivalent mass are also highlighted as reference points. Given the constant area-specific mass of the tank material, a higher weight efficiency can be achieved as the tank volume increases. This is beneficial for energy-intensive applications like aviation. Note that the estimated weight efficiencies do not account for aircraft space restrictions, but assume that all the fuel can be stored in one large tank. Unless drastic aircraft design changes occur, several tank modules may be required, limiting the possible gain of high volume to surface area ratios. The optimal design should consider how the tanks can be fitted into the aircraft. ZeroAvia has shown concepts of both external tanks attached to the wings and tanks integrated inside the wings for their six-seat Piper M hydrogen aircraft [97]. Universal Hydrogen plans to use compressed hydrogen modules that can be fitted into the Dash-8 Q300 fuselage by removing two seat rows [76]. Airbus revealed different possible fuel tank locations for their zero-emission concept aircraft, whereas all the concepts are based on liquid hydrogen storage [4]. The optimal way to fit hydrogen tanks into the aircraft will depend on the design of the aircraft, the size of the tanks and the choice of storage technology. This is not only a volumetric consideration, but will

also affect the aircraft centre of gravity and stability. These considerations are deemed out of the scope of this work. However, the modelling approach of the flight missions allows for translating any excessive tank volumes into an equivalent drag force contribution and a corresponding mission power and energy increase. This can be further elaborated and utilized in future works.

3.4 Battery Modelling

The *Nanophosphate® High Power Lithium-Ion ANR26650M1* from A123 Systems is used as the reference cell for the battery modelling [98]. These lithium iron phosphate ($LiFePO_4$) cells have high discharge capabilities, achieving power densities above 2 kW/kg. The energy density is more moderate at around 108 Wh/kg. For the application of power boosting during demanding flight phases, the power output is expected to be limiting rather than the energy content. The choice of this reference battery is, thus, justified by its high power capabilities, as well as the safety associated with the $LiFePO_4$ chemistry. These batteries have excellent thermal stability and can endure high discharge rates without significant degradation. In the case where the battery is expected to have a more prominent role than power support, reference battery cells with higher energy densities should be considered. Another advantage with the chosen reference battery is that appropriate data to model charge and discharge behaviour, as well as the temperature and aging effects, are available through the Simscape library in Simulink®. Normally, such data must be obtained by experimental testing. To enable the use of these parameters, the same modelling approach as in the Simscape block is used in this work [99]. The charge and discharge models are described in [100]. The Li-ion discharge model is introduced here as it is essential for the estimated battery characteristics used in the power system optimization,

$$V_{batt} = E_0 - K \cdot \frac{Q}{Q - it} \cdot it - R \cdot i + Aexp(-B \cdot it) - K\frac{Q}{Q - it} \cdot i^*. \tag{3.6}$$

where

V_{batt}	=	battery voltage [V]
E_0	=	battery constant voltage [V]
K	=	polarization constant [V/Ah]
Q	=	battery capacity [Ah]
it	=	actual battery charge [Ah]
A	=	exponential zone amplitude [V]
B	=	exponential zone time constant inverse [$(Ah)^{-1}$]
R	=	internal resistance [Ω]
i	=	battery current [A]
i^*	=	filtered current [A]

The polarization constant, the exponential zone amplitude and the exponential zone time constant inverse are obtained directly from the $LiFePO_4$ preset model in Simulink® to achieve the same cell behaviour both in optimization calculations and in simulations. The constant current discharge and constant power discharge curves are shown in Fig. 3.14a and Fig. 3.14b, respectively.

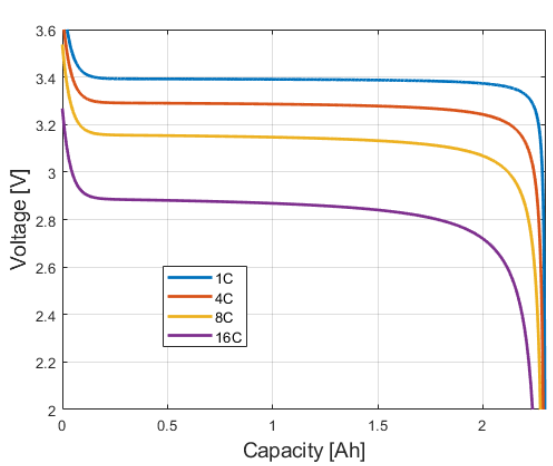

(a) Discharge characteristics for various C-rates.

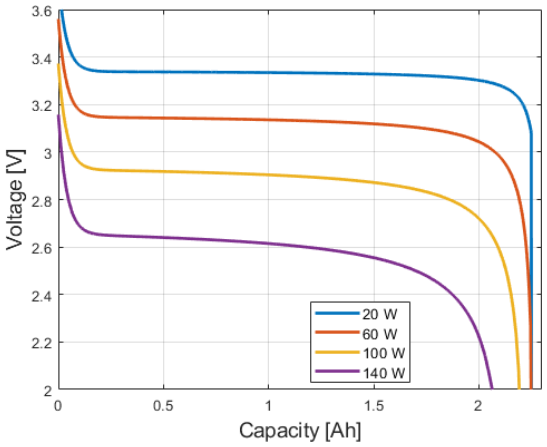

(b) Discharge characteristics for various power rates.

Figure 3.14: Discharge characteristics for the reference battery cell.

The discharge curves show good compliance with the ones provided by the manufacturer, as expected [98]. No Peukert effect[19] is explicitly modelled, but the capacity is still limited by the cutoff-voltage limit and the increased losses at higher discharge rates. Thus, if the battery cells are discharged at a high rate, the effective capacity will suffer. This trade-off between power and energy will depend on the required load power. In the case of a power-intensive load, high discharge rates can be accepted if the duration and energy requirement are sparse. Another concern is the thermal battery limits. This will most often be decisive for the continuous current rating. For the optimization calculations, temperature effects on the battery discharge curves are not considered, but operation above the continuous current limit given by the manufacturer is not allowed. The preset $LiFePO_4$ cell model has the parameters given in Tab. 3.5.

[19] Peukert effect = The loss of available capacity at increasing discharge rates.

Table 3.5: Key parameters for A123 Systems' lithium iron phosphate ($LiFePO_4$) battery cells obtained from datasheet and Simulink® preset model [98].

Parameter	**Value**
Nominal voltage	3.3 V
Rated capacity	2.3 Ah
Internal resistance (R)	0.014 Ω
Cut-off voltage	2.475 V
Fully charged voltage	3.748 V
Constant voltage (E_0)	3.4265 V
Polarization constant (K)	0.000645 V/Ah
Exp. zone amplitude (A)	0.38019 V
Exp. zone time constant inverse (B)	26.5487 $(Ah)^{-1}$
Max. continuous discharge	70 A
Core cell weight	70 g
Max. operating temperature	60°C

The resistance will contribute to a significant heat generation and lowered efficiency at high discharge rates. The power loss is calculated as [99],

$$P_{loss} = (E_0 - V_{batt}) \cdot i \tag{3.7}$$

where V_{batt} and i represent the battery voltage and current, respectively. At high discharge currents, the losses will be dominated by the ohmic losses. Thus, the internal resistance is an important measure for the discharge rate limit of the battery. Figure 3.15 shows the estimated power loss, and the corresponding efficiency, of the battery cells at different power output levels.

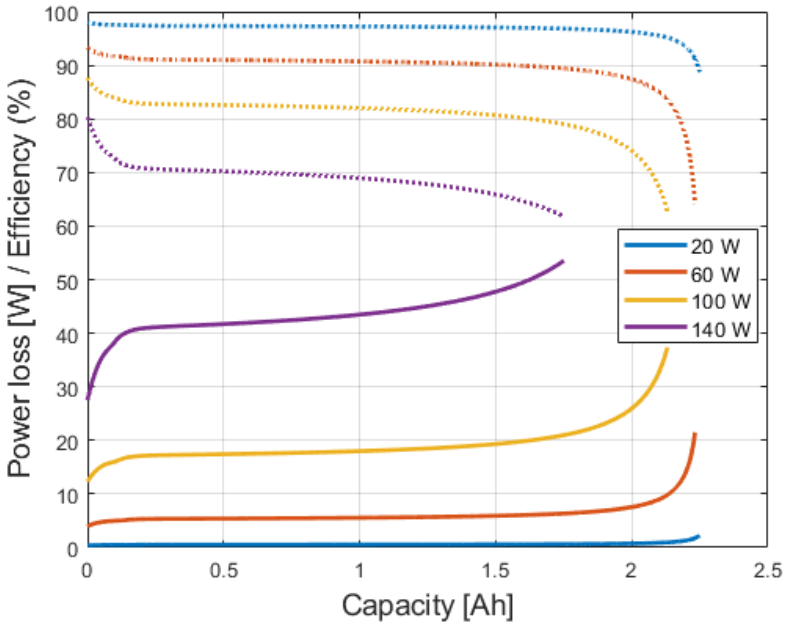

Figure 3.15: Battery cell power loss at different power outputs. The dotted lines shows the estimated operating efficiency.

The heat generation is large at high discharge rates. As long as the continuous current limit is obeyed, the battery is assumed to be able to effectively reject all heat, but the battery heat generation is considered for the sizing of the aircraft HEXs. In this way, excessive discharge rates will be penalized in weight optimizations. For these calculations, the maximum operating temperature of 60°C is used. Even at high power outputs, the battery will normally operate at much higher efficiencies than the FC. At nominal operation, the battery has an energy density of about 108 Wh/kg[20] on cell level and 73 Wh/kg on system level[21]. As the reference cell does not reflect the rapid capacity development batteries have experienced the last decade, a sensitivity on the energy density is also investigated in the Section 6.2.

3.5 Energy and Power Calculation

Both the energy and the power requirement of the engines can be estimated from the mission profile model. To obtain the power and energy requirement of the FC power system, the electrical drivetrain efficiency must be considered. In [3], an optimistic engine and power management and distribution efficiency of 97% is used as a basis. A battery to shaft efficiency of 92% is assumed for electric aircraft in [73]. Similarly, a slightly more conservative efficiency of 90% is assumed from the FCS to the motor shaft in this work. This means that at the maximum engine power of 3.6 MW, 4.0 MW will be consumed from the power system. Note that in reality,

[20] Cell weight = 70 g [98].

[21] Assuming a system to cell gravimetric ratio of 0.672 for cylindrical cells [101].

the drivetrain efficiency will vary within a certain range during operation. To calculate the fuel requirement, also the efficiency of the FC and its surrounding components must be taken into account. In addition, there are regulations on how much excess fuel an aircraft must carry as a safety measure. This includes such as the contingency fuel, the alternate fuel, the taxi fuel and a final reserve. These requirements will vary from mission to mission. For simplicity, the block fuel is constantly set to be twice the trip fuel in this work. This means that the hydrogen and tank requirement will be based on twice the actual energy consumption. In the case of cryogenic storage, the boil-off rate is assumed to be negligible due to the tank insulation and the continuous energy consumption throughout the flight. The input power at idle is set to 1 kW for the FCS to model the low FCS efficiency at low current densities. According to the 2020 technical targets from DoE, the idle power of the compression system alone should be about 0.5 kW for an 80 kW stack [45]. Note that no aircraft hotel loads are considered for the optimizations.

3.6 Powertrain Topology

As the reference FC has a gross power output around 125 kW, a large number of stacks are required to meet the peak load. With a DC-link voltage of 1 kV, maximum two reference stacks can be put in series in a voltage step-up configuration. The reference FC manufacturer is reported to not offer series connection possibilities for their stacks [62]. Thus, minimum 32 reference stacks must be paralleled to supply the takeoff power of 4 MW[22]. It is reasonable to believe that the total FC volume and weight could be reduced by using larger and less stacks. However, using a high number of small stacks increases the aircraft and powertrain design flexibility and may ease the FC cooling. The total number of required stacks will vary with the oversizing factor, the parasitic power consumption of the BoP components and the possible battery hybridization.

Increasing design variables like the cell area or the cell count of each FC stack is not necessarily viable for the reference stack due to cooling and reactant supply limitations. These variables should be decided by the manufacturer for the given application. The reference stack is, thus, not specifically designed to facilitate optimal conditions for the power converters in terms of duty cycles and current ratings in this work. However, to avoid limiting the FC size optimization to a whole number of paralleled stacks, oversizing of the FC is realized by changing the total cell count in the complete FCS. This means that the optimal number of stacks may not be an integer. To evaluate the conditions on stack level or cell level, the full load can be divided by the stack count and cell count, respectively. In this way, the cell count and voltage range of each stack remain unchanged for all FC sizing alternatives.

For simulations, the system is modelled on the stack level with a DC-DC converter separating the FCS and the DC-link. For hybridization cases, the battery[23] is directly shunted to the DC-link. In this way, a large number of additional power converters are omitted. However, the

[22] Assuming a 90% efficiency from FC to shaft.

[23] Adjusted for stack level by dividing the number of parallel battery cells on the total number of stacks.

simulation model is not comprehensive enough to evaluate the performance of this topology compared to an active battery hybridization. Therefore, the weight of power converters are not included in the numerical optimizations to prevent discrimination of the FCS compared to the battery. This means that the numerical power balancing calculations, with varying FC/battery hybridization factors, are solely performed as an optimal power sharing between the power devices, neglecting the power conversion and any transient limitations of the system. Such conditions are mainly left for qualitative discussion.

3.7 Costs Calculation

The approach used to optimize the system mass and costs is presented in Chapter 5. The optimal hybridization and FC sizing will depend on many factors, such as the power device and mission profile characteristics, temperature limits and lifetime considerations. The latter is not accounted for in a mass optimization. Minimizing the mass of the power system is not effective if it completely deteriorates the expected lifetime of the power devices. To investigate how the investment costs of the power devices and the fuel costs are affected by the suggested sizing and operating conditions, the economic relation in Section 2.7 can be utilized. To include the cost of reinvestments as the power devices degrade, the lifetime must be estimated.

3.7.1 Lifetime Estimations

By dynamically calculating the FC stack voltage and the operating temperature, the FC lifetime model can be used to estimate the operating lifetime for different FC sizes. The temperature is calculated by assuming a cooling limitation given by the FC cooling system and the aircraft HEX. As the FC stack degrades, the required current to meet the load power of the mission profile will increase. This means that after some time the heat generation during takeoff and initial climb will exceed the cooling capabilities of the system, forcing the FC to operate at a higher temperature during the takeoff and the initial climb. For these calculations, standard temperatures (ISA) are assumed. For each flight, also the worst-case ambient temperature scenario[24] is calculated to see if the system is capable of keeping the FC temperature below a maximum of 95°C in the case of abnormal operating conditions. If not, the EoL criteria is assumed to be met. However, this is expected to occur with little deviation in time from the main EoL criterion of 10% power loss for the FCS.

The lifetime estimation approach is illustrated in Fig. 3.16.

[24] Worst-case is considered as a temperature of 40°C at ground-level.

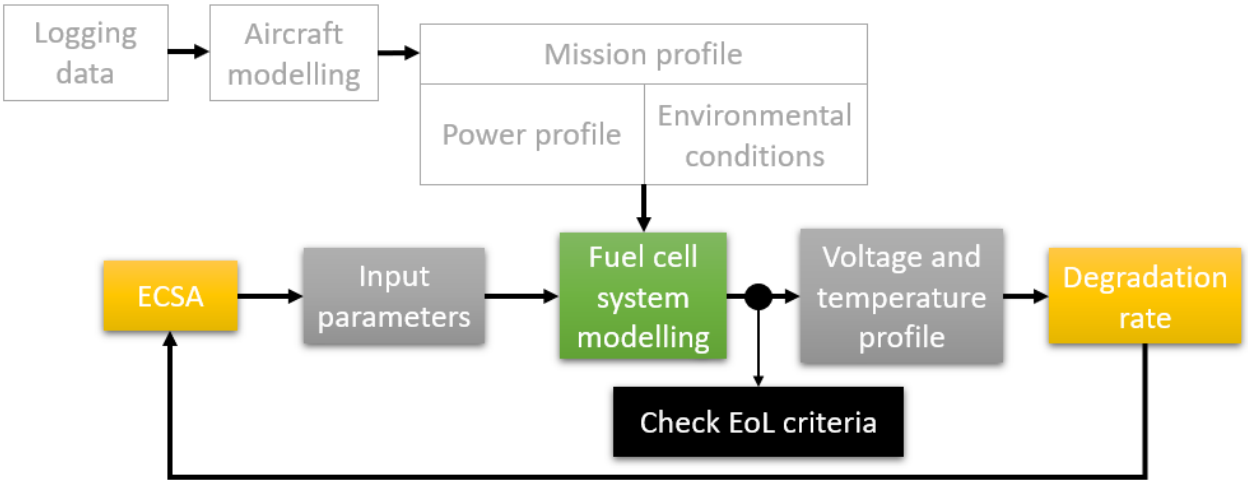

Figure 3.16: Schematic overview of FC lifetime estimation model.

The algorithm must iteratively simulate the flight mission until the one of the EoL criteria are met to find the operating FC lifetime. Updating the ECSA on-line throughout the simulation is found to be superfluous as the ECSA loss of each single flight is very small. To limit the computation time when used in larger optimization structures, the ECSA is only updated twice a week, or at every twenty-first flight in the case of six daily flights.

The aging model of the battery block in Simulink® can estimate the battery lifetime based on the charge and discharge currents and the depth-of-discharge (DoD). By obtaining the discharge profile for each hybridization case, the full cycles equivalent can be estimated by off-line simulations. However, since the battery in all relevant hybridization cases are operated at the maximum discharge current during takeoff and the initial climb, and with a DoD independent of the FC sizing, the preset cycle life model has not been utilized. Instead, a battery cycle life of 1000 cycles has been assumed as a basis for all relevant hybridization cases. This is estimated as the minimum cycle life at 10C and 100% DoD discharge by the manufacturer [98]. The constant cycle life assumption is justified by the small variation in how the battery is operated in the various optimization cases. A more accurate battery lifetime estimation is left for further works.

3.7.2 Model Parameters

The battery price is set to 5.14 $/cell based on the distributor pricing of the next generation of the reference cell [102]. The 2020 cell price split of 74.5% reported by BloombergNEF are used to estimate the cost of the whole battery pack [103]. This yields a battery cost of about 909 $/kWh. This is within the suggested cost range for $LiFePO_4$ batteries in Section 2.4, but still represent a conservative estimate when considering the battery price trend the last few years. The Pt dependent cost for automotive FCs, reported in [104], are used for price estimations of the FCS. These prices are based on historical data and the corresponding Pt loading. Thus, the price estimations of both power devices are slightly conservative and do not reflect the projected

cost developments for the coming years.

A discount rate of 4% and a time horizon of 15 years are used for investment cost calculations based on benchmark values from the European Commision [105]. It is expected that the reference flight performs six daily flights on average, similarly to what was found for comparable aircraft in [10]. By using these parameters in lifetime and present value calculations, the total investment costs can be estimated. This includes the initial investments, the reinvestments and the residual values of the power devices throughout the period of analysis.

Similarly, the fuel costs can be estimated from the fuel consumption of each flight. As for the power devices, there is uncertainty tied to the price development of hydrogen. Together with McKinsey & Company, the Hydrogen Council published a report in 2020 estimating the hydrogen at the pump price to be between 4-5 $/kg within 2030 for all evaluated distribution scenarios [106]. Even at 6 $/kg, hydrogen is estimated to be competitive for about 15% of the transport energy demand. In this work, 6 $/kg is used as the base hydrogen price. In addition, a sensitivity between 3-8 $/kg has been performed to illustrate the high sensitivity of this parameter.

3.7.3 Cost per Available Seat Kilometer

A typical measure for aviation costs is the cost per available seat kilometer (CASK). This measure expresses the average cost of operating the aircraft per available seat every kilometer. In this work, these costs are limited to the investment costs of the power devices and the fuel costs. Keep in mind that also other cost items should be considered in a complete cost-optimization. This can both be fixed costs and other operational costs, such as the maintenance costs and the cost of unavailability.

The payload capacity of the reference aircraft is 6124 kg [75]. According to Universal Hydrogen, their FC-powered projected version of the reference aircraft can achieve usable ranges of 400 nautical miles with compressed tanks and 40 passengers, yielding a passenger capacity of 4000 kg[25] [76]. Similarly, a passenger capacity of 4000 kg is assumed as the basis for the mass-optimized energy system in CASK calculations. In Section 7.4, it will be shown that this capacity might be a bit optimistic with the current technology of key electrical components. The CASK values will normalized to a reference case, limiting the importance of the payload capacity uncertainty. Figure 3.17 illustrates how the available payload capacity decreases for optimization cases with higher system masses than the mass-optimized case.

[25] Assuming 100 kg per PAX [75].

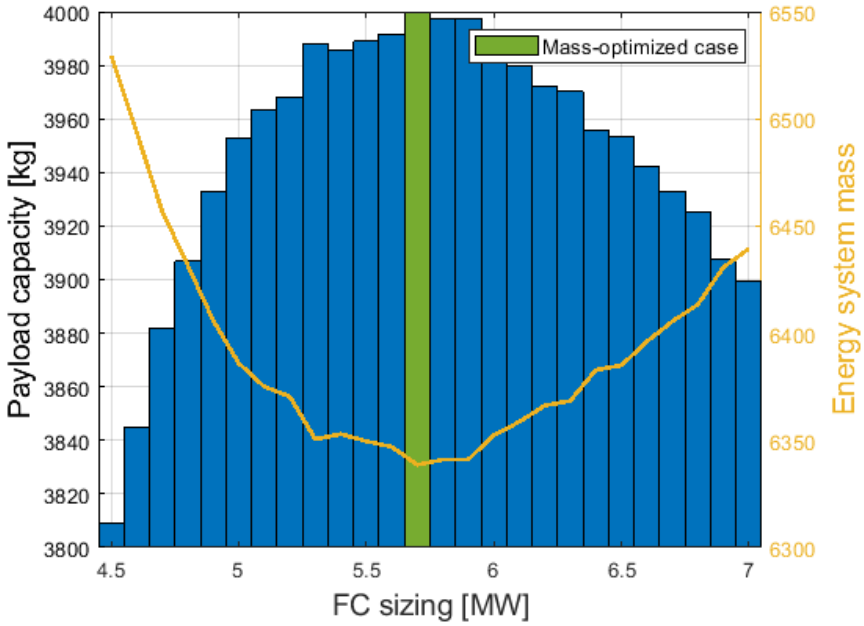

Figure 3.17: Available payload capacity based on the FC sizing and the corresponding energy system mass.

Everything else equal, a lower payload capacity results in a higher CASK. All costs are discounted with the same discount rate over the same time horizon. The economic calculations may give good indications on the cost-optimality, but the main value is found in the approach. The investment and fuel cost calculations performed in this work can also be useful in larger cost-optimizing model structures.

Chapter 4

Simulation Model

The mission profiles, the battery model, the FC model and the relevant submodels are realized numerically in MATLAB. These are used in the optimization work presented in the following chapter. The models are also implemented in Simulink to provide a more visual representation and easier control system implementations, such as power ramp limits for the FCS. The increased transparency following such a model easily allows users to investigate how the system responds to various inputs and operations. In this work, the model is primarily used to investigate the system behaviour during power steps and load loss. An overview of the simulation model topology is depicted in Fig. 4.1.

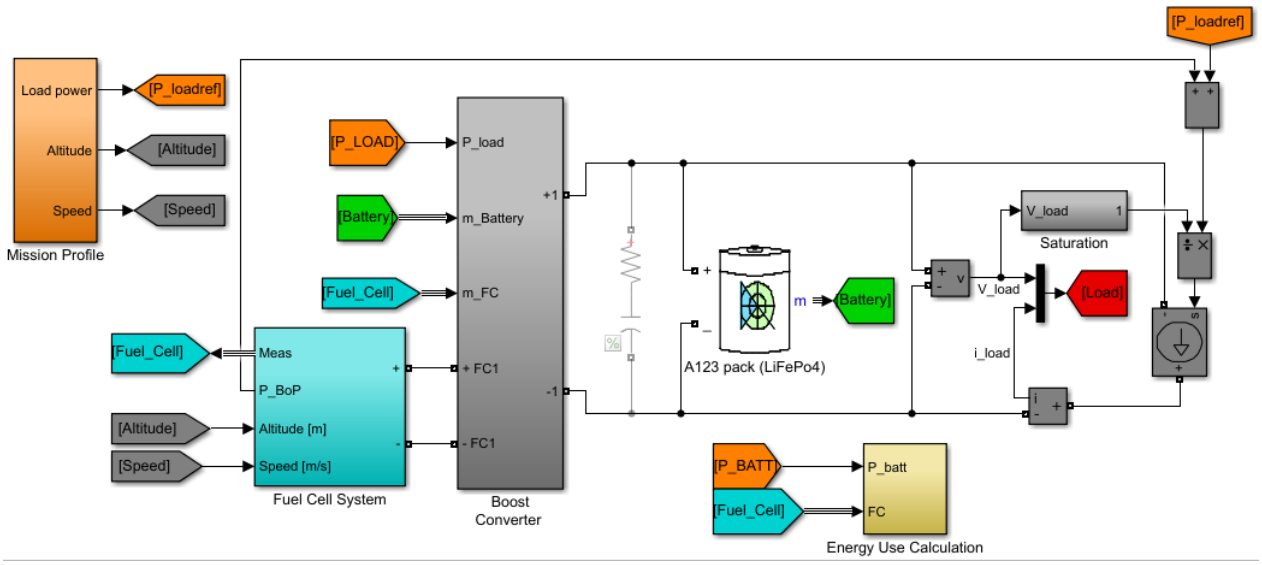

Figure 4.1: Overveiw of model implementation in Simulink®.

For the purpose of this work, the mission profiles are pre-calculated and simply applied to the system through a controlled current source. Thus, the required current supply from the power devices will depend on the DC-link voltage. With small adjustments, the load power could be calculated dynamically using the speed and climb rate logging data, at a computational cost.

For hybridization cases, the reference battery is directly shunted to the DC bus. This means that the DC-link voltage will be governed by the battery. The FC is connected through a boost converter, stepping the voltage up to an appropriate level.

Without any battery in the system, the FC must be responsible for the DC-link voltage. In this case, a cascaded controller with an inner current loop and an outer voltage loop must be used. The current controller must be included to match the supply and consumption of the reactants [107]. Only the hybrid version of the system is used for simulations in this work, to demonstrate how the power ramping and load loss can be simplified by including a battery in the energy system. More detailed descriptions on each subsystem can be found in Appendix C.1.

4.1 Power Ramp Case

The Federal Aviation Administration (FAA) have a power response requirement of increasing from 15%[1] to 95% of rated takeoff power in maximum five seconds [108]. From this, a power ramp case can be constructed on the FC stack level. For optimal FC sizing scenarios, the rated takeoff power of each stack is just below 100 kW, including the BoP power consumption. Thus, the FCS should be able to go from 15 kW to 95 kW within 5 seconds. By including the FCS's ramp-up limitation of 13 kW/s in the control system, the required battery power support and the corresponding DC-link voltage dip can be simulated for the hybrid system.

4.2 Load Loss Case

A worst-case transient scenario is that the power system suddenly loses the propulsive load while operating at full FC power. This can be caused by fault conditions or simply strong tail-winds easing off the load of the propellers. While the FCS is ramping down, the excess energy must somehow be consumed to prevent elevated DC-link voltages. This test case allows for simulations on how the battery can absorb some of this energy. The difference between the FCS power supply and the recommended battery charging limit is rejected in a braking resistor realized by a variable resistance.

4.3 Mission Profile Simulation

The simulation model is also well-suited to perform power balance simulations of the different mission profiles due to its high computational speed. In this work, the power balancing calculations used for optimizations are performed by numerical calculations in MATLAB®. Still, the simulation model are based on the same numerical equations and can, thus, produce similar

[1] Or the minimum flight idle power.

results in a more visual environment. Simple power balancing tests, with the optimized power devices, are performed in Section 8.2. The use of the numerical models in optimizations are described in the following chapter.

Chapter 5

Optimization Model

In this chapter, the optimization model used to find the best combination of FC and battery power, as well as the most convenient FC sizing, are presented. The model will be used to calculate the energy system mass in Chapter 6 and investment and fuel costs in Chapter 7. First, an initial optimization approach is presented as it describes the key principles of the FC optimization in an illustrative manner.

5.1 Optimization Model Development

Prior to the introduction of battery power support, the main components of the optimization are the FC, the corresponding BoP components and the hydrogen tank. Also the HEX[1] are included for mass calculations. In [7], a simple objective function is presented to demonstrate the trade-off between FC power and FC efficiency,

$$f(i_{0,N}) = k \cdot P_{fcs}(i_{0,N}) + (1-k) \cdot \eta_{fcs}(i_{0,N}) \tag{5.1}$$

where k is a weighting factor. The authors are only considering the electric efficiency of the FC stack. In this work, η_{fcs} represents the efficiency of the whole FCS and P_{fcs} represents the net output power. Figure 5.1 shows how the optimal current density $i_{0,N}$, and the corresponding objective function value, varies with different weightings, k.

[1] Presented in Section 3.2.3

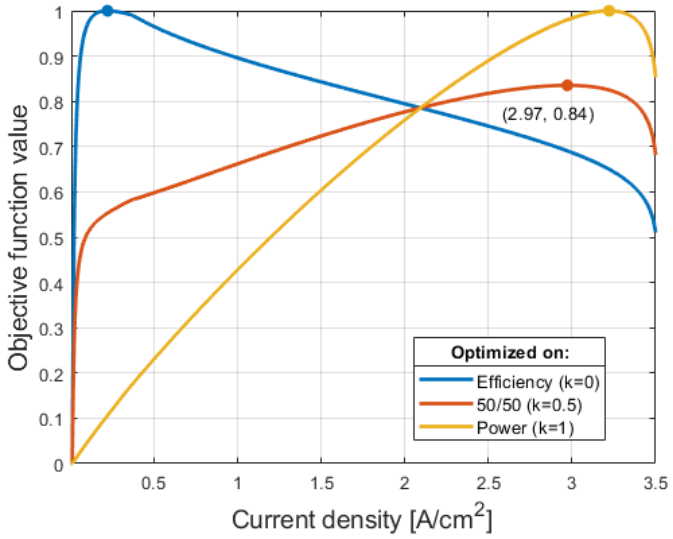

Figure 5.1: Finding the optimal current density for different weightings between power and efficiency.

The power output is optimized at a high current density, while the peak efficiency is found at a low current density. In this case, the optimal trade-off between power and efficiency is found at a current density $i_0 = 2.97$ A/cm2 for a 50/50 weighting. At this point, the FC net output is 290.4 W/cell[2,3]. The maximum net output of 296.3 W/cell is acheived at 3.27 A/cm^2. If $i_{0,N} = 2.97$ A/cm^2 is used as the dimensioning current density, this yields a theoretical oversizing of about 2%[4]. In practice, as the cell area is assumed constant, it means putting together enough cells to meet a particular power requirement at the dimensioning current density. If the MPP current density is dimensioning, about 13 500 cells would be required to achieve a net output of 4 MW from the FCS. This is equivalent to almost 30 units of the reference stack. Similarly, 13 775 cells would be required if 4 MW was to be met at a current density of 2.97 A/cm^2. Whether the FCs should be sized based on the cell count or the cell area will depend on the characteristics of the problem. Ideally, both are optimized to achieve both desirable voltage and current levels. In this work, the cell area is defined by the reference stack such that the optimal cell count is implicitly the target of the optimization. Thus, a FC oversizing can be seen as an increased cell count realized by an increased number of paralleled reference stacks.

5.1.1 Mass Optimization

When optimizing the FCS for an aircraft, the total mass is essential. Both the fuel tank and the cooling system will be sensitive to the efficiency of the FCS. By expressing each system component as a function of the current density, the optimal current density working point can be

[2] Net power output calculated for reference FCS and divided on number of cells $N_{cells} = 455$.
[3] At beginning-of-life.
[4] $296.3W/290.4W - 1 = 2.03\%$.

obtained. The weight of the FCS can be approximated by estimating the weight of the FC stack, the compression system, the cooling system, the tank and the fuel,

$$\begin{aligned} m_{tot}(i_{0,N}) &= m_{fc} + m_{comp} + m_{cool} + m_{tank} + m_{H_2} \\ &= \frac{P_{rq}}{\rho_{fc}} \cdot \frac{P_{cell,max}}{P_{cell}(i_{0,N})} + \frac{P_{rq}}{P_{cell}(i_{0,N})} \cdot \frac{P_{cell,comp}(i_{0,N})}{\rho_{comp}} + \frac{P_{rq}}{\rho_{cool}} \cdot \frac{V_{LHV} - V_{cell}(i_N)}{V_{cell}(P_{max})} \\ &+ m_{tank}(E_{rq}, \eta_{fcs}(i_N)) + \frac{E_{rq}}{\omega_{H_2} \cdot \eta_{fcs}(i_{0,N})} \end{aligned} \tag{5.2}$$

where

$$m_{tank}(E_{rq}, \eta_{fcs}(i_N)) = \begin{cases} \varrho_{tank} \cdot \pi^{\frac{1}{3}} \left(\dfrac{6 \cdot E_{rq}}{\rho_{H_2} \cdot \omega_{H_2} \cdot \eta_{fcs}(i_N)} \right)^{\frac{2}{3}} & \text{(Spherical tank)}, \\ \varrho_{tank} \cdot \pi^{\frac{1}{3}} \left(\dfrac{3\sqrt{6} \cdot E_{rq}}{\rho_{H_2} \cdot \omega_{H_2} \cdot \eta_{fcs}(i_N)} \right)^{\frac{2}{3}} & \text{(Cylindrical tank)}, \end{cases}$$

The tank mass is derived from (2.12)-(2.14), where all relevant parameters are explained. P_{rq} and E_{rq} represent the estimated FC power and energy requirement of the flight, respectively, while η_{fcs} represents the operating efficiency of the whole FCS. A high dimensioning current density, i_N, is equal to little oversizing of the FC, while a low i_N brings the opposite. This means that the weight of the FC stack will increase for a lower i_N, while the tank, fuel and cooling system weight will decrease due to the improved efficiency of an oversized FC. The compression system will also benefit from an oversized FC due to the nonlinear relation between the power output and the compressor requirement. Smaller BoP components, such as the hydrogen circulating pump and the humidifier, are neglected in the FCS sizing. In comparison, the hydrogen pump of the Toyota Mirai has a maximum power output of only 2% of the air compressor and the FCS is designed without a dedicated humidifier [95]. The HEX between the liquid cooling loop of the FC and the ambient air is included due to its importance for the aircraft weight, even though it is not normally regarded as a part of the FCS.

5.1.2 Hybridization

A fraction, $1 - h$, of the power requirement can be assigned to other power devices to share the load. As batteries are devices with both reasonable power densities and energy densities, and are already used as energy buffers in hydrogen aircraft, this technology is used as the basis for hybridization calculations. With the hybridization factor, (5.3) is achieved.

$$m_{tot} = h \cdot m_{fcs} + m_{tank} + m_{H_2} + (1 - h) m_{bat} \tag{5.3}$$

Unlike FCSs, where the energy is related to the hydrogen tank and the power to the FC, batteries must be sized to ensure both enough power and energy. This means that either the energy or

the power requirement may be dimensioning, as in (5.4).

$$m_{bat} = max\left(\frac{P_{bat}}{\rho_{bat}}, \frac{E_{bat}}{\varepsilon_{bat}}\right) \tag{5.4}$$

Here, ρ_{bat} and ε_{bat} represent the battery power density and energy density, respectively. For most scenarios, batteries are not competitive with hydrogen and FCs on energy. Thus, for the application of power boosting during the initial flight phases, the power requirement will be limiting. Figure 5.2 illustrates the required battery power and energy for the four different mission profiles, given a hybridization factor of 0.625 (i.e. a FC power limit of 2.50 MW).

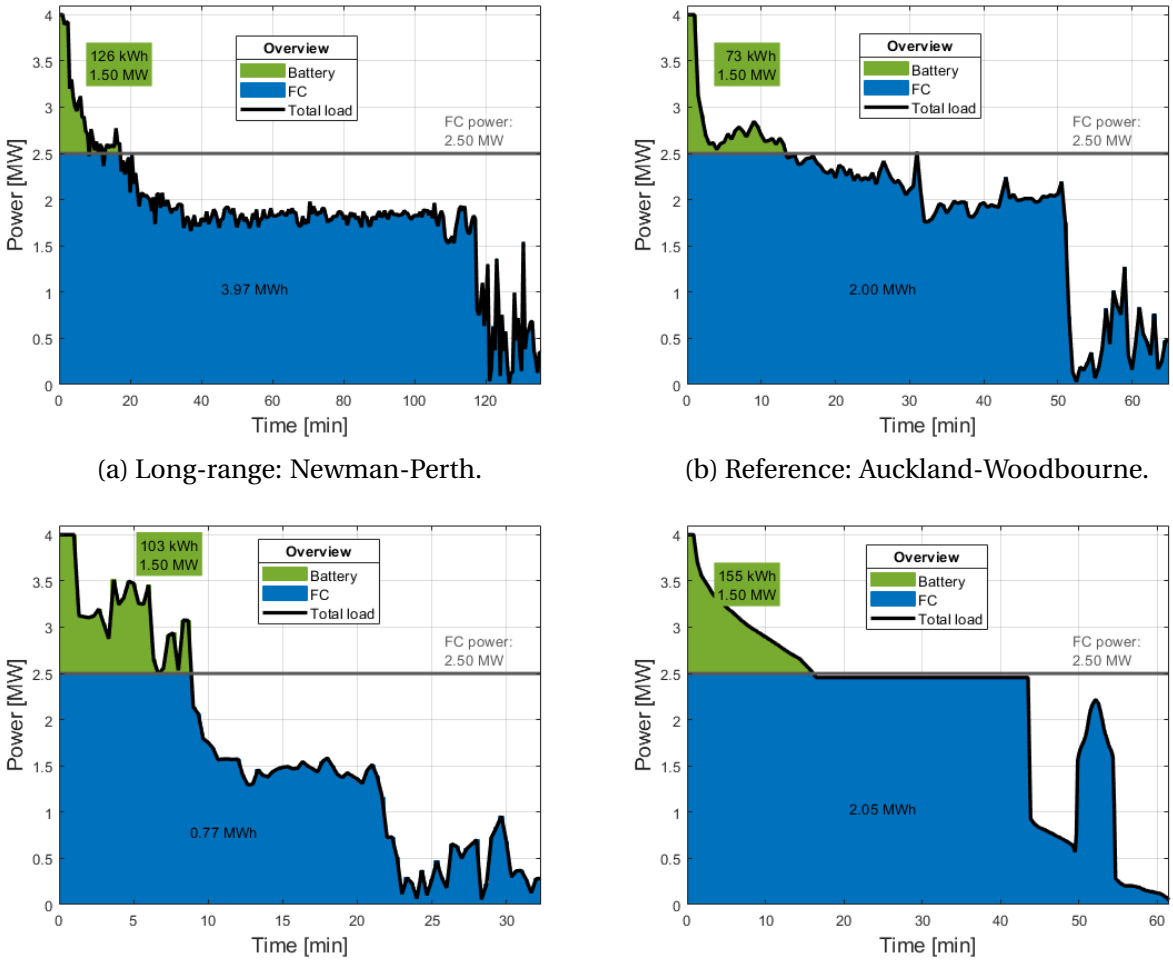

(a) Long-range: Newman-Perth.

(b) Reference: Auckland-Woodbourne.

(c) Short-range: Bodø-Evenes.

(d) Standard profile: Based on [10].

Figure 5.2: Power profiles based on logging data from four different flights.

Both for long, medium and short ranges, the battery power requirement heavily outweighs the corresponding energy requirement. In the case of conservative C-rate limits, the battery would need to be seriously oversized in terms of energy capacity to meet the peak power requirement. A mass optimization with typical continuous C-rates and linear power and energy densities will

rarely find any optimality in including a battery. More advanced approaches are required to perform more in-depth optimizations.

5.2 Optimization Approach

The optimization approach will be a trade-off between generality, complexity and accuracy. One approach with a low computational cost is to assume constant operating conditions to obtain dimensioning power and energy requirements.

- **Fixed power requirement:** With this approach, the optimization is based on a fixed power and energy requirement. The energy requirement can be accurately calculated based on a specific mission profile. However, the operating efficiency of the power devices will be estimated based on the fixed power requirement. This will lead to significant inaccuracies as the real power profile is varying with time. A typical choice for the fixed power requirement is the maximum load power. Using this may lead to an unnecessarily large oversizing, as the aircraft is operated at the maximum power only for a limited fraction of the flight. This approach will be more accurate when the takeoff and climb make up a large part of the flight. Another possibility is to use the cruise power as the dimensioning power requirement. This choice will optimize the power devices for the, usually, longest flight phase, but will not assure that the peak power requirement is met. The choice will be particularly useful for flights with long cruise phases and in the case where batteries or other boosting devices are sized to cover the extra power during takeoff and climb. The fixed power requirement approach has minimal computational cost, is useful for preliminary optimizations and can take part in larger modelling structures. It can also be used to calculate an initial guess or starting point in more demanding, iterative algorithms, such as below.

- **Mission profile:** This approach includes optimizing the power devices based on a specific mission profile. Despite more computational complexity, this will give more accurate results and can be applicable for different types of specific flight missions. Another advantage is that the power requirement can be evaluated dynamically. In the case of battery hybridization, the battery power and capacity can be estimated based on the discharge profile for each hybridization case. Similarly, the FCS efficiency and hydrogen consumption can be estimated depending on the power output and the environmental conditions throughout the flight, such that an optimal FC size can be found for each hybridization case.

Both approaches will be further elaborated and demonstrated in the following sections.

5.2.1 Optimization On Constant Power

This initial approach is briefly presented as it is illustrative. Figure 5.3 shows the optimized mass when the FC stack is modelled at BoL with compressed hydrogen storage in cylindrical (cylind.) tanks.

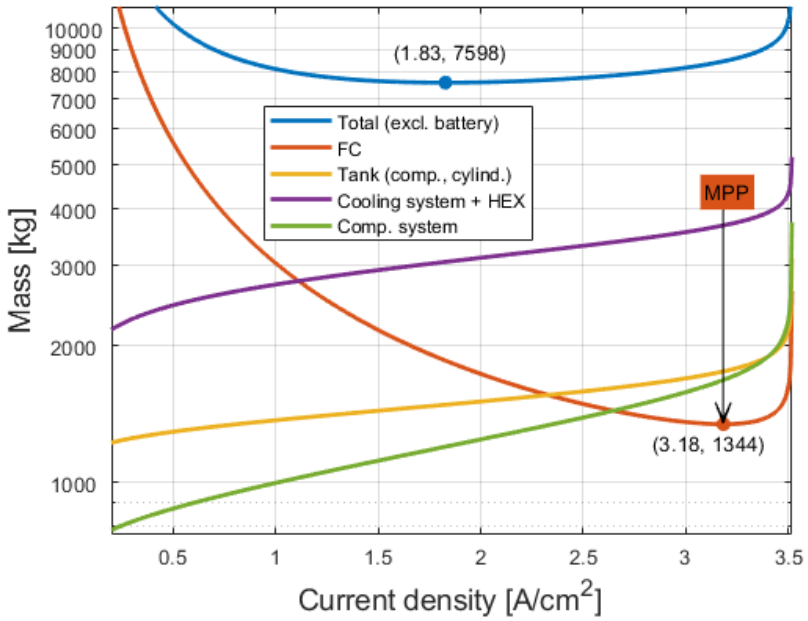

Figure 5.3: Optimization with a constant power requirement. The mass-optimized dimensioning current density is significantly lower than the MPP. Comp. system = compression system.

In this case, the optimal weight is achieved when the FC stack is sized to meet the maximum power load at i_N = 1.83 A/cm^2. This equals to a 38% oversizing, or a 5.52 MW FC at BoL, to meet the 4.0 MW power requirement. This means that enough cells and stacks are put together such that the maximum power requirement are met at a more desirable operating point than the MPP. The advantage of this oversizing is found in the lowered cooling, fuel and compression requirements at lower current densities. The aircraft will operate at different altitudes. The constant power approach is not well-suited to evaluate the consequence of operating under varying environmental conditions for the different flight phases. These limitations are also found in similar existing optimization work. If batteries or other boosting devices are assumed to cover parts of the extra power required during takeoff and climb, the FCS can be designed to meet a more continuous power profile. Figure 5.4 shows a scenario where only 2.55 MW (61.25%) of the load power is to be covered by the FC. In this case, the dimensioning power will be closer to the average FC power throughout the whole flight and, thus, give a more accurate estimation of the actual fuel consumption.

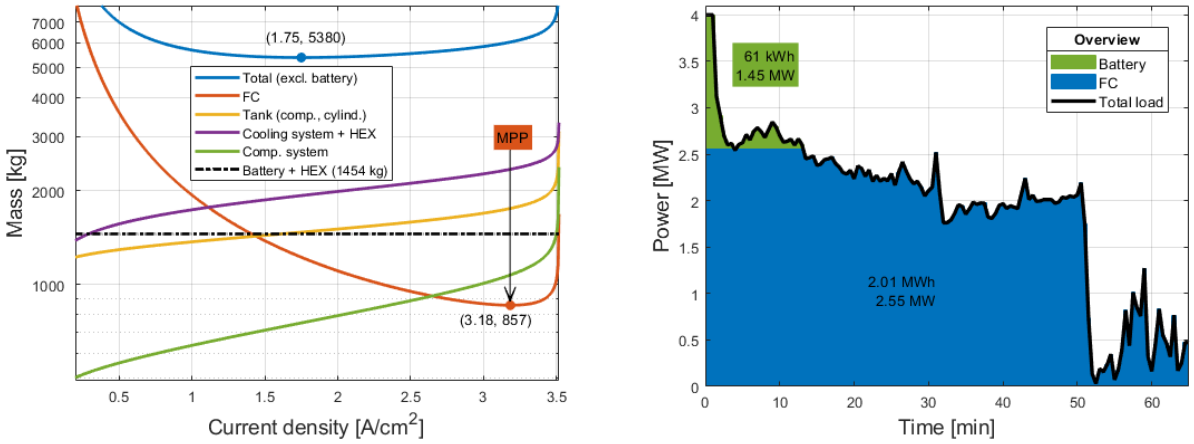

(a) Operating point optimizing system mass.

(b) Battery buffer to cover 1.45 MW.

Figure 5.4: Optimization with a constant power requirement for FC/battery hybrid

The optimal oversizing is now 42.5% to supply the 2.55 MW power share, with the remaining load power being covered by the reference battery. The constant power approach cannot be used to find the optimal hybridization weight alone[5], as this will depend on the characteristics of the mission profile. To obtain the battery weight, and the corresponding HEX requirement due to battery heat generation, the battery load depicted in Fig. 5.4b should be used to find the required battery capacity. As the battery is assumed to be unaffected by the changing environmental conditions during the flight, this suboptimization does not bring too much computational cost.

Despite its inaccuracy, this optimization method can give decent estimations and can be run for several different scenarios without computational challenges. The results obtained with this approach can be found in Appendix D.1. However, the optimization approach was found to be too inaccurate. Inspired by its limitations, the main optimization model has been developed utilizing the specific mission profiles.

5.2.2 Optimization On Mission Profile

To ensure a higher accuracy in the mass estimations, the power requirement of all relevant devices, and the corresponding fuel consumption, can be estimated dynamically throughout the flight mission. The method also allows for evaluating operation with dynamically changing FC conditions[6]. In this work, the FC is constantly kept at reference conditions where the model has good compliance with the polarization curve of the reference stack. Even though the operating conditions of the FC are assumed constant, the power consumption from the BoP components will vary significantly with the environmental conditions. Particularly, the required compres-

[5]The bulk energy requirement of the ES device must be known to estimate its weight contribution.

[6]The FC model allows for varying operating temperature and pressure levels.

sor power will increase dramatically at high altitudes to keep the operating pressure constant. By using discrete time steps, the algorithm can iterate through a given mission profile and calculate the current, voltage and power profiles of the FC and the battery in the case of hybrid operation. All possible hybridization cases can be run with different levels of FC oversizing to find the optimal combination. Unless otherwise specified, time steps of 1 second are used to limit the computation time. For illustration, the FC and battery profiles for a 60% hybridization case with a 40% oversized FC is shown in Fig. 5.5.

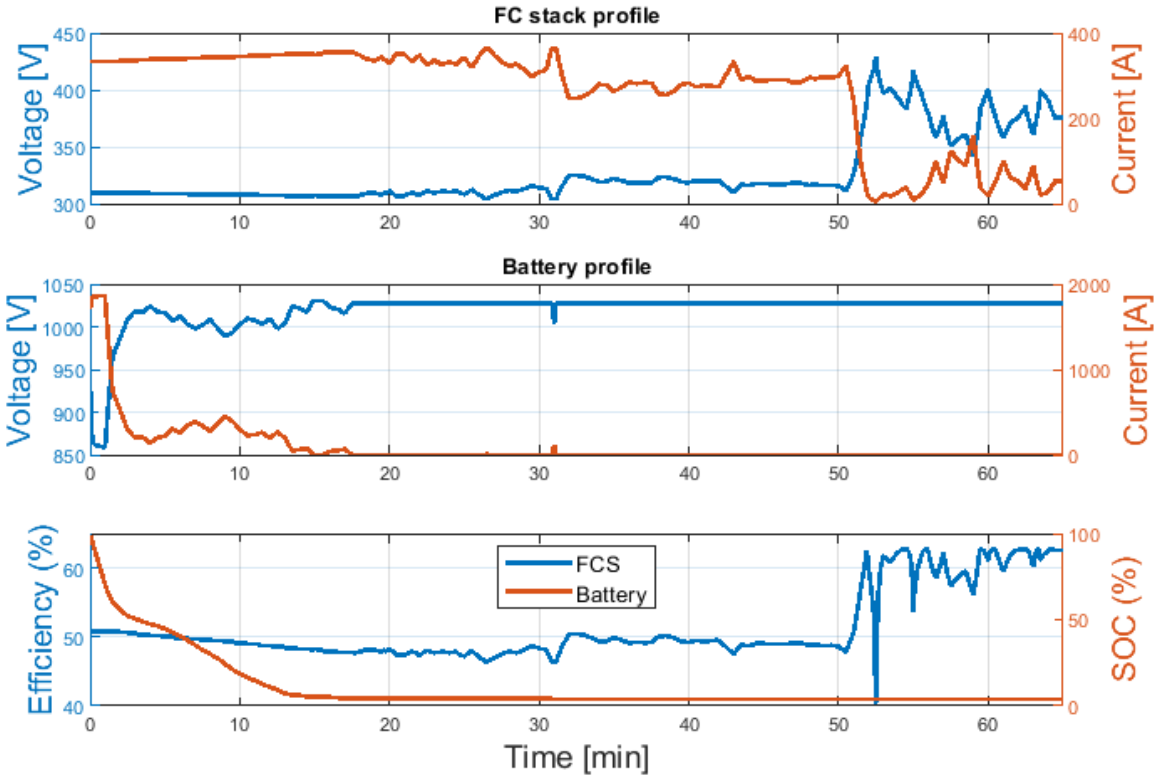

Figure 5.5: Discharge profiles for the power devices throughout the flight with a hybridization factor of 0.6 and a 40% FC oversizing.

Just enough battery cells are put together in series and parallel to ensure compliance with cell current, cut-off voltage and SOC limits for the given power share. No recharging of the battery from the FC is considered for this optimization method. In the case of higher battery power shares, where the battery is expected to pick up load after the initial flight phases, battery recharging should be implemented in the algorithm. Due to the shape of the flight missions, with decreasing load power after the takeoff and climb, the simplification will be negligible for the optimization of the relevant hybridization cases.

A schematic overview of the optimization procedure[7] is shown in Fig. 5.6.

[7] Code scripts for the mission profile, FC and battery modelling can be found in Appendix F.

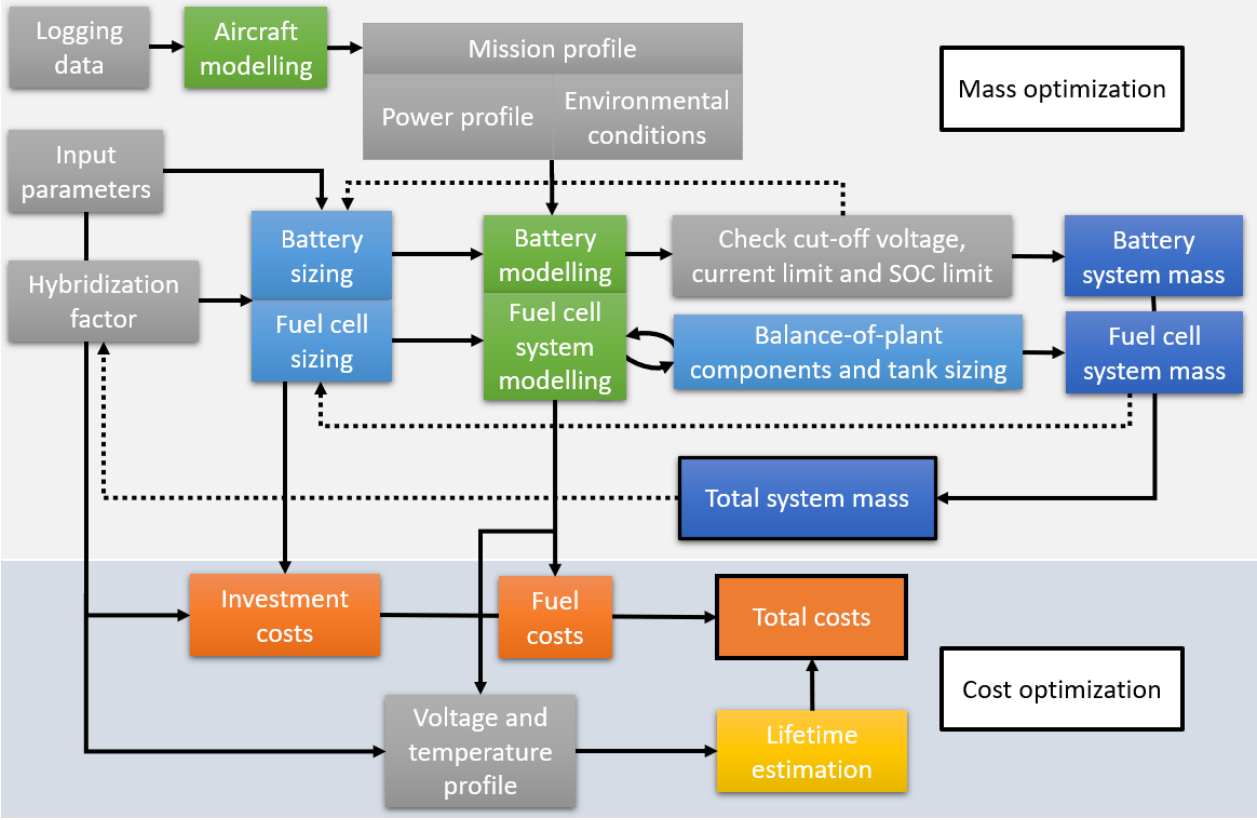

Figure 5.6: Schematic overview of the mass- and cost-optimizations.

By utilizing all the submodels, parameters and assumptions presented in Chapter 3, mass and cost optimizations can be performed dynamically. By iteratively calculating the total mass of the energy system[8] for different FC and battery sizings, the optimal combination can be obtained.

For each given hybridization case, the corresponding investment costs and fuel costs can be estimated based on the power device sizes and the fuel consumption. Another advantage of the approach is that the obtained voltage and current profiles for the power devices can be used for lifetime estimations. The dynamic temperature development of the FC stack is also valuable in this context. Lifetime estimations are performed by the approach presented in 3.7.1.

[8]Mass calculations consider the FC stack, the compression system, the cooling system and HEXs, the hydrogen storage and the battery. Power densities and dimensioning criteria for the relevant components are presented in Chapter 3.

Chapter 6

Mass Optimization

6.1 Optimization On Mission Profile

The optimization differentiates between two main cases:

- *FC only case*: The FC operates without support from batteries or other energy buffers.
- *Hybrid case*: The FC is hybridized with a battery to supply the propulsion load.

6.1.1 FC Only Case

A range of FC sizes[1] has been evaluated to find the mass-optimized FC sizing. The optimal FC sizing is defined as the point where the combined mass of the FCS, fuel, tank, battery and HEX is at a minimum. The key results from this optimization in summarized in Fig. 6.1.

[1] The algorithm iterates through the defined FC range with discrete steps of approximately 64 kW (275 cells) to find the optimal size.

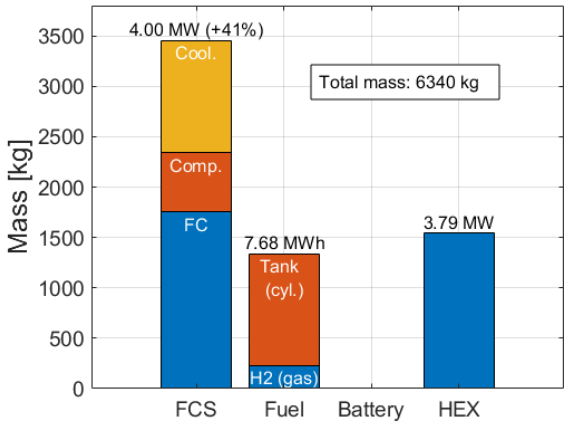

(a) **Compressed storage:** Component mass specification.

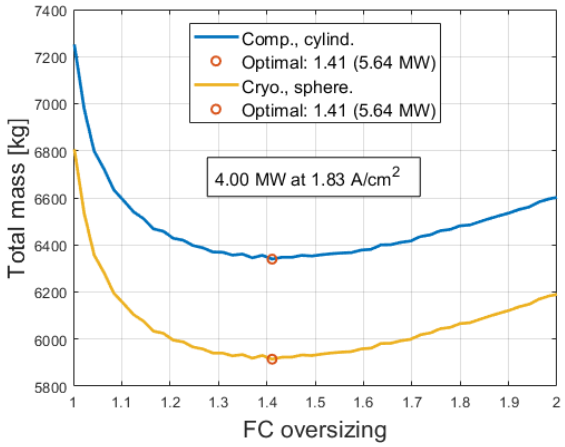

(b) FC size sensitivity.

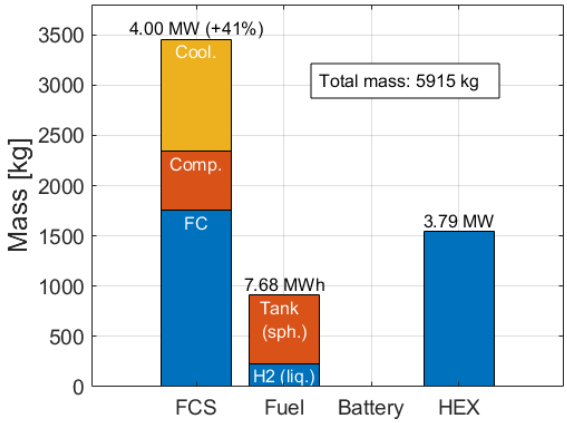

(c) **Cryogenic storage:** Component mass specification.

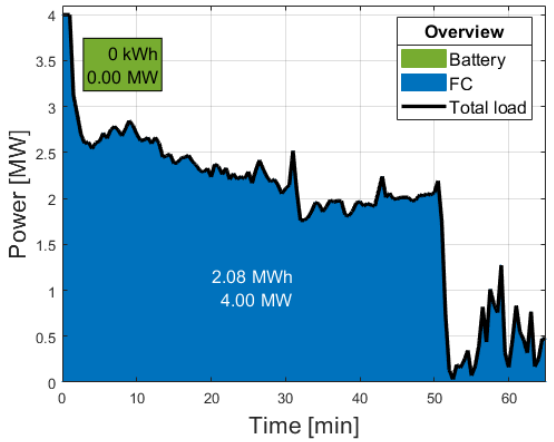

(d) Power sharing.

Figure 6.1: Optimized FC sizing for reference mission profile.

- Figure 6.1a: With compressed storage the mass-optimized FC sizing is estimated to be a **41%** oversizing. This gives a maximum power output of **5.64 MW** if operated at the MPP. However, the compressor and the cooling system are dimensioned for the nominal power point, not the MPP. The mass of the energy system components is estimated to **6340 kg** for this case.

- Figure 6.1b: Without any FC oversizing, the total mass increases dramatically due to the high fuel consumption and cooling requirement. The weight-reducing effect of oversizing decreases at large oversizing factors, or low current densities, due to the nonlinear power and efficiency curves of the FCS. It is essential that the FC is at least large enough to avoid continuous operation beyond the ohmic region of the polarization curve, in the

mass transport region[2]. The same oversizing is found optimal both with compressed and cryogenic tanks. The optimal dimensioning current density is **1.83 A/cm**^{2}.

- Figure 6.1c: With cryogenic storage the total mass is **5915 kg**, yielding a **6.7%** reduction from compressed storage. The weight of the tank is less prominent in this case. This is due to the reduced hydrogen volume and, thus, tank surface area. Also here, a **41%** FC oversizing is found optimal.

- Figure 6.1d: The FC energy requirement is **2.08 MWh**. Due to the FCS efficiency and the fuel margin requirement, this makes up only **27.1%** of the hydrogen energy stored in the fuel tanks.

Similar result plots can be found for the remaining mission profiles in Appendix D.2.1.

6.1.2 Hybrid Case

A range of FC sizes and hybridization factors have been evaluated to find the mass-optimized hybridization and FC oversizing. The key results are summarized in Fig. 6.2.

[2]This can be understood by the power and efficiency curves in Fig. 3.11b in Section 3.2.4.

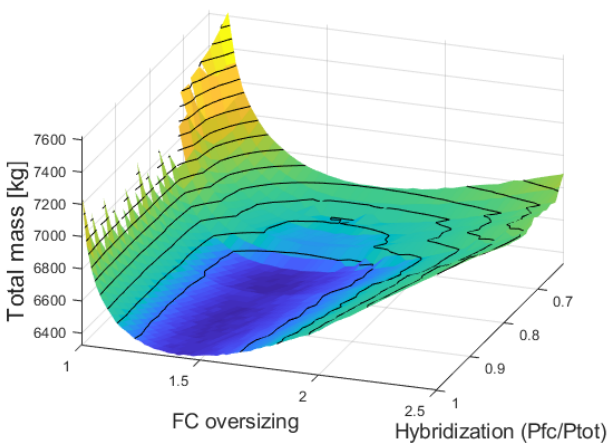

(a) Mass profile.

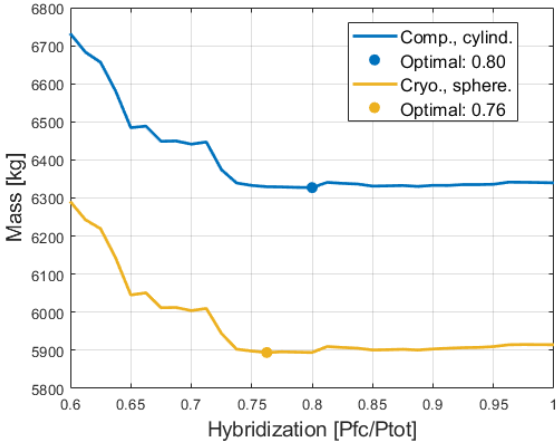

(b) Optimal hybridization.

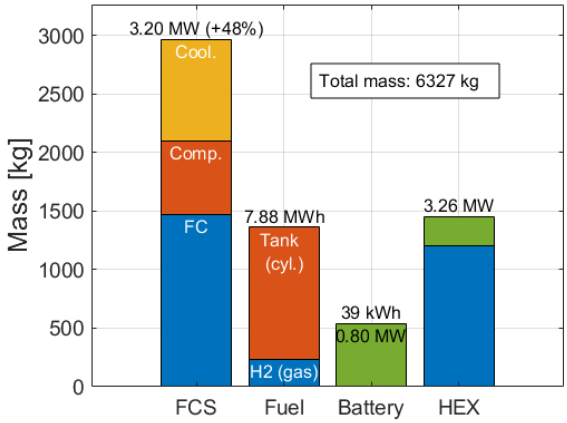

(c) Optimal mass specifications.

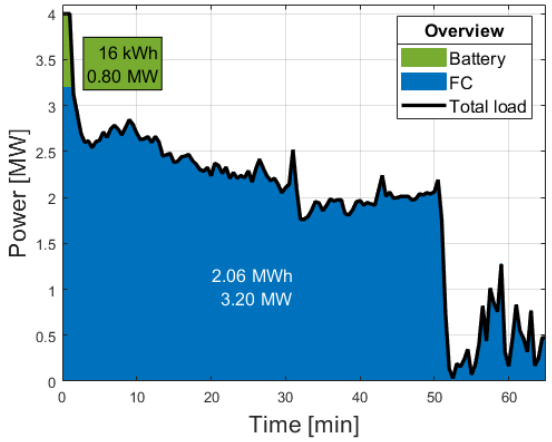

(d) Optimal power sharing.

Figure 6.2: Reference mission profile: Auckland-Woodbourne. Compressed storage in cylindrical tanks.

- Figure 6.2a: There is a hybridization range between **0.74** and **1.0** giving relatively similar mass estimations. The total mass increases rapidly for hybridization factors below this, due to the low energy density of the battery. In all cases, a significant oversizing of the FC, between **40%-60%**, is optimal with respect to the total mass.

- Figure 6.2b: The optimal mass is achieved at a hybridization factor of **0.80** and **0.76** with compressed and cryogenic tanks, respectively. The optimal FC oversizing is **48%** in both cases, yielding a maximum power output of **4.74 MW** if operated at the MPP. The oversizing is higher than for the *FC only case*, where the FC is already significantly oversized with respect to the cruise phase power. The oversizing means that the FC stack itself should be capable of supplying the whole peak load during takeoff if operated beyond its rated

power point[3]. However, this would bring higher requirements from the FC cooling system, the aircraft HEX and the compressor.

- Figure 6.2c: Despite a high battery power rating, the corresponding HEX requirement (colored in green) is relatively low due to the high battery efficiency. The energy rating of the battery is higher than required in order to meet the power requirement without violating its discharge limits. The total mass is **6327 kg**, which is only a **0.2%** reduction from the *FC only case*. With cryogenic tanks, the total mass is **5894 kg**[4] for the *hybrid case*, yielding a **6.8%** reduction from compressed storage.

- Figure 6.2d: In the optimal mass case, the bulk energy is supplied by the FC and hydrogen. The FC energy requirement is **2.06 MWh**, but due to the fuel margin requirement and the FCS efficiency this makes up only **26%** of the stored hydrogen energy. The battery contributes with **0.80 MW** during takeoff and initial climb. Still, only **16 kWh** of the required **2.08 MWh** are covered by the battery.

Similar result plots can be found for the remaining mission profiles in Appendix D.2.2.

6.2 Device Characteristics

In all cases, the total mass reduction from including batteries for power support is almost negligible with the given reference devices. However, the optimization is sensitive to the performance of the battery. In Fig. 6.3, the energy density of the reference battery is varied within a reasonable range to evaluate its influence. The adjustment is performed by changing the cell mass, such that also the power density will increase correspondingly.

[3] Rated power point at current density 1.73 A/cm^2.
[4] Not shown in plot.

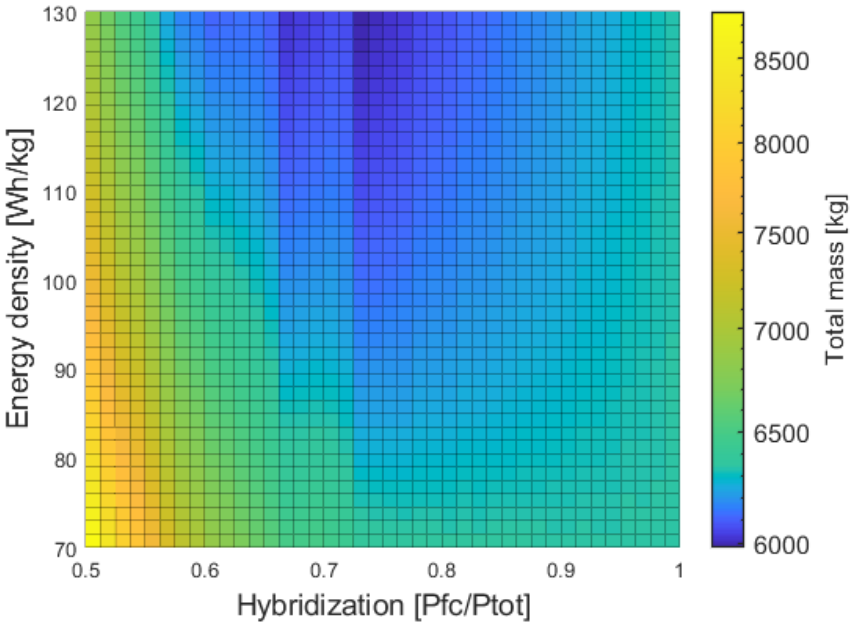

Figure 6.3: Hybridization mass with a sensitivity range on the battery energy density.

At 130 Wh/kg, the optimal hybridization factor is **0.725**, yielding a **5.7%** weight reduction from the *FC only case*. The corresponding battery power density is **2.4 kW/kg** at this point. The plot illustrates how sensitive the optimal hybridization will be to the development of the power device technologies. Still, even at quite high energy densities, the mass-optimization limits the role of the battery to power boosting rather than bulk energy supply. It is important to clarify that batteries with higher energy densities than the reference battery already exists commercially. However, the required discharge rates are less compatible with typical high energy batteries. Due to the high power to energy ratio, there are reasons to believe that also supercapacitors may be applicable for electric aircraft boosting power.

To demonstrate the *effective* power and energy densities of the power devices, with their complementary components, relevant calculations[5] are performed based on the optimal *hybrid case*, specifically. The results are shown in Fig. 6.4.

[5]The power densities are calculated based on the maximum continuous power output of the power devices. The energy density of the hydrogen and tank represents the actual energy delivered by the FCS, by adjusting for the varying FCS efficiency throughout the flight.

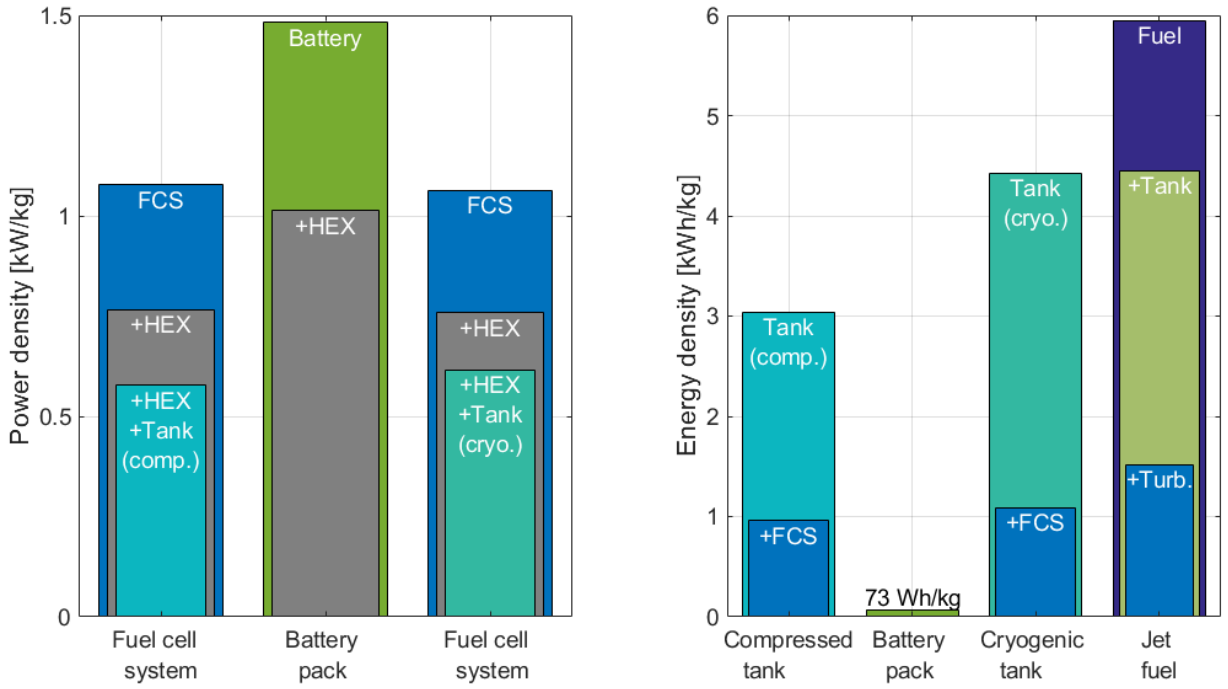

Figure 6.4: Device characteristics for the reference mission profile. Energy densities are based on actual energy output from the fuel cell system or jet turbine. An optimistic jet turbine efficiency of 50% is used for the jet fuel calculation.

The power density of the battery is **1.48 kW/kg**, while it is **1.08 kW/kg**[6] for the FCS. The optimal FCS is significantly oversized to limit the aircraft HEX requirement. The power density of the FC *stack* would be higher without this oversizing. However, the combined FCS, HEX and tank system would be heavier, yielding a overall inferior power-to-weight ratio. Contrarily, the little need of battery oversizing is an important reason why the battery power density is so high. The high operating efficiency of the battery limits the total heat generation during the takeoff and the initial climb, restricting the total HEX requirement. Thus, the battery can be relatively compact, without compromising on the requirements of its surrounding components. This consideration is often neglected in similar optimization work, even though the peripheral components, and the aircraft cooling system in particular, represent key challenges to overcome for FC-powered aviation.

The densities are represented with an increasing component penetration to illustrate how key components are affecting the system densities. For the energy density, it is noticeable that the hydrogen system is slightly inferior to the conventional fuel system[7], but far superior to the reference battery. Even with compressed tanks, the energy density is significantly higher

[6] This do not include the weight of the FC control system, the small hydrogen pump or power electronic converters.

[7] Energy densities of conventional fuel system based on values in [21].

than for the HY4 project[8]. This may partly be explained by a lower area-specific tank mass, but the improvement can mainly be found in a higher energy requirement, giving larger tanks with better volume to area ratios. Thus, for larger aircraft and longer flights, the weight efficiency of the tank can be further improved and even surpass the energy density of conventional fuel systems [7]. However, this may require aircraft design changes due to voluminous tanks.

[8] Discussed in Section 2.3.10.

Chapter 7

Cost Optimization

7.1 Lifetime and Investment Costs

See Section 3.7 for the choices of parameters relevant for the lifetime and economic calculations. For all calculations in this section, it is assumed that the aircraft is operated at its maximum takeoff weight for all scenarios. Thus, for increasing energy system weight, the available aircraft payload will decrease. The cost optimization is performed with discrete steps of 100 kW on the FC size.

7.1.1 Investment Costs

Figure 7.1 shows the investment cost of the power devices, the total system mass[1] and the estimated FC lifetime for the *FC only case*.

[1] Including the FCS, fuel and tank, battery (if any) and HEXs, as in Section 6.1.

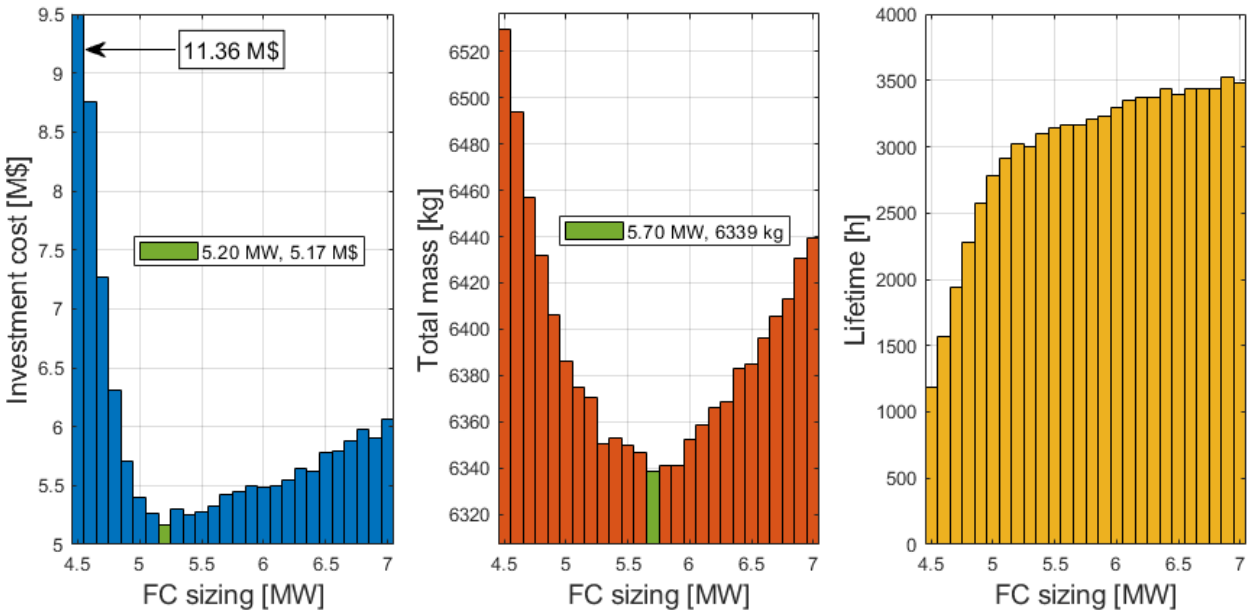

Figure 7.1: Power devices investment cost, the energy system mass and the fuel cell (FC) lifetime estimation for the *FC only case*.

The lowest investment costs are achieved with a **5.20 MW**, or **30%** oversized, FC. This is less oversizing than the mass-optimized size of **5.70 MW**[2]. The estimated lifetime increases with increasing FC sizes and decreases the number of required FC reinvestments throughout the period of analysis. Thus, the lowest total investment costs are found at the optimal trade-off between the initial investment cost and the total number of reinvestments. Similar results are shown with the mass-optimized hybridization factor[3] in Fig. 7.2.

[2]Notice that this value is slightly changed from 5.64 MW in the previous chapter because of the lower resolution on the iterative steps in this chapter.

[3]Hybridization factor = 0.8.

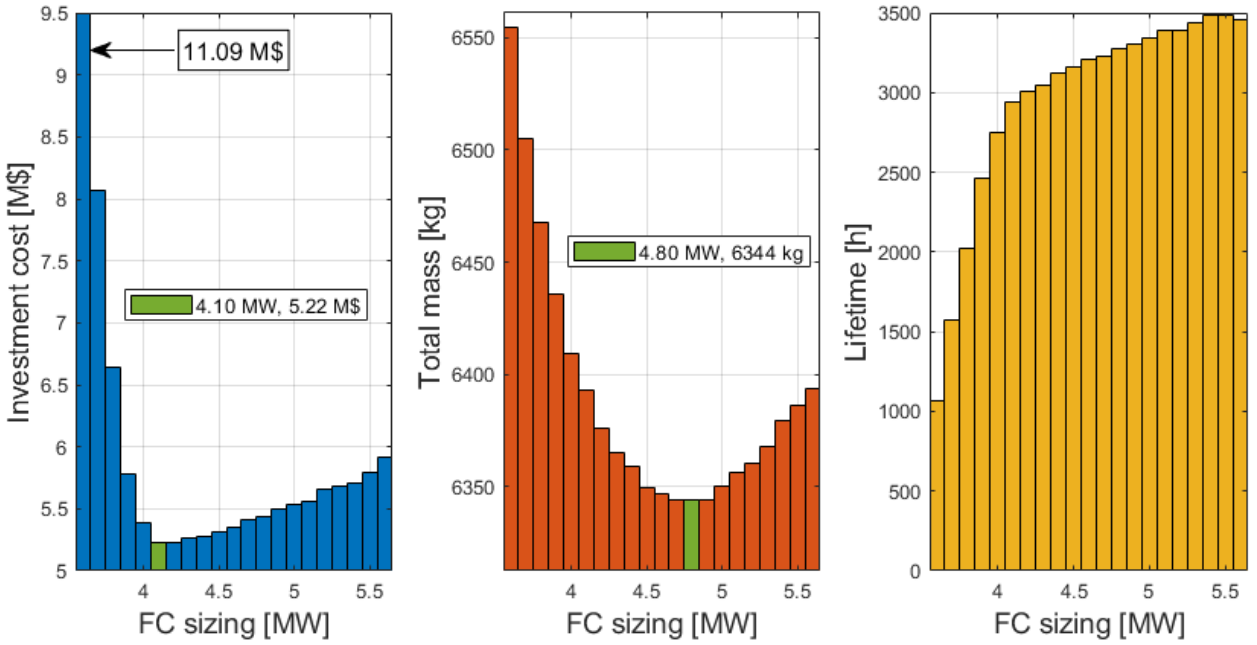

Figure 7.2: Power devices investment cost, the energy system mass and the fuel cell (FC) lifetime estimation for the FC/battery *hybrid case*.

Here the optimal investment costs are achieved at a FC oversizing of **28%**. With the given parameters, the *hybrid case* investment costs are slightly higher than the *FC only case*. Also here, the optimal oversizing in terms of investment costs are lower than the mass-optimized FC sizing[4]. As for the *FC only case*, this is mainly due to the estimated lifetime gain leveling out at higher oversizing factors.

7.1.2 Platinum Loading

The Pt loading in the catalyst will affect the performance, the degradation rate and the lifetime of the FC. Figure 7.3 shows the estimated operating lifetime of the FC at various Pt loadings and FC sizings for the *FC only case*. The estimated stack investment cost and total investment costs throughout the analysis period are also shown. The same can be seen for the mass-optimized *hybrid case*, including the fixed battery costs, in Fig. 7.4.

[4]Notice that this value is also slightly changed from 4.74 MW in the previous chapter because of the lower resolution on the iterative steps in this chapter.

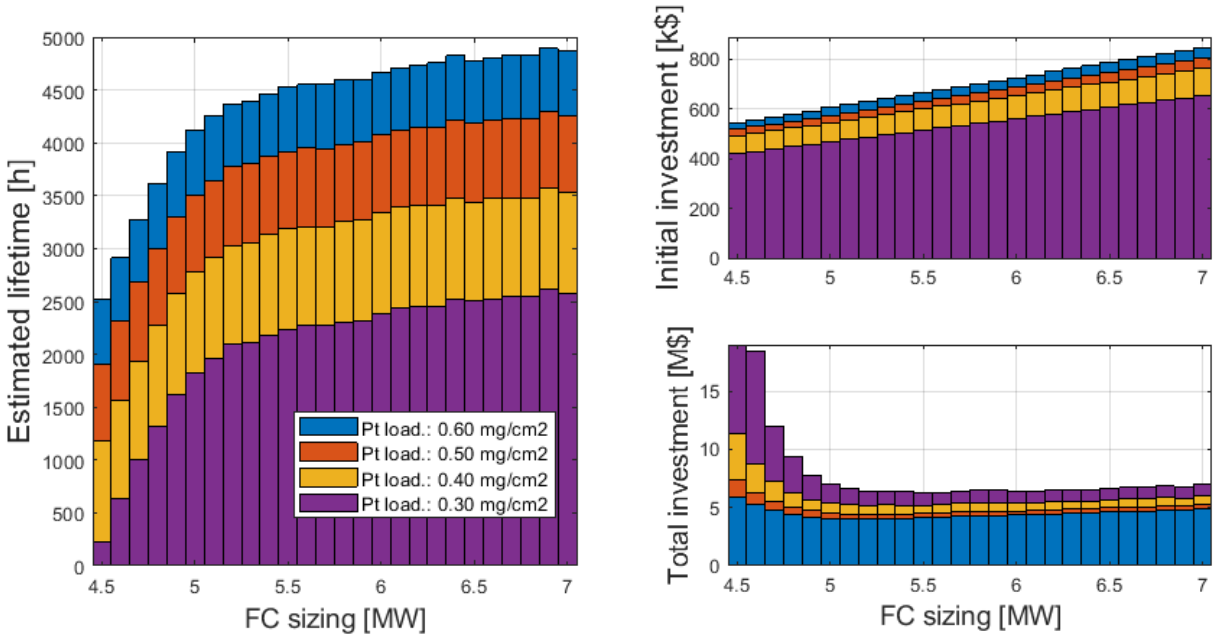

Figure 7.3: Estimated fuel cell (FC) lifetime and the initial and total investment costs of the power devices for the *FC only case*. Four variations on the platinum loading in the FC catalyst is included.

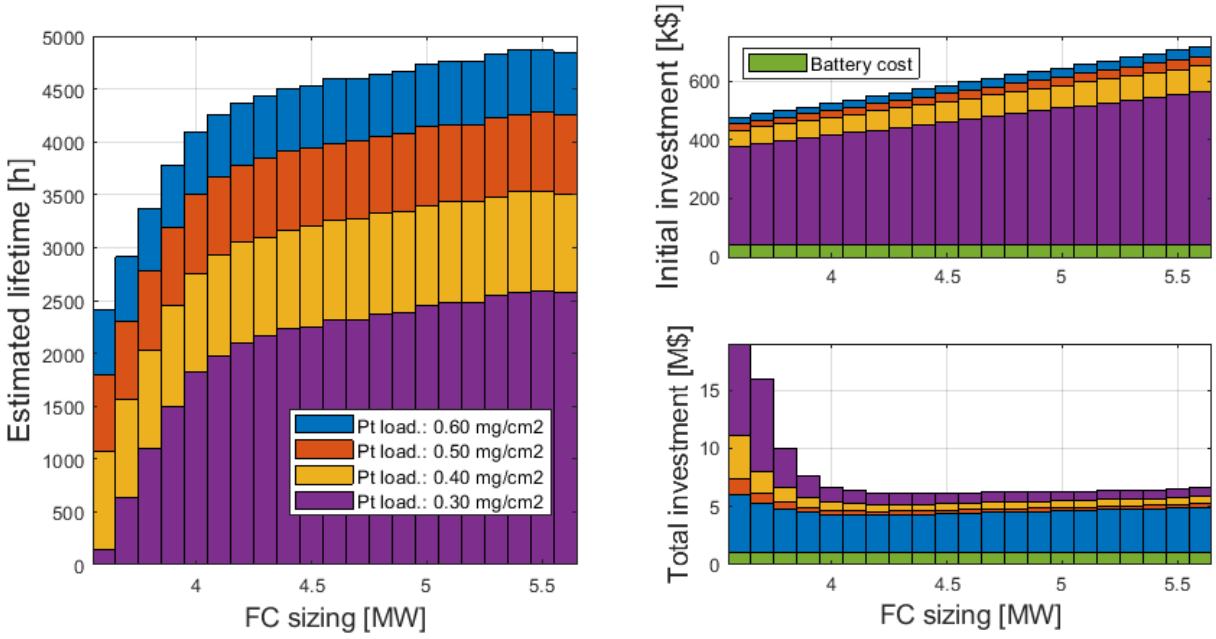

Figure 7.4: Estimated fuel cell (FC) lifetime and the initial and total investment costs of the power devices for the FC/battery *hybrid case*. Four variations on the platinum loading in the FC catalyst is included.

For each Pt loading, the cell count are kept equal to that of the reference case[5] for each evaluated FC sizing. Thus, with Pt loadings of 0.50 and 0.60 mg/cm^2 the FC power and efficiency curves are improved without increasing the FC mass[6], while 0.30 mg/cm^2 yields the opposite effect. The optimization model shows clear advantages of a high Pt loading in terms of total investment costs. Despite higher initial investments, the increased lifetime ensures a lower number of reinvestments throughout the period of analysis. The extended lifetime is explained by a more efficient operation, allowing the FC to remain at its reference operating temperature for a higher number of operating hours. In addition, less FC oversizing is required to meet the peak power towards the EoL due to the improved power curve at higher Pt loadings. This is in accordance with the improved performance and reduced degradation rate found for higher Pt loadings in [109]. Still, the commercialization of fuel cell-electric vehicles (FCEVs) may possibly drive the Pt prices further up. The element is not very abundant and largely exist in geopolitically unstable regions. This means there are also non-economic incentives for reducing the Pt loading. Particularly in the automotive industry, there are much focus on reducing the Pt loading to achieve competitive FC prices. However, while cars are lifted by their wheels, aircraft have to produce this lift by the power of their engines. This means that every kilogram of reduced weight counts. The results indicate that it may be beneficial to keep the Pt loading constant, or even increase it from current levels, despite the opposite trend in the automotive industry. Other important benefits of increasing the Pt loading is that the FC efficiency will increase, lowering both the tank and cooling system requirements. The consequence of an increased FC heat generation is also addressed as a clear limitation for the Pt use lowering, in [46].

7.2 Fuel Costs

Figure 7.5 shows how the fuel costs add to the total costs over the period of analysis for the varying FC sizings.

[5] $L_{Pt} = 0.40$ mg/cm^2 for the reference case.

[6] Assuming that the an increased Pt loading does not affect the FC weight.

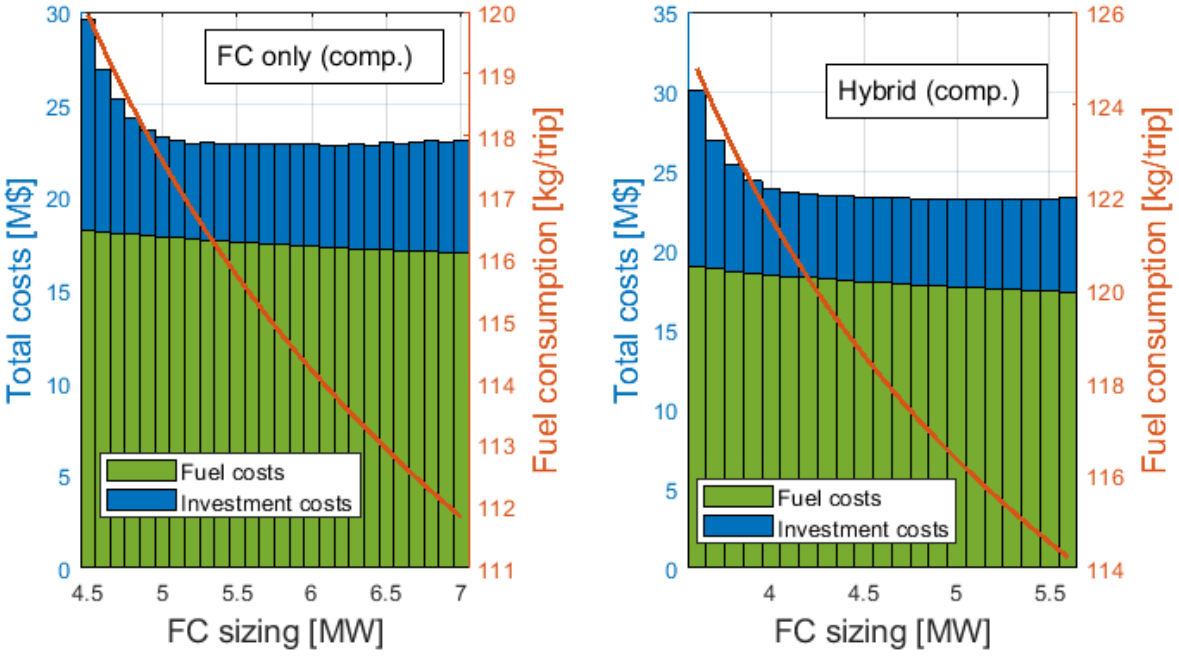

Figure 7.5: Fuel costs and investments costs for the *fuel cell only case* (left) and the *hybrid case* (right) with compressed (comp.) tanks.

The fuel consumption decreases as the FC sizing increases. Both the *FC only case* and the *hybrid case* have similar trends with relatively large sizing ranges showing little differences in total costs. The reason is that the lower investment costs at less oversizing, shown in Fig. 7.1 and Fig. 7.2, are leveled out by the reduced fuel costs at larger oversizings.

The fuel costs will be very sensitive to the price of hydrogen. This is illustrated in Fig. 7.6 and Fig. 7.7 for the *FC only case* and the *hybrid case*, respectively.

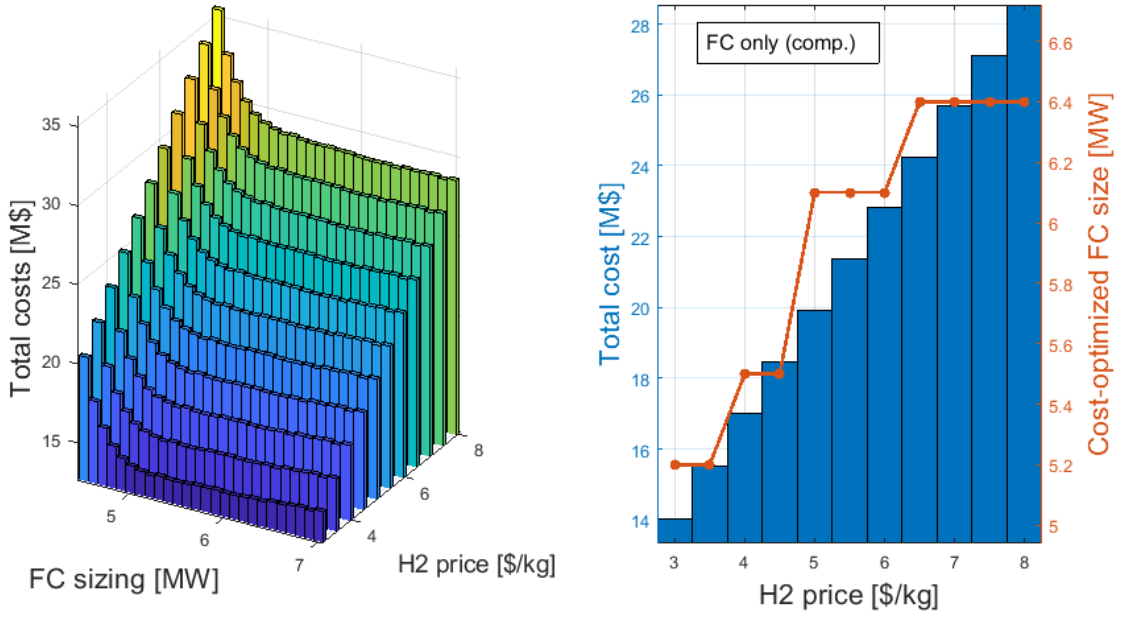

Figure 7.6: Sensitivity of the hydrogen price on the total costs for the *fuel cell only case*.

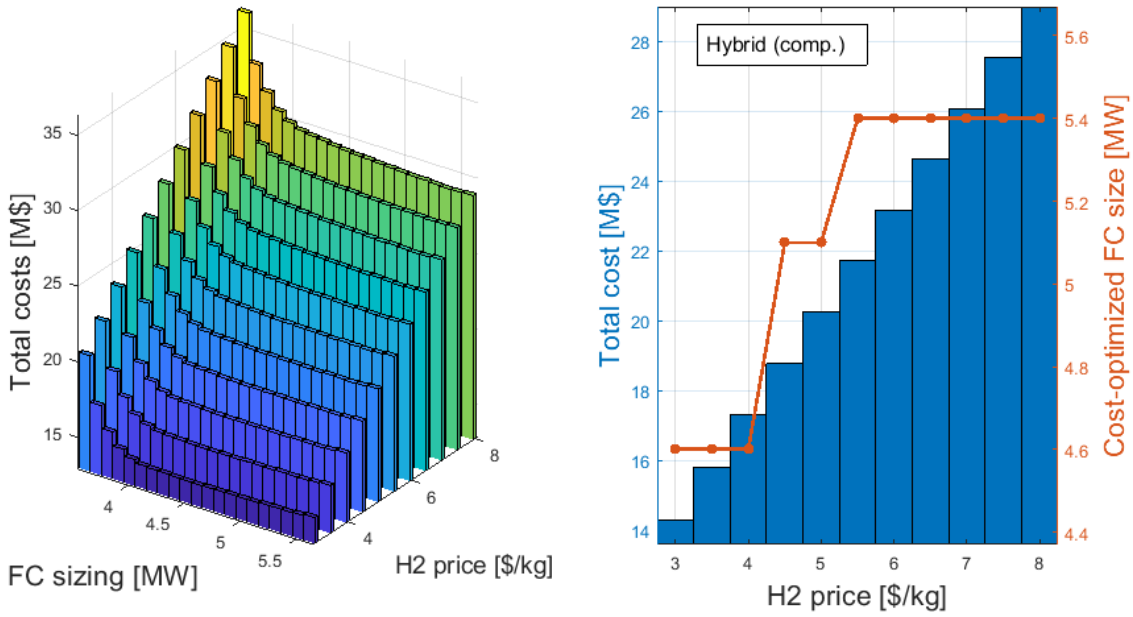

Figure 7.7: Sensitivity of the hydrogen price on the total costs for the *hybrid case*.

The cost-optimized FC sizing increases as the price of hydrogen increases. This trend is expected, as an oversized FC will bring a more efficient operation and, thus, reduce the fuel consumption. For the *FC only case*, a **60%** oversizing becomes optimal with a hydrogen price of **6.5 $/kg** or above. Given a hydrogen price of **3-3.5 $/kg**, the cost-optimized oversizing is only **30%**.

For the *hybrid case*, a **69%** oversizing is optimal already at hydrogen prices of **5.5 $/kg** or above. Between **3-4 $/kg**, the optimal oversizing is reduced to **44%**. Thus, there are large differences on the optimal FC sizing for different hydrogen price scenarios. Similarly, it can be expected to be a reversed trend with the initial investment costs of the FCS. If the FCS prices decrease faster than the hydrogen prices, more oversizing will be favourable and vice versa.

The above calculations do not evaluate the weight of each FC sizing. Increasing the FC size to achieve a more efficient power generation is ineffective if it results in an overall heavier aircraft. As the aircraft is assumed to operate at its maximum takeoff weight for all calculations, heavier energy systems will limit the payload capacity.

7.3 Cost per Available Seat Kilometer

The cost per available seat kilometer (CASK) measure makes it possible to somehow connect the economic and technical aspects of the optimization. Everything else equal, the weight of the energy system will limit the aircraft payload capacity, which can be translated to equivalent passengers[7] for convenience. This is done for both the *FC only case* and the *hybrid case*, considering both the compressed and the cryogenic storage technologies. The normalized[8] CASK is shown in Fig. 7.8 for all cases.

[7] Assuming 100 kg per PAX.

[8] CASK normalized on the optimal *FC only case* with compressed storage.

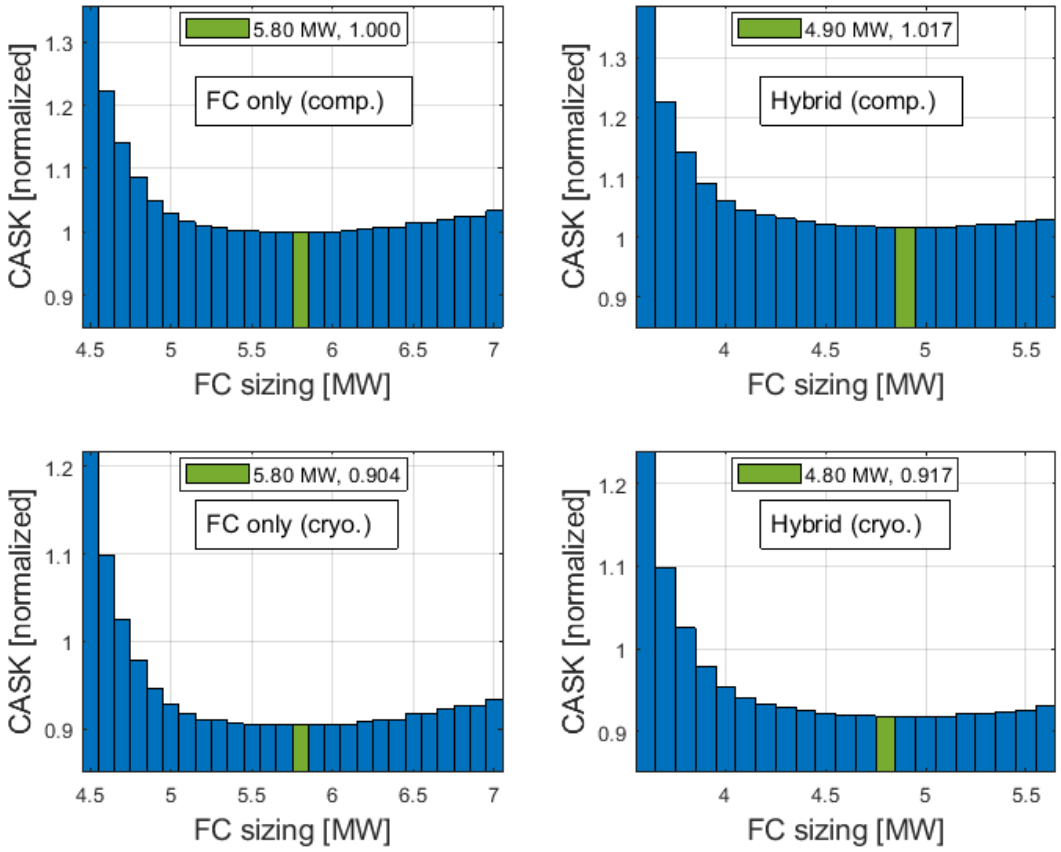

Figure 7.8: Cost per available seat kilometer (CASK) for the *FC only case* and the *hybrid case* with compressed (comp.) and with cryogenic (cryo.) tanks. The CASK is normalized to the optimal *FC only case* with compressed storage.

The estimated CASK is about **10%** lower with cryogenic tanks. This is primarily due to the reduced weight of the hydrogen tanks, increasing the aircraft payload capacity. With the base parameters, the *FC only case* is found to have a slightly lower CASK than the *hybrid case*. This is partly explained by the fact that the FC operates very efficiently at cruising power when it is sized to also cover the takeoff power. Figure 7.9 shows the same cases for the long-range mission profile.

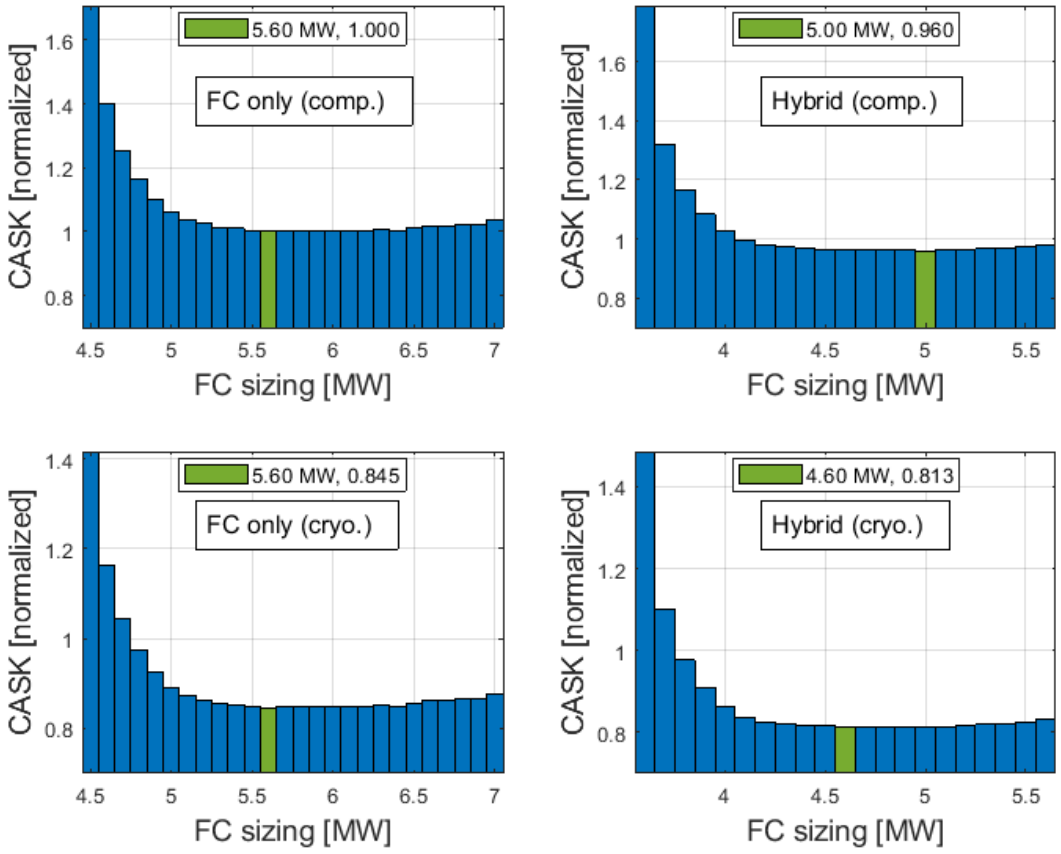

Figure 7.9: Long-range mission: Cost per available seat kilometer (CASK) for *FC only case* and *hybrid case* with compressed (comp.) and with cryogenic (cryo.) tanks. The CASK is normalized to the optimal *FC only case* with compressed storage.

This mission profile has a longer cruise phase and requires more fuel per flight. Thus, the advantage of storing the fuel cryogenically is even more pronounced, with above **15%** CASK reduction for both the *FC only case* and the *hybrid case*. For this mission profile, the *hybrid case* gives about **4%** reduction in the CASK compared to the *FC only case*.

The estimated CASK for the short-range and the standard missions can be found in Appendix D.2.3.

The cost-optimized FC sizings and the corresponding costs are summarized in Tab. 7.1 for some selected hybridization factors.

Table 7.1: Cost-optimized FC sizings and corresponding costs for different hybridization factors. (*)Translating battery energy to H_2 equivalent fuel consumption.

Hybridization	1.0	0.9	0.8	0.7	0.6
FC power	4 MW	3.6 MW	3.2 MW	2.8 MW	2.4 MW
Battery power	-	0.4 MW	0.8 MW	1.2 MW	1.6 MW
Cost-optimized FC size	5.8 MW	5.2 MW	4.9 MW	4.6 MW	4.4 MW
Battery cost [k$]	-	18.41	40.59	55.25	98.05
Operating life [cycles]	-	1000	1000	1000	1000
Total battery investments [M$]	-	0.4663	1.0279	1.3882	2.4828
FCS cost [M$]	0.6322	0.5668	0.5341	0.5014	0.4796
Operating life [hours]	3209	3232	3300	3459	3618
Total FCS investments [M$]	5.4429	4.8458	4.4756	4.0137	3.6747
Total investment costs [M$]	5.4429	**5.3121**	5.5035	5.4129	6.1575
Fuel costs [M$]	17.439	17.656	17.739	17.809	17.233
Payload capacity [kg]	3998	4002	3994	3899	3600
Eq. passengers	39.98	40.02	39.94	38.99	36.00
Total costs [M$]	**22.882**	22.971	23.242	23.222	23.390
CASK [normalized]	**1.000**	1.003	1.017	1.041	1.135
CASK [normalized] (*)	**1.000**	1.004	1.020	1.046	1.157

The optimal CASK is achieved with no hybridization. This means that the best combination of investment costs, fuel costs and energy system mass is achieved without any battery. Still, with hybridization factors of **0.9** and **0.8**, the CASK is only increasing with **0.3%** and **1.7%**, respectively. Further hybridization gives both higher total costs and significant payload capacity reductions, yielding more significant increases in the CASK. The corresponding results for the long-range mission profile are listed in Tab. 7.2.

Table 7.2: Long-range mission profile: Cost-optimized FC sizings and corresponding costs for different hybridization factors. (*)Translating battery energy to H_2 equivalent fuel consumption.

Hybridization	1.0	0.9	0.8	0.7	0.6
FC power	4 MW	3.6 MW	3.2 MW	2.8 MW	2.4 MW
Battery power	-	0.4 MW	0.8 MW	1.2 MW	1.6 MW
Cost-optimized FC size	5.6 MW	5.2 MW	5.0 MW	4.5 MW	4.4 MW
Battery cost [k$]	-	19.13	36.68	63.81	109.9
Operating life [cycles]	-	1000	1000	1000	1000
Total battery investments [M$]	-	0.4844	0.9289	1.6159	2.7822
FCS cost [M$]	0.6104	0.5668	0.5450	0.4905	0.4796
Operating life [hours]	3132	3180	3322	3369	3559
Total FCS investments [M$]	11.144	10.194	9.3822	8.3251	7.7062
Total investment costs [M$]	11.144	10.678	10.311	**9.9410**	10.488
Fuel costs [M$]	29.788	29.956	29.921	30.111	29.716
Payload capacity [kg]	3313	3332	3391	3298	2959
Eq. passengers	33.13	33.32	33.91	32.98	29.59
Total costs [M$]	40.933	40.634	40.232	**40.052**	40.204
CASK [normalized]	1.000	0.987	**0.960**	0.983	1.100
CASK [normalized] (*)	1.000	0.988	**0.964**	0.989	1.113

For this mission profile, a hybridization factor of **0.8** is found to give the lowest CASK. This is largely explained by a long FC lifetime, limiting the total investment costs. In addition, the long-range flight has a relatively low power cruise phase. This means that the FC will operate at a very high efficiency regardless of the smaller FC sizing compared to the *FC only case*. These differences between the mission profiles can be seen in Fig. 7.10.

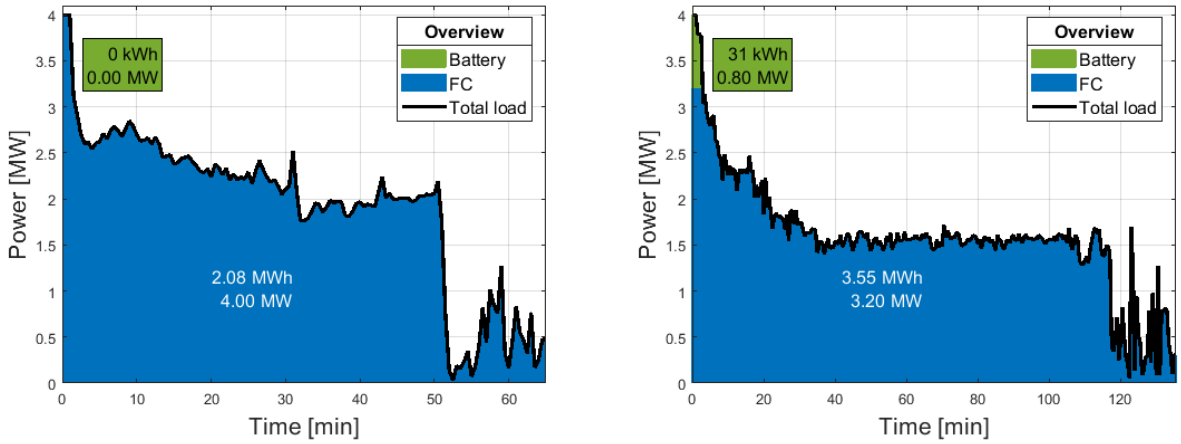

(a) Reference flight.

(b) Long-range flight.

Figure 7.10: Power sharing between battery and fuel cell.

The long-range flight has a longer and less demanding cruise phase than the reference flight. This means that the benefit of having a FC sized for the full takeoff power is less pronounced for this flight. Table 7.3 shows the CASK results for the short-range mission profile.

Table 7.3: Short-range mission profile: Cost-optimized FC sizings and corresponding costs for different hybridization factors. (*)Translating battery energy to H_2 equivalent fuel consumption.

Hybridization (short-range)	**1.0**	**0.9**	**0.8**	**0.7**	**0.6**
FC power	4 MW	3.6 MW	3.2 MW	2.8 MW	2.4 MW
Battery power	-	0.4 MW	0.8 MW	1.2 MW	1.6 MW
Cost-optimized FC size	5.6 MW	5.1 MW	5.0 MW	4.4 MW	3.7 MW
Battery cost [k$]	-	18.30	37.30	62.45	108.3
Operating life [cycles]	-	1000	1000	1000	1000
Total battery investments [M$]	-	0.4633	0.9447	1.5815	2.7429
FCS cost [M$]	0.6104	0.5559	0.5450	0.4796	0.4033
Operating life [hours]	3117	3129	3288	3299	3277
Total FCS investments [M$]	2.7756	2.5192	2.3570	2.0674	1.7499
Total investment costs [M$]	**2.7756**	2.9825	3.3017	3.6488	4.4928
Fuel costs [M$]	6.8479	6.8693	6.7592	6.5070	6.1322
Payload capacity [kg]	4681	4682	4595	4606	4479
Eq. passengers	46.81	46.82	45.95	46.06	44.79
Total costs [M$]	**9.6235**	9.8518	10.061	10.156	10.625
CASK [normalized]	**1.000**	1.023	1.065	1.072	1.154
CASK [normalized] (*)	**1.000**	1.027	1.074	1.099	1.207

As for the reference flight, no hybridization is found optimal for the short-range mission profile.

The total investment costs increase as the hybridization factor increases, due to the battery. The cycle life of the battery is assumed equal to that of the longer mission profiles, yielding a higher battery to FCS cost ratio. This assumption is not unreasonable as the battery operates for a larger share of the flight for the short-range mission. However, less FCS reinvestments are required throughout the period of analysis, as the number of daily flights are kept constant and independent of the length of each mission. Contrary to expectation, the short-range flight is found to be the least beneficial mission for hybridization. For such short ranges, and possibly with a slightly smaller reference aircraft, other more energy-dense reference batteries should be evaluated. When the battery is sized for a larger share of the energy requirement, such that the battery is dimensioned on energy rather than power, more moderate C-rates will be applicable due to a higher battery capacity.

7.4 Actual Payload Estimation

With the operating empty weight (OEW) of 11 793 kg and two engines weighing 450 kg each, the conventional base weight can be assumed to be 10 893 kg [81]. For each mission profile, the remaining payload capacity after including the respective CASK-optimal energy systems and other key electrical components can be roughly estimated as,

$$m_{payload} = m_{TOW} - (10\,893 + m_{motor} + m_{DC/DC} + m_{inverter} + m_{fcs} + m_{tank} + m_{H_2})$$

where m_{TOW} is the maximum takeoff weight. The HEXs are not included as the conventional aircraft will also have cooling loops with unknown mass contributions. The power densities of key electrical components discussed in Section 2.6 are summarized in Tab. 7.4, including both the current status and future projections.

Table 7.4: Current status and future projections on power densities for key electrical components. A power management and distribution efficiency of 97% is assumed, as in [3].

	Efficiency		**Power density [kW/kg]**		**Power req. [MW]**		**Mass [kg]**	
Component	Current	Future	Current	Future	Current	Future	Current	Future
Motor	95%	96%	4.9	13	3.6	3.6	734.7	276.9
Inverter	98%	99%	8.3	19	3.79	3.75	456.6	197.4
DC-DC converter	98%	99%	8.3	19	3.99	3.91	480.7	205.8
Fuel cell system	-	-	-	1.75	4.07	3.94	-	2251

Using these values, the estimated payload capacity is calculated for all four mission profiles and shown in Tab. 7.5.

Table 7.5: Payload capacity estimations for four mission profiles. (*)Using current power densities on key electrical components. (**)Using future power densities on key electrical components.

Flight	Storage	FCS [kg]	Tank [kg]	H2 [kg]	Total [kg]	Payload capacity*	Payload capacity**
Reference	Comp.	3483	1105	229.6	4817	2123	3115
526 km	Cryo.	3483	680.5	229.6	4393	2547	3539
Long-range	Comp.	3471	1578	392.1	5441	**1499**	2491
1093 km	Cryo.	3471	972.5	392.1	4835	2105	3096
Short-range	Comp.	3417	592.3	90.1	4099	2841	3833
187 km	Cryo.	3417	364.9	90.1	3872	3068	**4060**
Standard	Comp.	3503	1160	246.9	4910	2031	3022
407 km	Cryo.	3503	714.5	246.9	4465	2476	3467

The conventional aircraft has a maximum payload capacity of 6124 kg and a maximum range of 1711 km while carrying 50 passengers [75]. With the current technology level in the main electric components, the reference flight has an estimated payload capacity of **2123 kg**. With cryogenic storage, the corresponding capacity is **2547 kg**. This means that the economic profitability will suffer. Even with future projections for electric motors and power electronic converters, the payload capacity is significantly lower than for the conventional aircraft. For the shortest range and cryogenic storage, a payload of **4060 kg** is estimated, in this case. Note that cryogenic storage can enable cryogenic cooling concepts that may possibly push the component performances beyond the future projections in Tab. 7.4. For all cases, further improvements are required on the FCS and hydrogen storage technology. With the projected 1.75 kW/kg power density and 30% gravimetric efficiency for the FCS and hydrogen storage, the combined mass of these components will be **3246 kg**[9] for the reference mission [3]. This yields an estimated payload capacity of **4686 kg**. For the long-range flight the corresponding payload estimation is **3982 kg**. These numbers are in line with the Universal Hydrogen project estimate, where 16 seats are planned to be removed from the conventional reference aircraft. Keep in mind that the calculations do only consider the replacements of the main propulsion system components and are neglecting differences in the aircraft cooling system and other infrastructure changes. The fuel margin factor of two, used to calculate the total hydrogen requirement may also be slightly exaggerated. In reality, the requirement will vary with each route and depend on such as the alternate possibilities and the weather conditions. The minimum fuel reserve requirement of 45 minutes at cruising altitude will be more significant for short-range flight than the long-range flight [110]. However, this high-level payload capacity estimation indicates that further technology developments are required to compete with the conventional propulsion system on mass.

[9] Assuming the future FC power requirement to be 3.94 MW for the reference aircraft with the given efficiencies.

Chapter 8

Testing and Discussion

The final CASK results from Section 7.3 are repeated in Tab. 8.1.

Table 8.1: Final CASK results for reference, long-range and short-range flight missions.

CASK-optimized			
	Reference	Long-range	Short-range
Hybridization factor	1.0	0.8	1.0
Battery power	0 MW	0.8 MW	0 MW
FC power	4 MW	3.2 MW	4 MW
FC oversizing	45.0%	56.3%	40.0%

While the *FC only case* is optimal for the reference flight and the short-range flight, a hybridization factor of 0.8 is optimal for the long-range flight. In all cases, there are only small differences between systems with and without some battery power boosting for the takeoff and the initial climb. Thus, the implications of fast dynamics and system response requirements are important considerations to supplement the power balancing optimality.

8.1 Dynamics and Response Time

A concern when operating without the battery is whether the FCS is capable of meeting the power response requirement of the aircraft.

8.1.1 Power Ramp Case

Figure 8.1 shows how the CASK-optimal hybridization[1], with 0.8 MW battery power, responds to the power ramp case presented in Section 4.1.

[1] Optimization for the long-range mission is used.

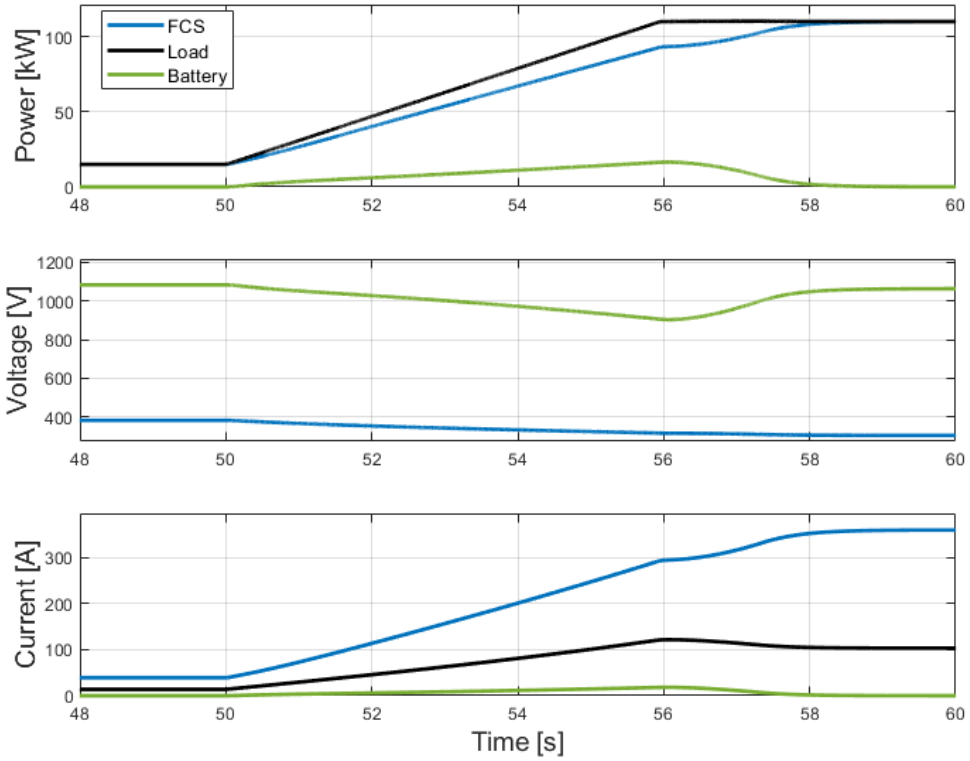

Figure 8.1: Power ramp case for CASK-optimized hybridization.

The battery automatically supplies the power shortage of the FCS due to the ramp-up limit, causing a significant voltage drop at the DC-link. When the load ramp occurs, the DC-link voltage is about 1100 V due to an unloaded and fully charged battery. The battery discharge current brings the voltage down to about 90% of its nominal value[2]. However, the FC catches up with the load fast enough to prevent any violation of system limits. Thus, including a battery in the energy system can help meet power response requirements set by regulatory authorities. If a DC-link capacitor was to serve the same purpose, it would be unreasonably large. Keep in mind that the FC ramp-up limit normally is suggested for normal operation to prevent conditions that can accelerate the lifetime degradation. In emergencies, it is reasonable to assume that this limit can be violated, particularly if the FCS is operated with an appropriate air excess ratio to avoid oxygen depletion. This assumption is substantiated by the transient response time of 1 second[3] reported by DoE for air compressors in transportation FCSs. In the same way as conventional gas turbine engines, the transient response of the FCS depends mainly on the fuel supply. An interesting consideration is to which extent the introduction of a battery could limit the FC air excess requirement without restraining the dynamic capabilities of the power system.

[2] 1000 V.

[3] From 10% to 90% of maximum flow.

This would allow the FCS to operate with lower parasitic compressor losses at low loads.

8.1.2 Load Loss Case

Figure 8.2 shows how the CASK-optimal hybridization responds to the load loss case presented in Section 4.2.

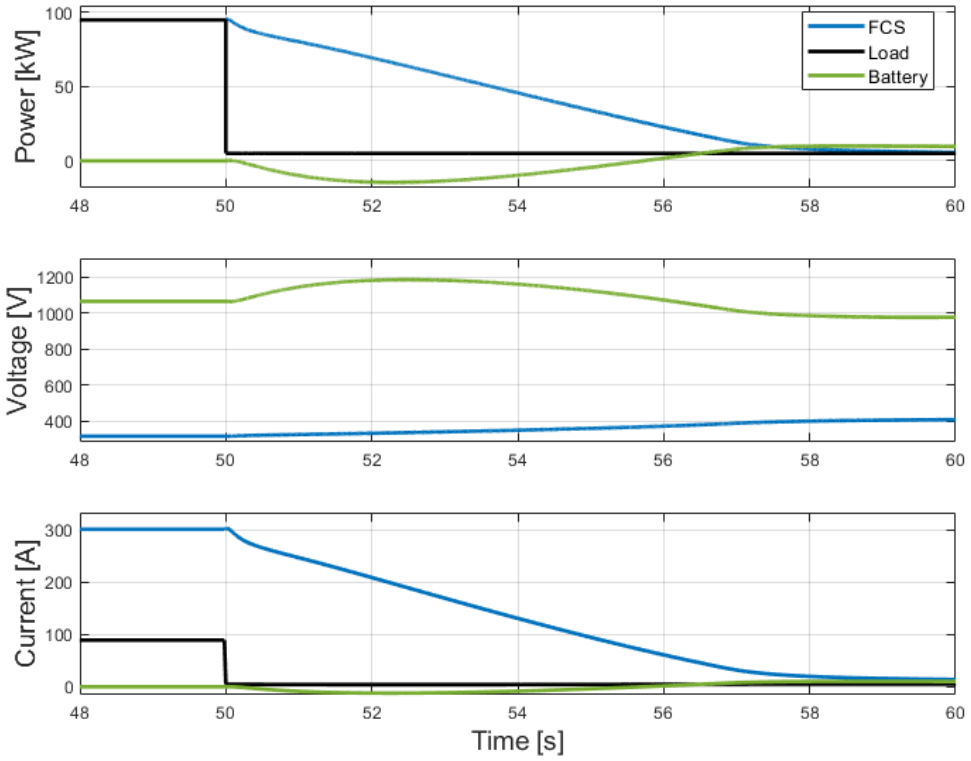

Figure 8.2: Load loss case for CASK-optimized hybridization.

When the load loss occurs, the FCS power drops with the limited ramp-down rate. Initially, about 90 kW is rejected in the braking resistor, while at most 15 kW is consumed by the battery. Here, the battery is limited by its recommended continuous charge current limit. For short durations, it is reasonable to believe that the battery can consume a larger share of the FC power. For less dramatic, but more frequent, load variations, it may even be possible to avoid ramping down the FC by allowing the battery to consume the excess energy at the DC-link. A more constant FC power output is known to increase its efficiency in operation.

8.1.3 Switching Conditions and Fast Dynamics

As long as the switching frequency of the power electronic converters are in the kHz range, the literature indicate that the filtering requirements at the FC side are minimal. Due to the capac-

itive effect of the FC double-layer, typical input side capacitors can be omitted. As long as the switching is fast enough, the FC voltage variations will mainly be related to the ohmic membrane resistance. The input inductor of the converter must somehow limit the ripple current to prevent excessive ohmic losses in both the inductor itself and the FC stack. The only concern, as addressed in the literature, is that high ripple currents may heat up the FC membrane and cause mechanical stress on the component. Due to the accelerating effect of a degraded membrane, precise recommendations on the ripple current limitation should be based on further experimental studies on the membrane conditions. For aircraft applications, it is important to quantify this effect to avoid the use of unnecessarily bulky inductors.

However, it is more essential that slower dynamics and load changes are filtered at the DC-link, as these variations are interacting with the frequencies of activation losses, and even reactant concentration losses. This will alter both the FC lifetime and performance. Having a battery in the system can also relief the FC from fast load variations, increase the system efficiency and help stabilizing the DC-link. Also supercapacitors are interesting for the same purposes due to their fast response time and great durability. The FC polarization curve is not representative for operation with fast load variations. To evaluate the quantified impact alternative modelling approaches, such as lumped-element models, must be applied.

8.2 Power Balancing

In sum, there are little economic differences found between the *FC only case* and hybridization with small batteries in terms of power balancing. The advantages of an improved response time and a more efficient operation, enabled by the battery, suggest that the hybridization is likely to give the most optimal overall operation. To illustrate the power sharing and discharge characteristics of the power devices, the power balancing is also performed by simulation for the CASK-optimal *hybrid case*. Thus, in all the simulations below, a 0.8 MW battery and a 3.2 MW FC overdimensioned by 56.3% are used.

Figure 8.3a shows the power, voltage and current profiles of the power devices for the medium-range reference flight. In Fig. 8.3b, the FC energy, reactant consumption and water generation are presented.

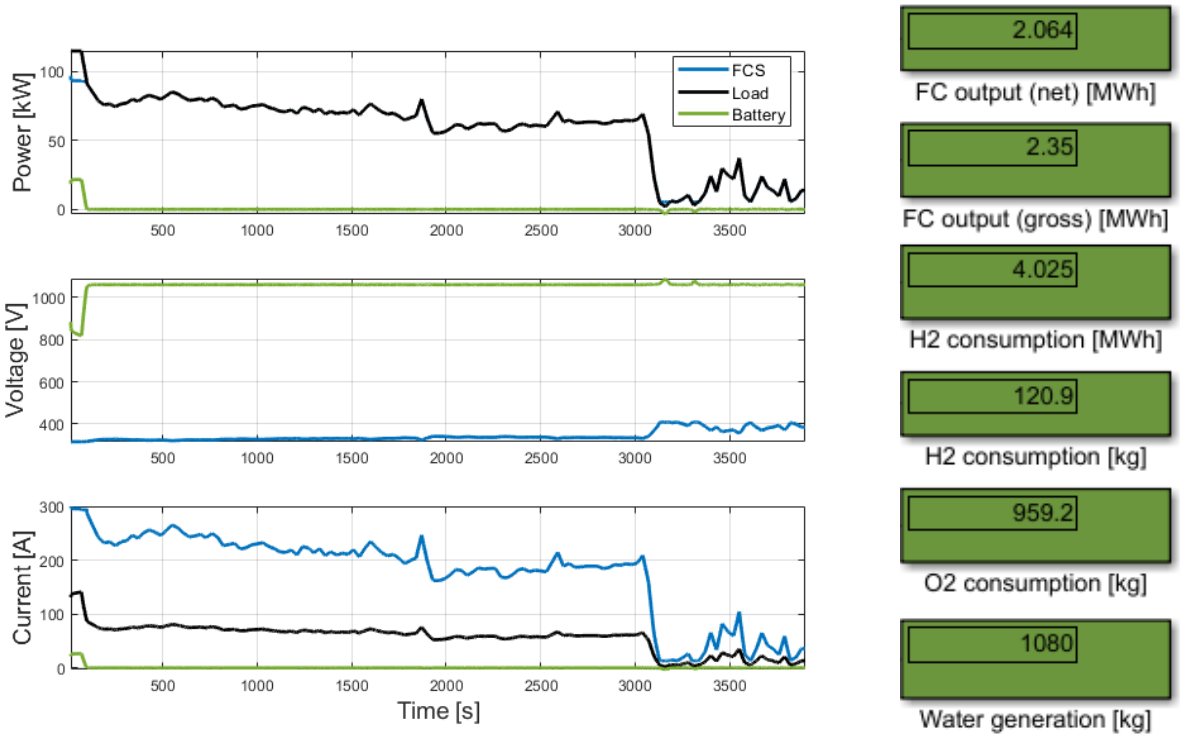

(a) Power sharing between fuel cell system and battery.

(b) Fuel cell energy.

Figure 8.3: Mission characteristics for the medium-range reference flight.

The DC-link voltage drops during the takeoff due to the high battery discharge and the decreasing SOC. After the initial phases, the FC supply the exact load power by itself. The only exception is during the aircraft descent after about 3100 seconds, where the load drop is too fast for the ramp-down limitation of the FCS and the battery is lightly charged by the excess energy at the DC-link. With a proper EMS strategy, the battery could allow a more leveled out FC power by acting on the faster load variations. From Fig. 8.3b, it can be seen that about **58.4%** of the hydrogen energy is converted to FC output power. From this, **12.2%** is consumed by the BoP components. The simulation gives close to identical results as the numerical modelling, as expected. The convenience of the simulation model can be further utilized is future works.

Similar simulation plots can be found for the long-range, the short-range and the standard mission profiles in Appendix E.1.

8.3 Additional Discussion

Given the reference devices, neither mass or cost optimizations give incentives to include bulk energy batteries in terms of power balancing. The trend towards smaller hybrid batteries is also implied in statements made by significant persons within the industry, such as Eremenko[4] and

[4] CEO of Universal Hydrogen

Kiselev[5]. With today's batteries, the energy density is too low to account for large shares of the regional aircraft energy. With energy requirements in the MWh range, hydrogen is much more competitive with conventional fuels, even when accounting for the heavy tanks and the FCSs. Cryogenic tanks show particularly promising weight efficiencies. The lowered tank mass, combined with the possibility for cryogenic cooling, will reduce the system weight through higher efficiencies and more compact cooling systems. This, in turn, will result in a lower fuel consumption and further reduced tank requirements. While cryogenic storage gives a better mass performance than compressed storage, the volume gain may be just as important by preventing bulky aircraft fuselages and wings to cope with the low volumetric density of gaseous hydrogen. Large hydrogen tanks may bring an increased parasitic aircraft drag and compromise on the aircraft passenger and cargo space, yielding a higher fuel consumption and a lower economic potential. If technical challenges related to cryogenic storage are solved, this technology will be a key enabler of larger hydrogen aircraft. A higher technological readiness level and the high energy requirement of liquefaction are still arguments forwarded for using compressed tanks in current hydrogen aircraft projects.

Including batteries for power boosting in the very first fractions of the flight gives very similar results as FC only operation. Besides the high power capability of the reference battery, the lowered aircraft cooling requirement is an important effect of supplementing the FCs with efficient batteries during takeoff. If cryogenic cooling concepts are enabled in the future, this effect may become lower. The implications of having devices operating at different temperatures will also bring an increased number of separate cooling loops. In addition, the combination of different power sources for the propulsion may complicate certification processes compared to conventional jet turbines. These are arguments for pursuing systems with pure FC-propulsion, limiting the application of batteries to cold-start assistance and uninterruptible power supply of critical aircraft loads and instruments[6]. To achieve this, a satisfying response time and efficiency[7], with moderate air excess ratios, must be ensured by the FCS. In addition, the complication of the aircraft heat rejection must also be improved, either by more efficient FCSs or cryogenic cooling concepts. Until then, including power boosting batteries in the energy system seems appropriate.

[5]Vice president of ZeroAvia

[6]Typical applications of batteries in conventional aircraft.

[7]Despite certain load variations.

Chapter 9

Conclusion and Recommendations for Further Work

9.1 Conclusion

The optimal combination of a FCS and a battery for aircraft propulsion has been evaluated by quantitative and qualitative considerations for specific mission profiles. By using a reference aircraft, FC stack and battery, the optimal power sharing between the power devices has been investigated based on the combined energy system mass, investment costs and fuel costs. The development of a dynamic optimization model has enabled a more detailed investigation of the operation of the power devices, compared to other similar work. This model is used to obtain such as the power, voltage, efficiency and temperature curves. This information is useful in the design of BoP components and the aircraft cooling system. Furthermore, the voltage and temperature curves are used to estimate the FC lifetime based on the FC sizing and the relevant mission profile.

Quantitative power balancing optimizations showed similar system masses and cost information for energy systems with only FCs and systems including small power boosting batteries. For the longest analyzed flight of 1093 km, the combined technical and economic optimality was found with a hybridization factor of 0.8. This yields a 3.2 MW FC power and a 0.8 MW battery power to meet the 4 MW propulsion load. A corresponding FC sizing of 5.0 MW (56.3% oversizing) was shown to give the best overall weight and costs, with a 4% reduced CASK compared to the *FC only case*. For the 526 km reference flight and the 187 km short-range flight, FC only propulsion was found to be optimal. In these cases, the optimal FC sizings were 5.8 MW and 5.6 MW (45% and 40% oversizing), respectively. For both mission profiles, light hybridizations with power batteries were only slightly inferior. For the reference mission, the *FC only case* showed only 1.7% CASK-reductions from the *hybrid case* with a hybridization factor of 0.8. For the short-range flight, the same reduction was 6.5%.

The benefits of hybridizing the FC with power boosting batteries, for power balancing considerations, are found in the higher power density of the reference battery and the lowered heat generation throughout the most demanding flight phases, due to the high battery efficiency. However, these benefits are more or less leveled out by the lowered FCS efficiency during the less demanding flight phases. The consequence is that the optimal FC oversizing percentage are higher for the *hybrid case* than for the *FC only case*. The advantages of a significantly oversized FC are mainly related to the extended FC lifetime and the improved efficiency. The FC must for all purposes be slightly oversized to meet the peak power requirement towards the EoL. With a larger FC, the power device can be operated at a lower current density, avoiding operation in the mass transport region. This will limit the heat generation and the parasitic consumption of the BoP components of the FCS. The lowered heat generation yields lower cooling system and HEX requirements, improving the combined system mass. Also, excessive temperatures, accelerating the degradation rate of the FC, are restricted by the reduced heat generation.

Faster dynamics, such as load variations, transient events and switching conditions, were investigated from a qualitative perspective. Low frequency ripple currents and load variations were suggested to be much more concerning than high frequency ripple currents, due to the activation of electrochemical and mass transport processes in the FC. The main concern for switching in the kHz range is suggested to be the possible heating and mechanical stress on the FC membrane at high ripple factors. Contrarily, slower variations can have a significant effect on the FC performance and lifetime. With batteries in the energy system, the FC can operate at a more constant power level by assigning the fast variations to the battery. In addition, the faster response time of batteries can help meet system response time requirements without operating the FC at very high air excess ratios. In sum, the qualitative investigations suggest that battery hybridizations bring certain advantages in terms of power ramping and FCS operating efficiency.

1. Due to the sensitivity of key parameters for the reference devices, one should be careful to make definite suggestions on the optimality in the general case. With the given mission profiles and power devices, the combined results and investigations point in the direction of including batteries for power boosting as the best overall option. A hybridization factor of 0.8 with a FC sizing around 5.0 MW gives good results for all the evaluated mission profiles, and particularly the longest flight.

2. The power balancing is incorporated quantitatively in the numerical optimization, and is also implemented and performed by graphic simulations. Contrarily, the impact of switching conditions are solely based on quantitative considerations. This is mainly due to the lack of available data, complicating the effort to address the topic from a quantitative perspective. Thus, a further evaluation and quantification of the impact of power

converter switching, and other fast dynamics, remain as important subjects of investigation.

The benefits of supplementing the FC with a battery are not unexpected, as batteries are commonly deployed in current FC-electric aircraft projects. However, there are clear indications that the battery size should be reduced and primarily used for power boosting during demanding flight phases, rather than contribute with bulk energy. FC only operation was shown to be more favourable than expected based on existing aircraft projects and similar literature. An important reason for this may be the lack of dedicated analyses, where the FCS and its surrounding components are optimized for specific applications. This is also a limitation of this work.

Limitations

An essential reservation is that the results are specific for the reference power devices and the investigate flight missions. With the rapid development in the performance of the power devices, as well as possible radical changes to how aircraft are operated, the problem may change significantly. An equivalent strength of the approach is that such changes easily can be applied to the optimization model to obtain updated aircraft mission profiles and power device specifications.

As the technology is relatively immature and rapidly evolving, frequent device replacements may be somehow advantageous. Thus, one could discuss whether the value of long device lifetimes are overestimated. This falls into the same area of discussion as the discount rate.

For completeness, more components should be included in the optimization. The power electronic converters and the DC-link are key components that are appropriate to include when expanding the scope of the optimization in further works.

9.2 Recommendations for Further Work

Switching conditions and fast dynamics: The impact of high frequency current ripple from power converters on the FC lifetime and performance should be further investigated to enable optimal designs of the power conversion. Particularly the FC membrane is of concern and should be tested with appropriate experimental stress tests. In this context, also the propagation of CM noise and the EMI tolerance of the FC stack should be addressed. Also the impact of transients and load variations on the FC lifetime and performance should be further investigated to enable calculations on the quantified benefit of including batteries in the system. This is addressed in [111].

Power devices: Put effort into finding a battery chemistry and design with an optimal trade-off

between power and energy. A possible approach can be found in [112].

Peripheral components: Develop more precise models for the balance-of-plants components. Submodels can be replaced or improved, while keeping the main structure of the numerical model. Also, increasing the scope of the optimization to also include power conversion, transmission. Particularly, an assessment of the complete TMS and the optimal power system voltage level should be investigated. The latter is investigated in [92].

Volume and drag: Introduce volume calculations and drag contributions from voluminous hydrogen tanks and air-cooled HEXs. This can be valuable for comparisons with conventional design concepts and to investigate the optimal design of hydrogen aircraft. In [77], the zero-lift drag contribution from various aircraft parts are studied. The hydrogen tank volume can be estimated by the relations given in Section 2.2.3.

Appendix A

Acronyms

AEA All-electric aircraft
BMS Battery management system
BoP Balance-of-plant
CCL Cathode catalyst layer
CHE Compact heat exchanger
CH_2 Compressed hydrogen
DOE U.S. Department of Energy
ECSA Electrochemically active surface area
EEC Equivalent electrical circuit
EIS Electrochemical impedance spectroscopy
EMI Electromagnetic interference
EoL End-of-life
ES Energy storage
EV Electrical vehicle
FC Fuel cell
FCS Fuel cell system
HEX Heat exchanger
LH_2 Liquid hydrogen
MEA Membrane electrode assembly
MPP Maximum power point
OCV Open-circuit voltage
ORR Oxygen reduction reaction
PEMFC Proton-exchange membrane fuel cell
SOC State-of-charge
SC Supercapacitor
TMS Thermal management system

Appendix B

Theoretical Background

B.1 Degradation and Operational Limits

Catalyst Layer

One key issue in FC degradation is the loss of electrochemical active surface area (ECSA) due to Ostwald ripening or sintering [113]. Ostwald ripening relates to the growth of platinum (Pt) particles through dissolution and re-deposition on larger particles [28]. Sintering is the agglomeration of Pt atoms into larger clusters through reorganization inside the catalyst layer [114]. Even though Pt loading is not necessarily decreased, both phenomena limit the active surface area of the catalyst. Another degradation mechanism of the ECSA is imposed by corrosion of the catalyst carbon support [115]. This phenomenon is affected by start-up and shut-down cycling, as corrosion at the cathode can be a consequence of the high potentials caused by oxygen crossover to the anode side [48]. Even though the anode side also may suffer from repeated starts and stops, it is the corrosion at the cathode side that is considered as the most important in terms of FC lifetime and performance [116]. The mechanism leads to large increase in the oxygen transport resistance [26]. High temperature and open-circuit voltage (OCV) operation are also reported to cause carbon corrosion [26].

Membrane

Membrane degradation includes loss in ohmic conductivity and increase in reactants permeability [117]. The ohmic losses in the membrane are related to the conduction of protons. This conductivity can be decreased by impurity contamination from other MEA components or from the fuel gases [117]. Increased conductivity losses in the membrane results in a degraded FC performance. An increased reactant permeability of the membrane also yields problems, as it facilitates increased hydrogen crossover to the cathode and oxygen crossover to the anode. This causes local overheating due to a direct reaction between the reactants, as well as degradation of both the catalyst layer and the membrane due to the production of hydrogen peroxide (H_2O_2)

[113][117]. A significant amount of H_2O_2 can be formed at the anode at lower potentials [48]. The combination of low potentials and high gas crossover is, thus, unwanted [118]. The mechanical degradation and thinning of the membrane accelerate the process and the membrane suffers from a self-reinforcing degradation effect. Membrane thinning can also be accelerated by high voltage operation at high temperatures [26]. A thinner membrane will be more vulnerable to mechanical stress and, thus, potential FC breakdown [113]. Differences in pressure at the anode and cathode, and membrane dehydration, are also typical mechanisms leading to mechanical membrane degradation [115].

Gas Diffusion Layer

Degradation of the gas diffusion layer (GDL) leads to decrease in mass transport, higher conductivity losses and a reduced control of the humidification [23][115]. A key degradation mechanism is corrosion and mechanical stress caused by changes in material hydrophobicity [113]. The reduced water management control may in turn lead to accelerated degradation, especially in the humidification sensitive membrane.

Water Management

Both dehydration and excess of water can be damaging to the FC. If the membrane is dehydrated, its ohmic resistance will increase significantly [115]. Long-time dehydration may also result in mechanical degradation such as cracks and pinholes in the membrane [113]. In the case of water excess, called flooding, the gas transport to the cell may be hindered, resulting in a decreased FC performance and potentially gas starvation [119]. In addition, high humidity accelerates the degradation of the MEA components [28][115].

Thermal Management

PEMFCs are normally operated around 60-80^{o}C, and below 90^{o}C, and they require cautious temperature management [23][115]. The cell temperature strongly affects the cell operation, and each FC has its optimal operating temperature. [23]. An increasing temperature can enhance FC performance in terms of gas diffusion and reaction kinetics [115]. Therefore, the optimal temperature will be a trade-off between efficiency and the acceleration of degradation mechanisms. The temperature is particularly important due to its influence on gas humidity and, thus, the hydration level in the cell [115]. At sub-zero temperatures, freeze/thaw operation can lead to mechanical damage on both the catalyst layer, the membrane and the GDL [23][113][115]. Under these conditions, rapid heating of the FC stack is usually desirable, as it can prevent ice formation and the corresponding blocking of the flow channels [120].

Appendix C

Modelling and Simulation

C.1 Simulation Model

The power balancing simulations are solved discretely with a sample time of 0.02 seconds. This gives at least 50 times the resolution of the various submodels, while enabling full mission profile simulations within a few minutes. If the converter switching conditions are to be evaluated, a much lower sample time must be applied.

C.1.1 Fuel Cell System

The fuel cell system (FCS) consists of the FC stack and balance-of-plant (BoP) components, as illustrated by Fig. C.1.

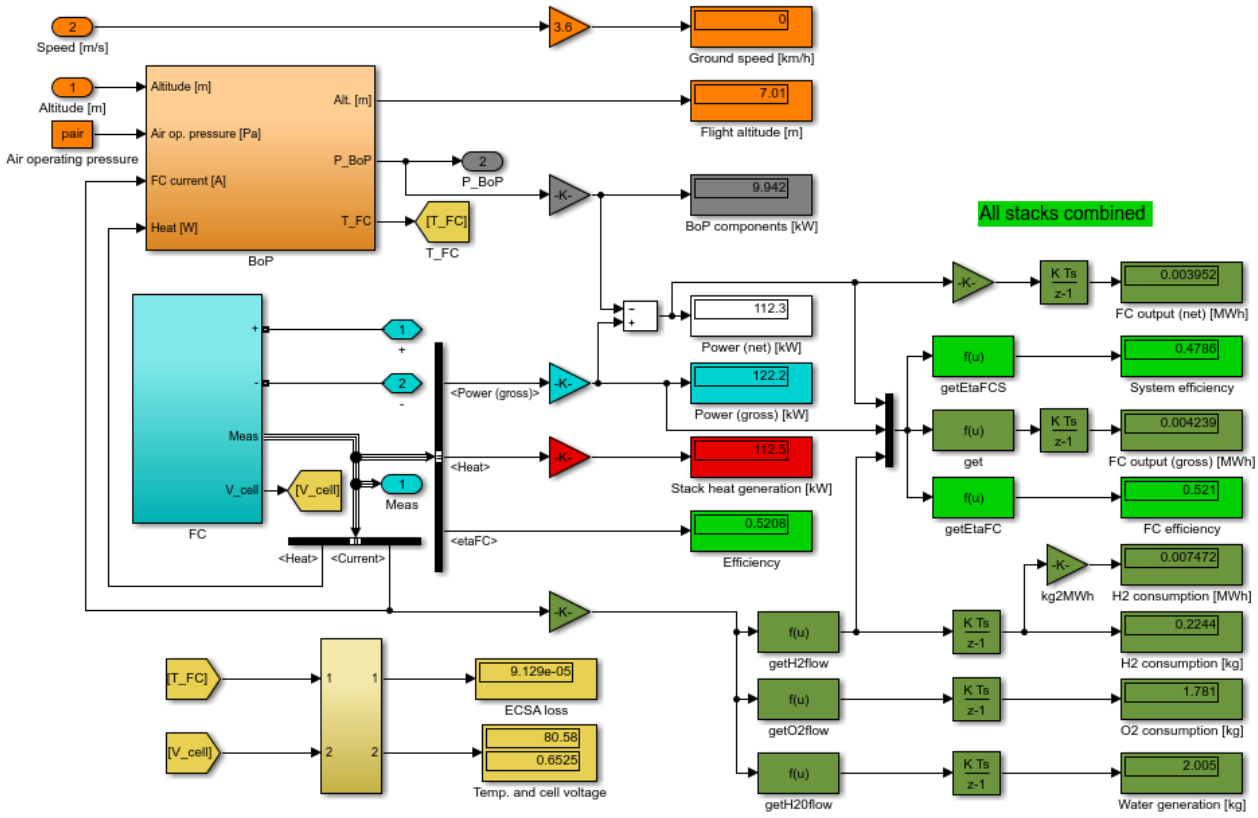

Figure C.1: Fuel cell system

Fuel Cell Stack

The voltage response of the FC stack is modelled by a look-up table with pre-calculated current and voltage relations. In this way, the behaviour will imitate the estimated polarization curve with negligible computational costs. This approach has the limitation of assuming static FC stack conditions. The set-up is depicted in Fig. C.2.

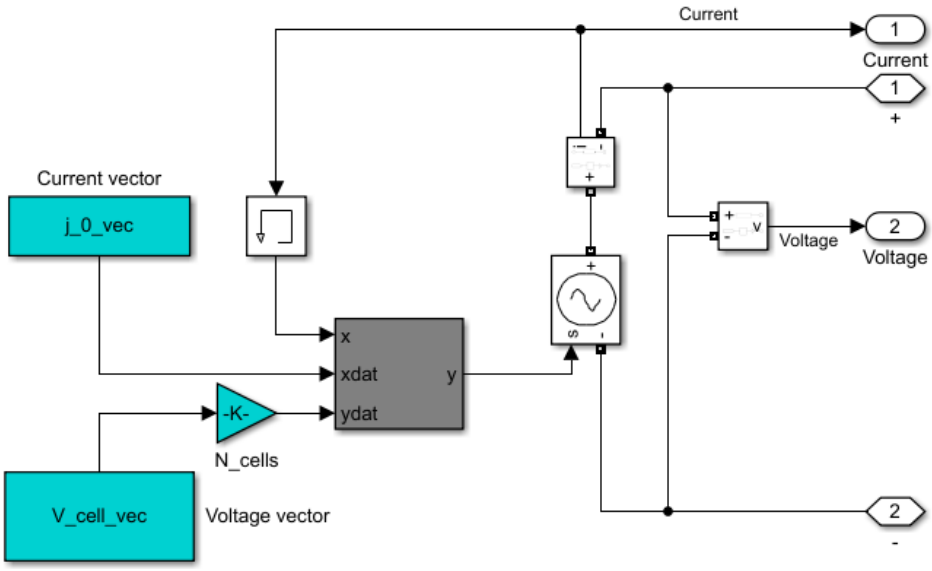

Figure C.2: Fuel cell stack

By small adjustments, the model can take both the air pressure and the stack temperature as inputs to dynamically update the polarization curve. This is not possible for the relative humidity, as it is not explicitly modelled. Another limitation of the model is that it does not consider transient FC response phenomena, such as voltage undershoots during load steps. Such constraints are instead handled by control system limitations.

Balance-of-Plant Components

The modelled BoP components are the cooling system and the air compressor, as shown in Fig. C.3.

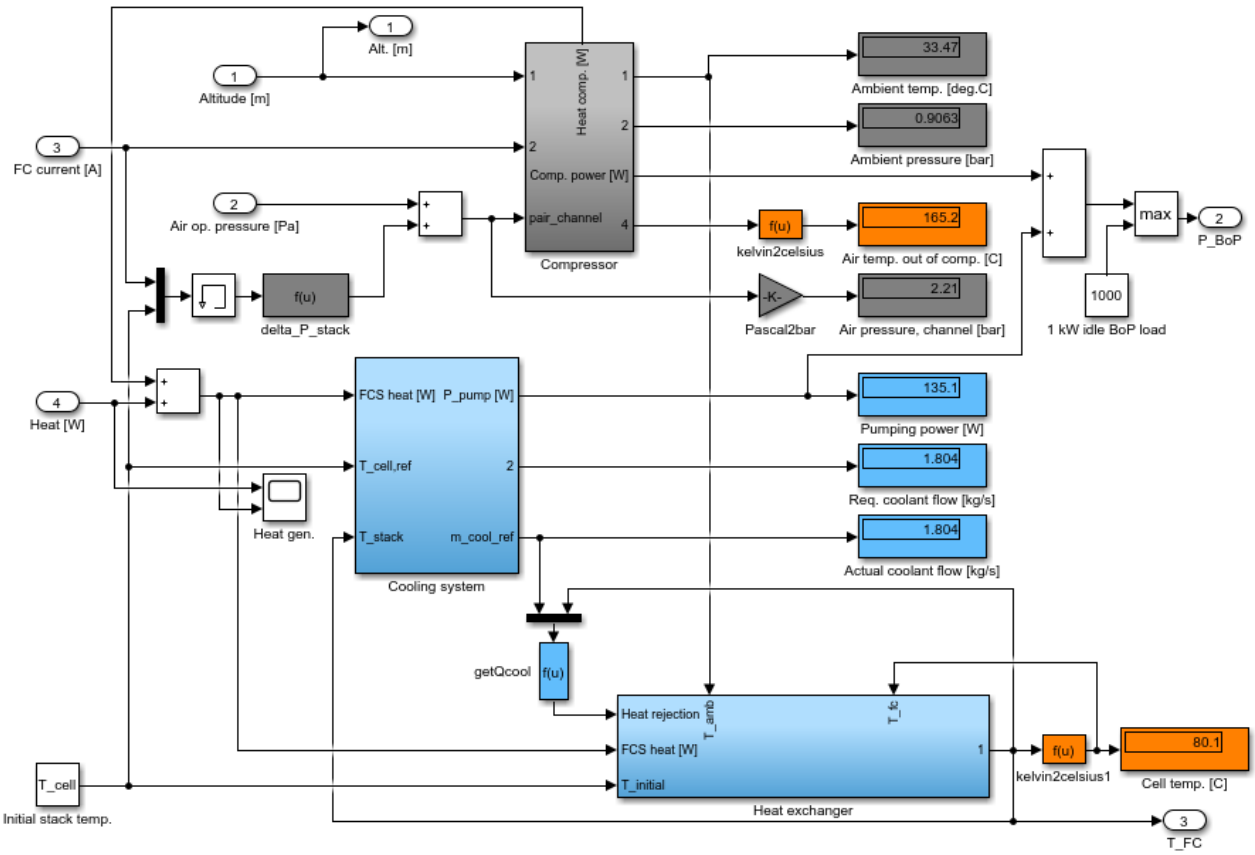

Figure C.3: Balance-of-plant components

Also the heat exchanger (HEX) are included here to dynamically update the FC stack temperature. The HEX block dynamically updates the heat rejection limit based on the temperature difference between the FC stack and the ambient air. Similarly, the cooling system block determines the coolant flow requirement and the corresponding pumping power. Also here, a maximum coolant flow restriction is enforced, limiting the system cooling capability.

The compressor is assumed to ensure a constant operating air pressure. The compressor block dynamically calculates the corresponding power requirement based on the FC current and the ambient air pressure given by the aircraft altitude. A constant air stoichiometry is assumed at all power levels.

The power consumption of the BoP system is drawn from the DC-link in the same way as the propulsive load.

ECSA Losses

By using the dynamically updated temperature and voltage profiles as inputs, the ECSA degradation rate can be determined. This is shown with yellow colors in Fig. C.1. The ECSA losses can be used to estimate the FC lifetime based on the operating conditions.

C.1.2 Boost Converter

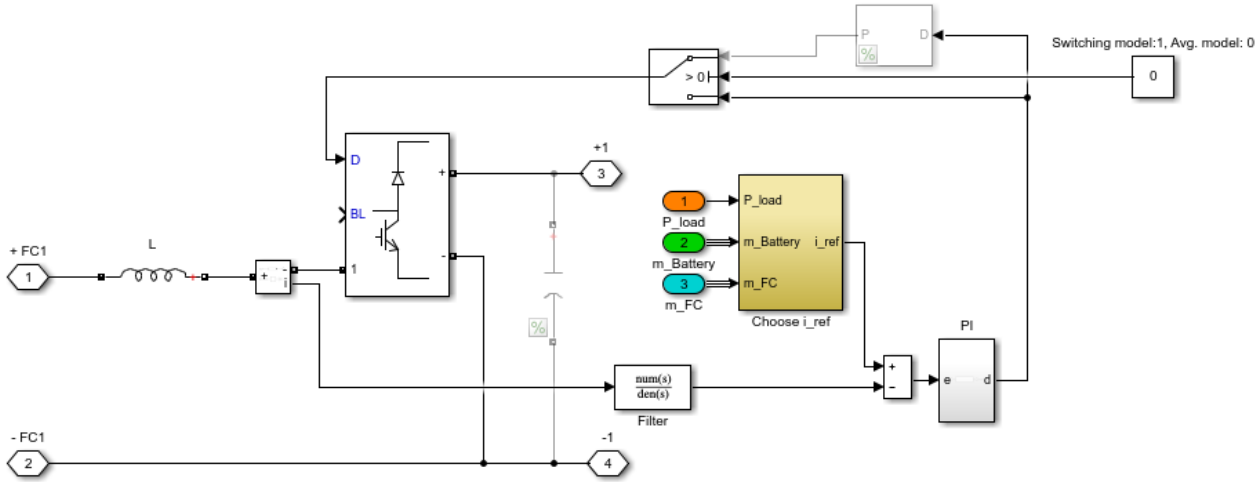

Figure C.4: Boost converter

As the main purpose of the simulation model is to evaluate the power balancing between the power devices, the converter is mainly average-modelled to achieve fast simulations. The converter model can easily be adjusted to switching mode operation with PWM pulses for investigations on smaller time scales. When a battery is attached to the DC-link, the boost converter is operated in current control mode. This means that a current reference is calculated and used to obtain the duty cycle signal. For specific mission profiles, the FC current reference is obtained from the difference between the load power and the pre-calculated battery power share. This approach lacks generality, but is suitable for testing the power balancing between the power devices. For the general case, the SOC control algorithm in [121] is implemented and can be used to adjust the current set-point of the FC. In this way, the FC can be operated at a desirable power level as long as the battery SOC and, thus, the DC-link voltage, are satisfying. The PI regulator used to obtain the FC current reference is relatively slow and the system allows the battery to respond to the fastest power transients. In the case of no hybridization (i.e. no battery), the converter will be voltage controlled (not shown in Fig. C.4) with a much higher crossover frequency, as there is no battery to stabilize the DC-link voltage. A large capacitor is used to maintain the DC-link voltage at a desirable level in this case. This capacitor must account for both the switching behaviour of the FC power supply, as well as the power ramp limitation of the FCS. The control system calculating the FC current reference is shown in Fig. C.5.

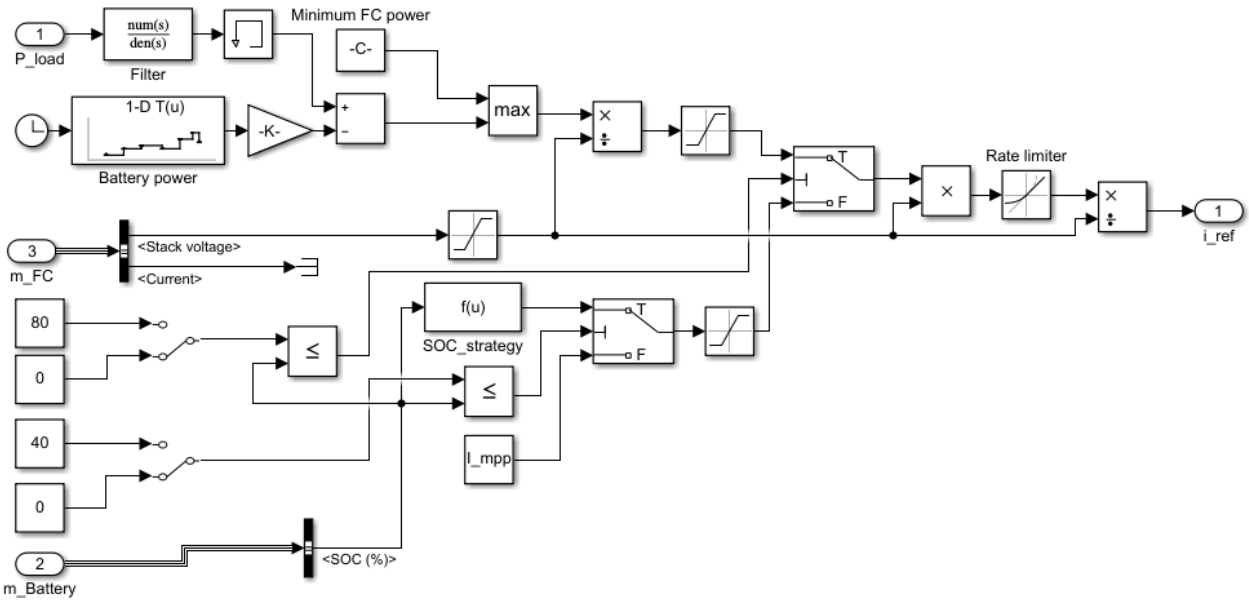

Figure C.5: Current reference system

There FC current reference is saturated by the lower and upper current limits of the FC. The *rate limiter* block ensures that the suggested power ramping limits, both up and down, are not violated.

C.1.3 Battery

The generic Simscape battery model is used for simulations. Parameters are obtained from the reference battery cell datasheet and adjusted with the number of series and parallel cells, as shown in Fig. C.6.

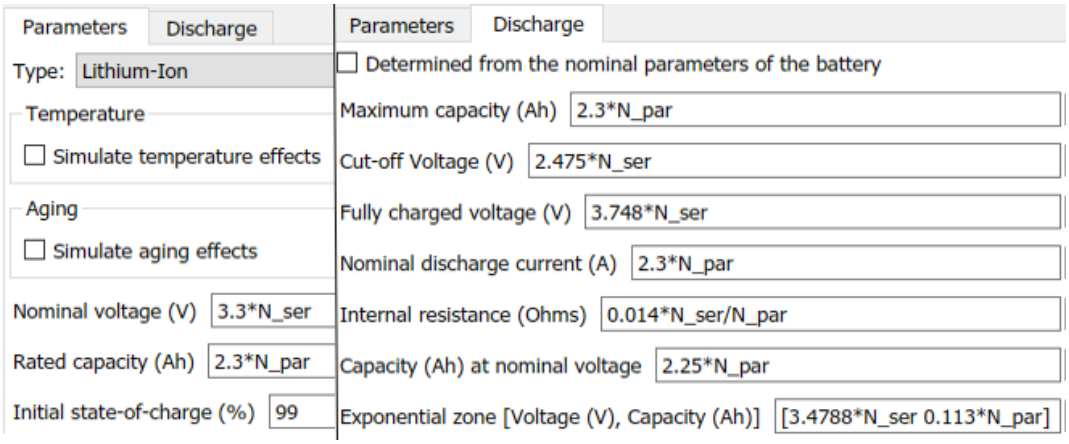

Figure C.6: Boost converter

As the battery is directly shunted to the DC-link, there is no direct control of the battery power output.

C.1.4 Mission Profile

The power, speed and altitude profiles are pre-calculated for each mission profile. The load power is divided by the number of FC stacks put in parallel to simulate the load seen by each stack and battery configuration in the power system. The possibility of ramping of the power before takeoff is also implemented to avoid initial load steps from zero to full power. To test how the system responds to demanding load conditions, some fault and emergencies cases are also implemented, as shown in Fig. C.7.

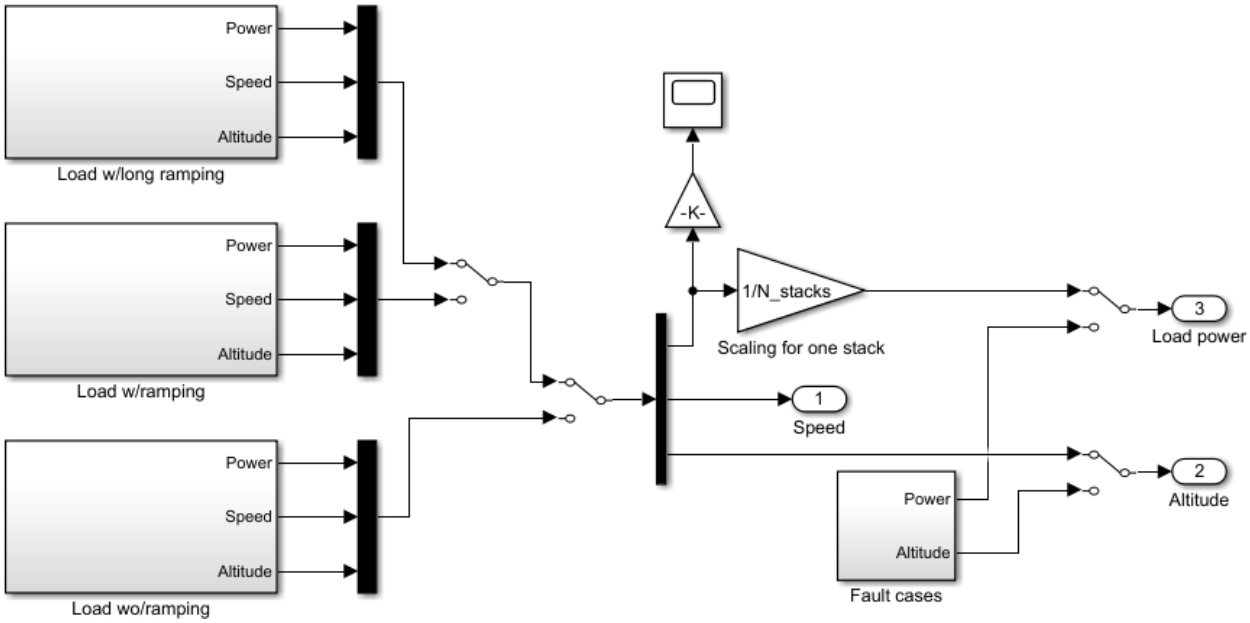

Figure C.7: Load profile

Unless otherwise stated, the time steps of the mission profiles are set to one second.

C.2 Lifetime Calculations

To calculate the estimated operating lifetime of the FC, the ECSA leading to a 10% power output degradation must be found. This can be done by using the FC voltage-current relation presented

in Section 2. The ECSA after T seconds of operation can be calculated as

$$\begin{aligned}(ECSA)_T &= (ECSA)_{T-1} - \frac{(ECSA)_{T-1}\cdot(kT+kU)}{3600}\cdot\Delta t \\ &= (ECSA)_{T-1}\cdot\left(1-\frac{(kT+kU)\Delta t}{3600}\right) \\ &= (ECSA)_{T-2}\cdot\left(1-\frac{(kT+kU)\Delta t}{3600}\right)^2 \\ &= \dots \\ &= (ECSA)_2\cdot\left(1-\frac{(kT+kU)\Delta t}{3600}\right)^{T-2} \\ &= (ECSA)_1\cdot\left(1-\frac{(kT+kU)\Delta t}{3600}\right)^{T-1} \\ &= (ECSA)_0\cdot\left(1-\frac{(kT+kU)\Delta t}{3600}\right)^{T},\end{aligned} \tag{C.1}$$

where Δt has a resolution of 1s. The time to reach the EoL criteria during constant voltage and temperature cycling can be calculated as,

$$T_{EoL} = \frac{ln\left(\frac{(ECSA)_{EoL}}{(ECSA)_{BoL}}\right)}{ln\left(1-\frac{(kT+kU)\Delta t}{3600}\right)} \tag{C.2}$$

where $(ECSA)_{EoL}$ and $(ECSA)_{BoL}$ is the ECSA at end-of-life and beginning-of-life, respectively. In the case where the FC is operated at two different temperatures,

$$T_{EoL} = \frac{ln\left(\frac{(ECSA)_{EoL}}{(ECSA)_{BoL}}\right)}{(1-x)\cdot ln(c_1)+x\cdot ln(c_2))} \tag{C.3}$$

where x is the fraction of time spent at the temperature corresponding to c_2 and

$$c_i = 1-\frac{(kT_i+kU)\Delta t}{3600}.$$

Appendix D

Optimization Results

D.1 Optimization on Constant Power

Table D.1: Weight optimization for different hybridization factors based on the reference mission profile.

Auckland-Woodbourne										
Hybrid. factor	Storage tech.	Opt. current density [A/cm2]	Over-sizing	Tank H2 [kg]	Stack [kg]	Comp. [kg]	Cool. [kg]	HEX [kg]	Est. battery [kg]	Total [kg]
100%	Comp.	1.83	38.1%	1483	1856	1199	1230	1831	0	7598
4.0 MW	Cryo.	1.87	35.6%	1020	1822	1210	1236	1841	0	7130
80%	Comp.	1.79	40.0%	1479	1505	952	980	1701	547	7164
3.2 MW	Cryo.	1.84	37.1%	1018	1474	962	986	1710	547	6697
50%	Comp.	1.70	46.0%	1466	981	583	605	1023	4107	8766
2.0 MW	Cryo.	1.77	41.4%	1011	950	592	611	1032	4107	8302
Opt.: 61%	**Comp.**	**1.75**	**42.8%**	**1473**	**1223**	**752**	**776**	**1502**	**1108**	**6834**
2.55 MW	**Cryo.**	**1.81**	**39.0%**	**1014**	**1191**	**761**	**782**	**1511**	**1108**	**6368**

In all cases, a significant oversizing is optimal. The gain of oversizing increases as the hybridization increases (i.e. more battery power), because the weight of the FC becomes less dominating compared to the tank system.

Table D.2: Optimal hybridization for different mission profiles based on weight.

Flight	**Opt. hybrid.**	Storage tech.	Over-sizing	Tank H2 [kg]	Stack [kg]	Comp. [kg]	Cool. [kg]	HEX [kg]	Est. batt. [kg]	Total [kg]
Medium ~500 km ~80 min	65% 2.6 MW	Comp.	34.9%	1464	1178	372	765	1529	988	**6297**
	65% 2.6 MW	Cryo.	31.1%	1010	1146	380	771	1538	988	**5833**
Long ~1000 km ~150 min	68.5% 2.7 MW	Comp.	40.6%	2172	1276	375	785	1412	1141	**7160**
	68.5% 2.7 MW	Cryo.	35.5%	1523	1229	385	793	1424	1141	**6495**
Short ~200 km ~30 min	70% 2.8 MW	Comp.	27.7%	743	1201	418	837	1501	979	**5680**
	70% 2.8 MW	Cryo.	25.9%	499	1185	423	841	1506	979	**5433**
Standard ~400 km ~60 min	77.5% 3.1 MW	Comp.	33.4%	1541	1390	447	915	1598	653	**6543**
	77.5% 3.1 MW	Cryo.	30.0%	1064	1355	456	922	1608	653	**6057**

The optimal hybridization is independent of the storage technology for all four mission profiles, but oversizing of the FC is more favoured in the case of compressed storage in cylindrical tanks. This is due to the lower weight efficiency of this storage technology compared to cryogenic storage in spherical tanks. For all mission profiles, the optimal hybridization is between 65% and 77.5%.

D.2 Optimization on Mission Profile

D.2.1 FC Only Case

Figure D.1 shows the mass optimization for the long-range flight for the FC only case.

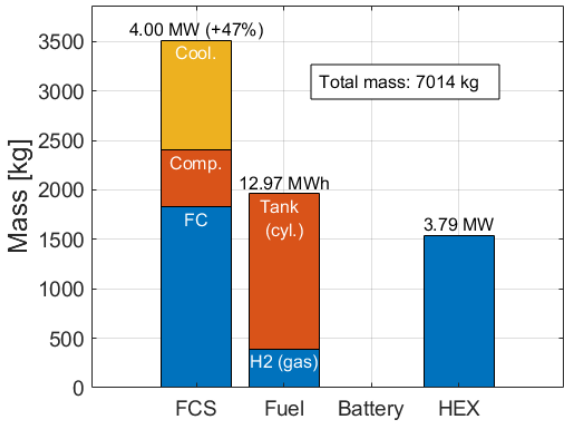

(a) **Compressed storage:** Component mass specification.

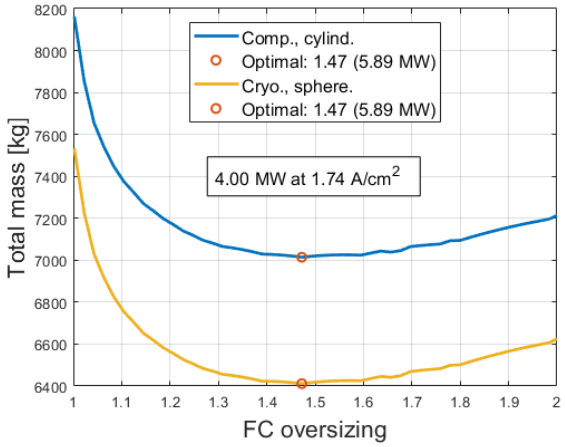

(b) FC size sensitivity.

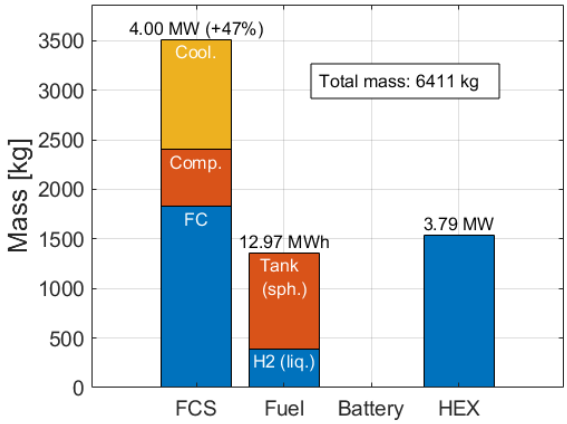

(c) **Cryogenic storage:** Component mass specification.

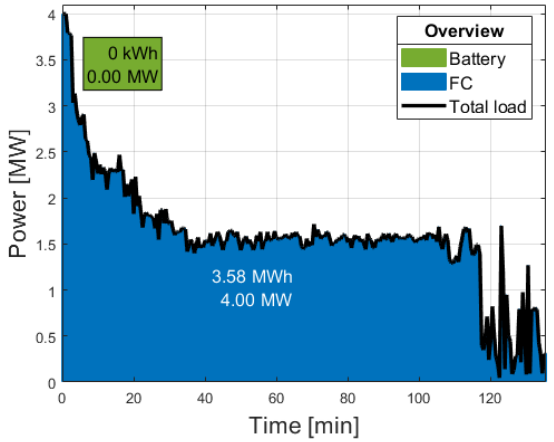

(d) Power sharing.

Figure D.1: Newman-Perth: Optimized hybridization for long-range mission profile.

Figure D.2 shows the mass optimization for the short-range flight for the FC only case.

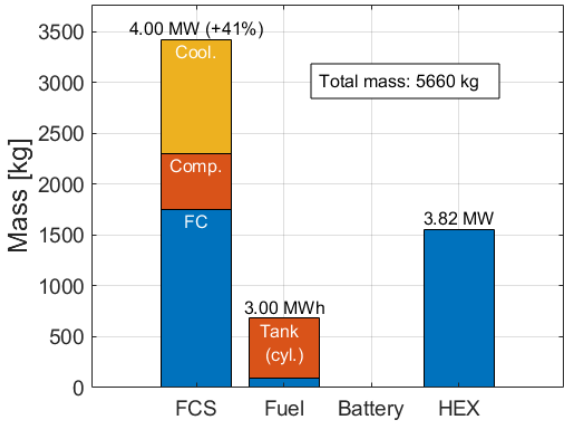

(a) **Compressed storage:** Component mass specification.

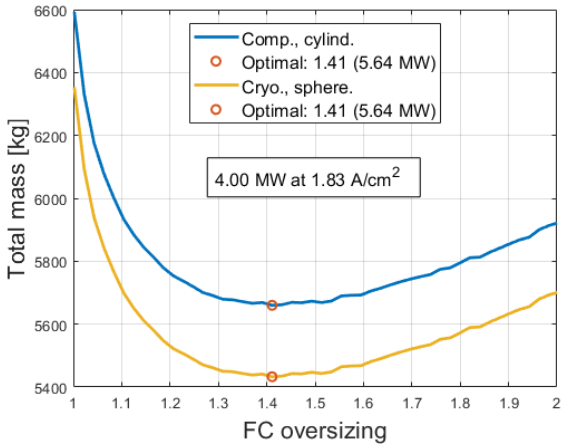

(b) FC size sensitivity.

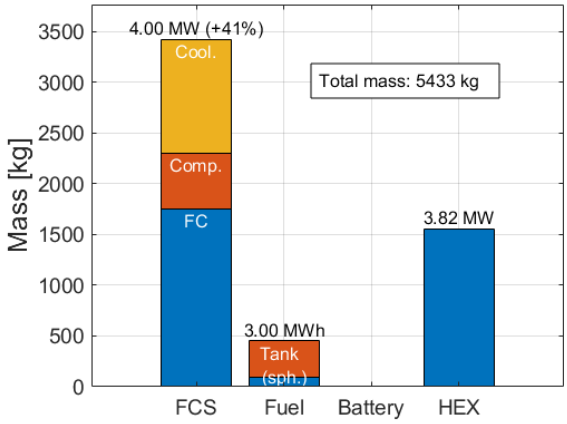

(c) **Cryogenic storage:** Component mass specification.

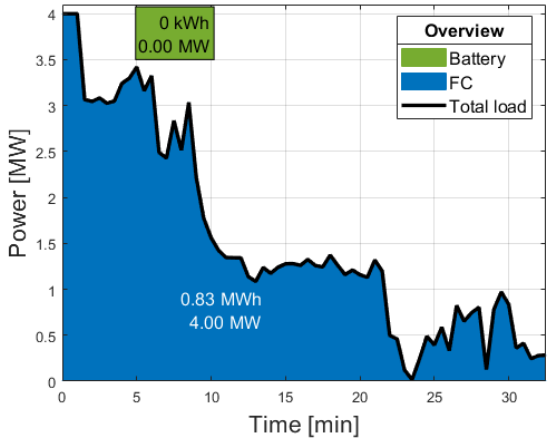

(d) Power sharing.

Figure D.2: Bodø-Evenes: Optimized hybridization for short-range mission profile.

Figure D.3 shows the mass optimization for the standard mission profile for the FC only case.

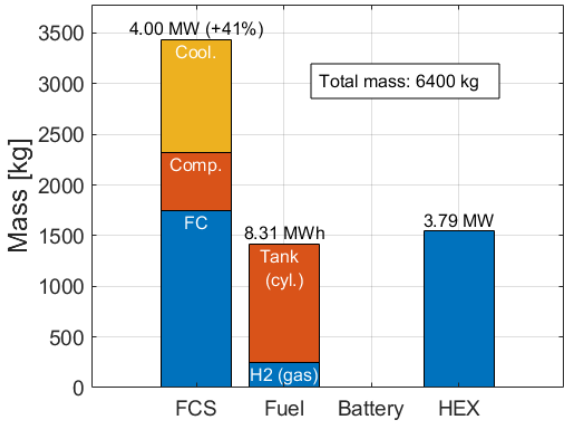

(a) **Compressed storage:** Component mass specification.

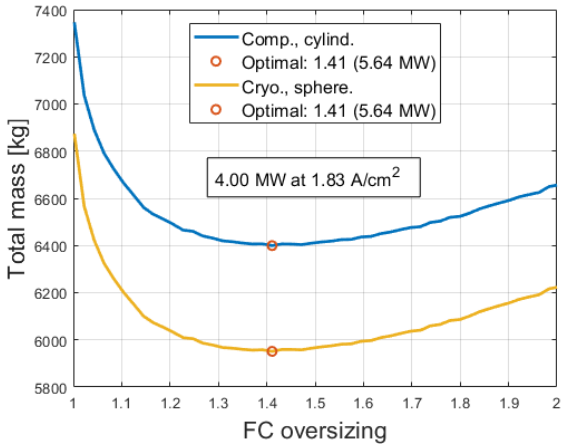

(b) FC size sensitivity.

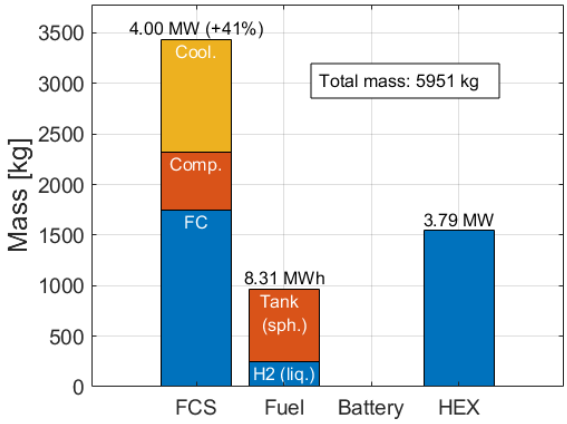

(c) **Cryogenic storage:** Component mass specification.

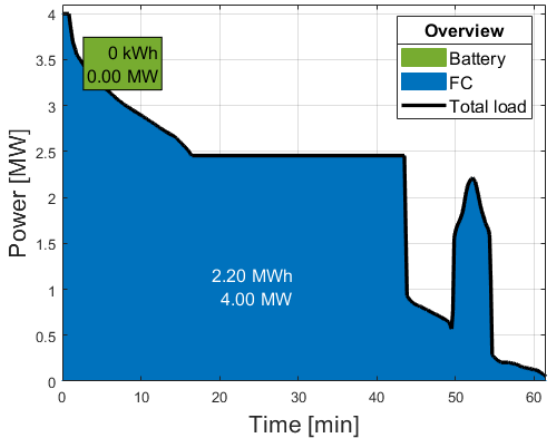

(d) Power sharing.

Figure D.3: Standard profile: Optimized hybridization for standard mission profile.

D.2.2 Hybrid Case

Figure D.4 shows the mass optimization for the long-range flight for the hybrid case.

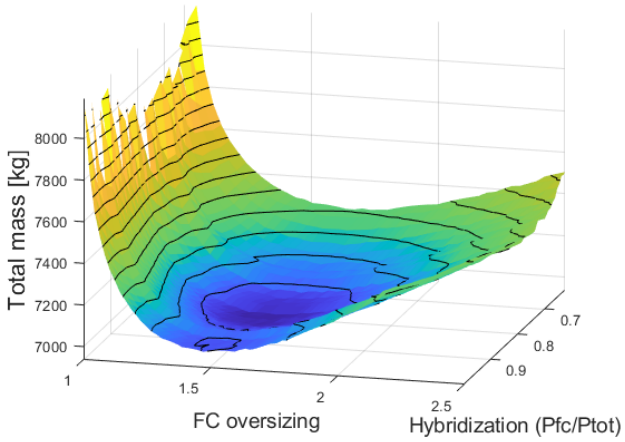

(a) Mass profile.

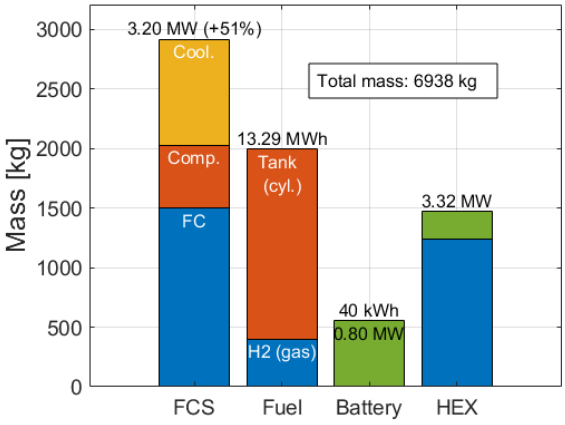

(b) Optimal mass specifications.

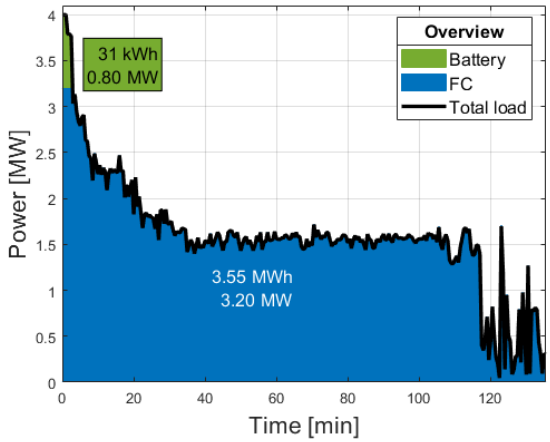

(c) Optimal power sharing.

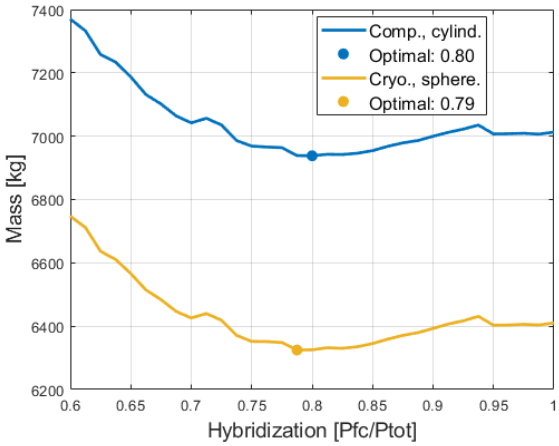

(d) Optimal hybridization.

Figure D.4: Long mission profile: Newman Perth. Compressed storage in cylindrical tanks.

Figure D.5 shows the mass optimization for the short-range flight for the hybrid case.

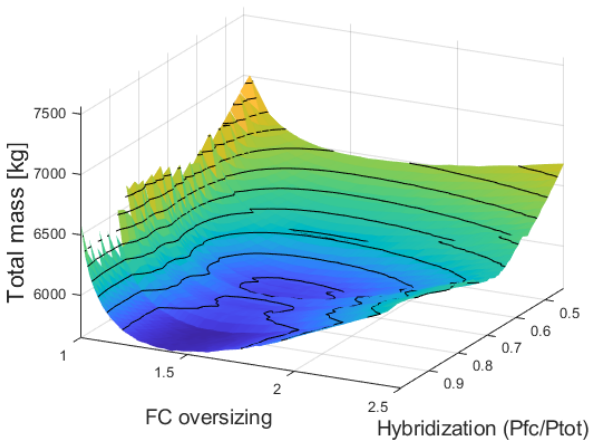

(a) Mass profile.

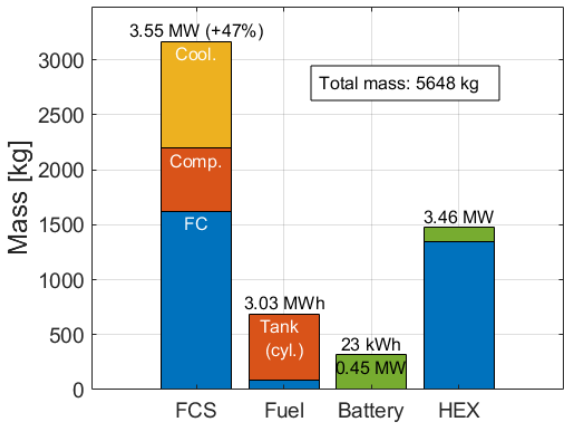

(b) Optimal mass specifications.

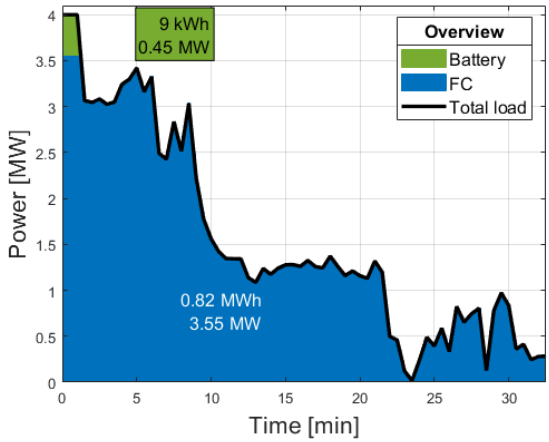

(c) Optimal power sharing.

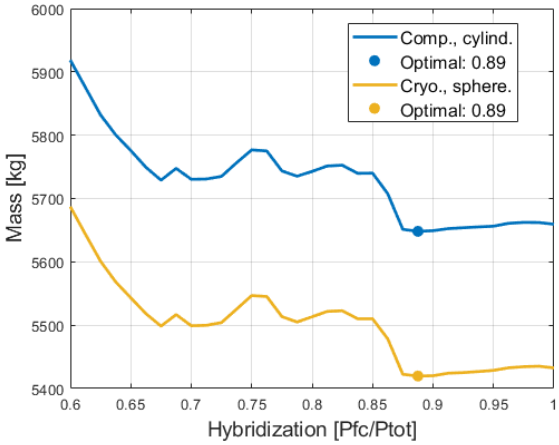

(d) Optimal hybridization.

Figure D.5: Short mission profile: Bodø-Evenes. Compressed storage in cylindrical tanks.

Figure D.6 shows the mass optimization for the standard profile for the hybrid case.

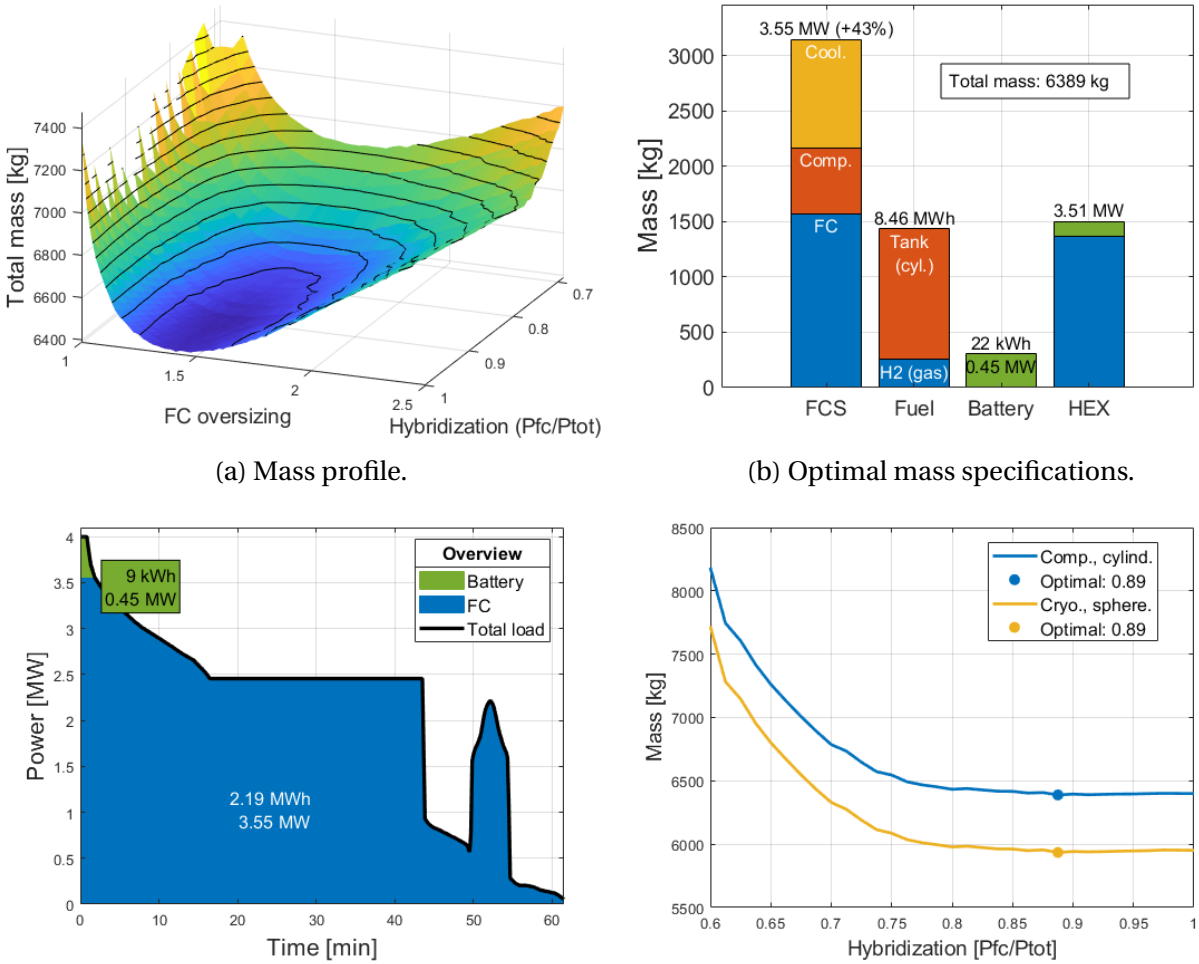

(a) Mass profile.

(b) Optimal mass specifications.

(c) Optimal power sharing.

(d) Optimal hybridization.

Figure D.6: Standard profile. Compressed storage in cylindrical tanks.

D.2.3 Cost per Available Seat Kilometer

Figure D.7 shows the normalized CASK for the short-range flight.

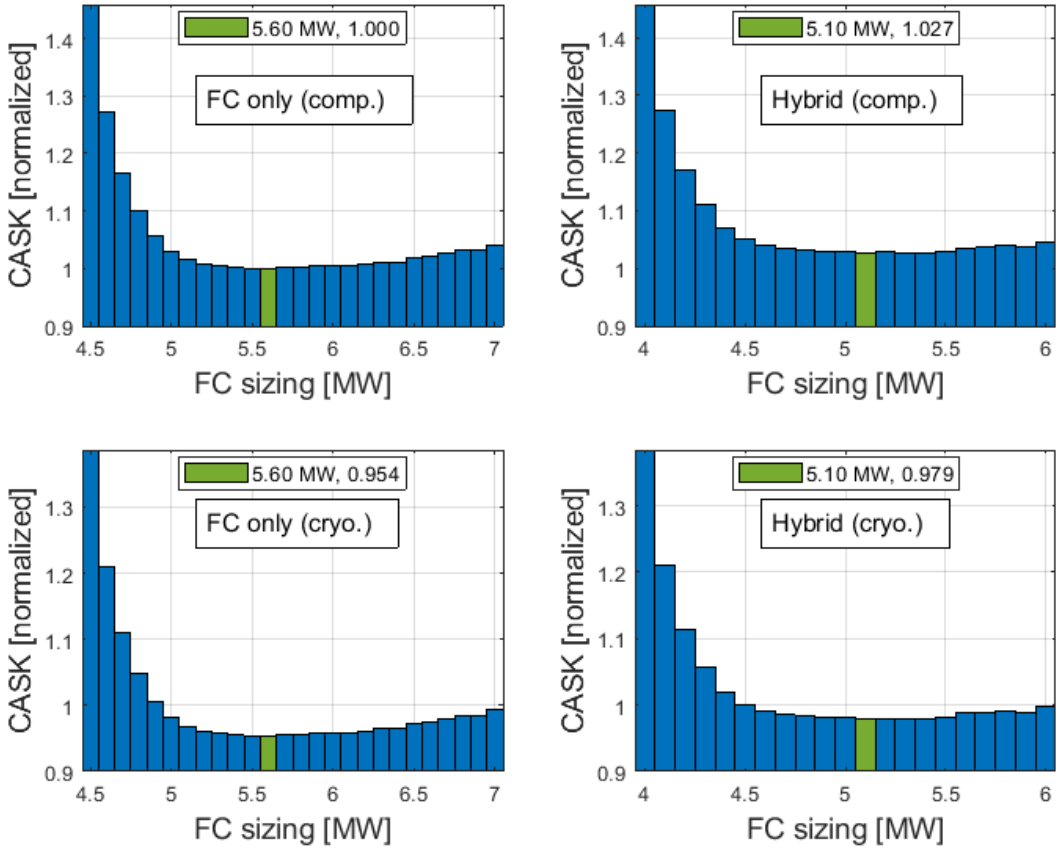

Figure D.7: Short-range mission: Cost per available seat kilometer (CASK) for FC only case and hybrid case with compressed and with cryogenic tanks. CASK normalized to the optimal FC only case with compressed storage.

Figure D.8 shows the normalized CASK for the standard mission profile.

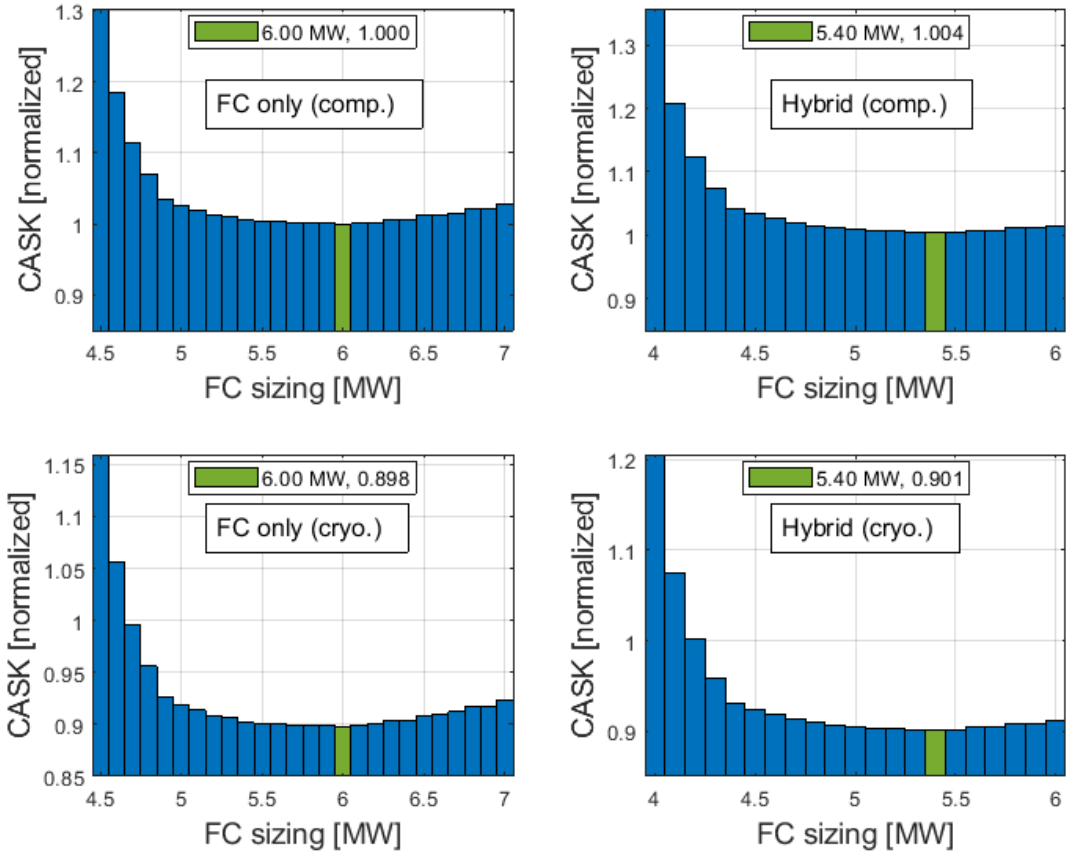

Figure D.8: Standard mission: Cost per available seat kilometer (CASK) for FC only case and hybrid case with compressed and with cryogenic tanks. CASK normalized to the optimal FC only case with compressed storage.

Appendix E

Simulations

E.1 Power Balance Simulations

Figure E.1 shows the mission characteristics for the long-range flight for the optimal hybrid case.

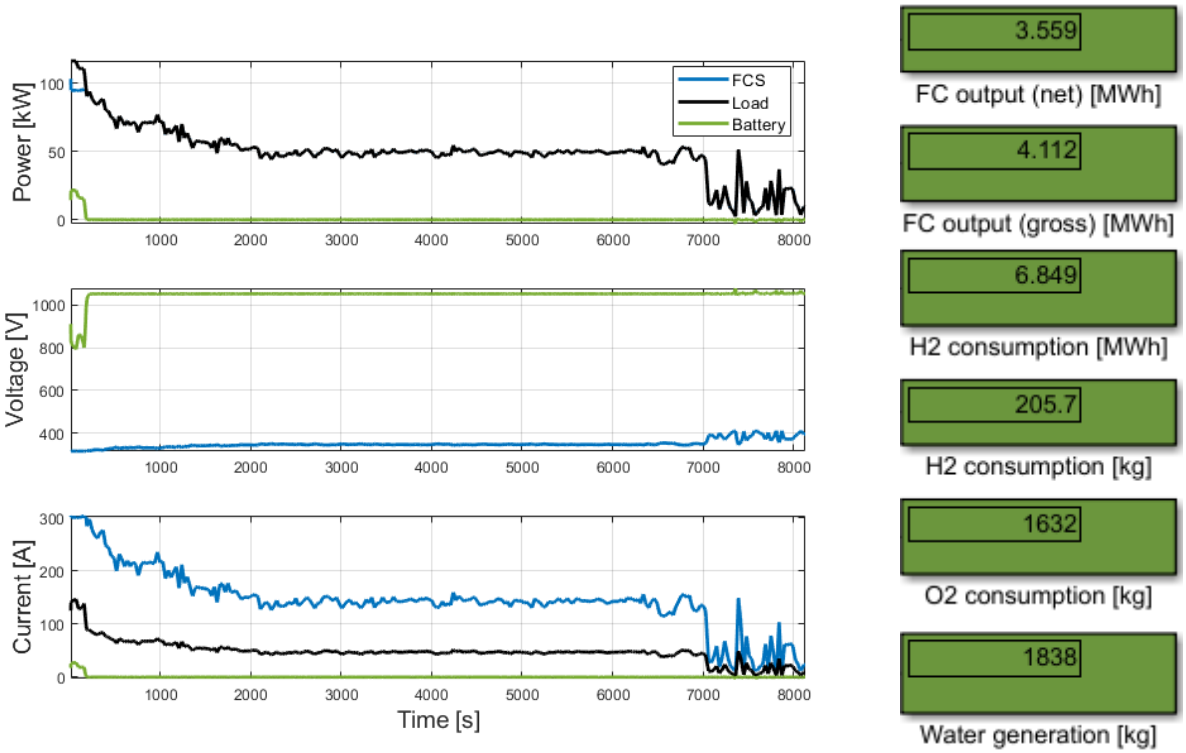

(a) Power sharing between fuel cell system and battery.

(b) Fuel cell energy.

Figure E.1: Mission characteristics for the long-range flight.

Figure E.2 shows the mission characteristics for the short-range flight for the optimal hybrid case.

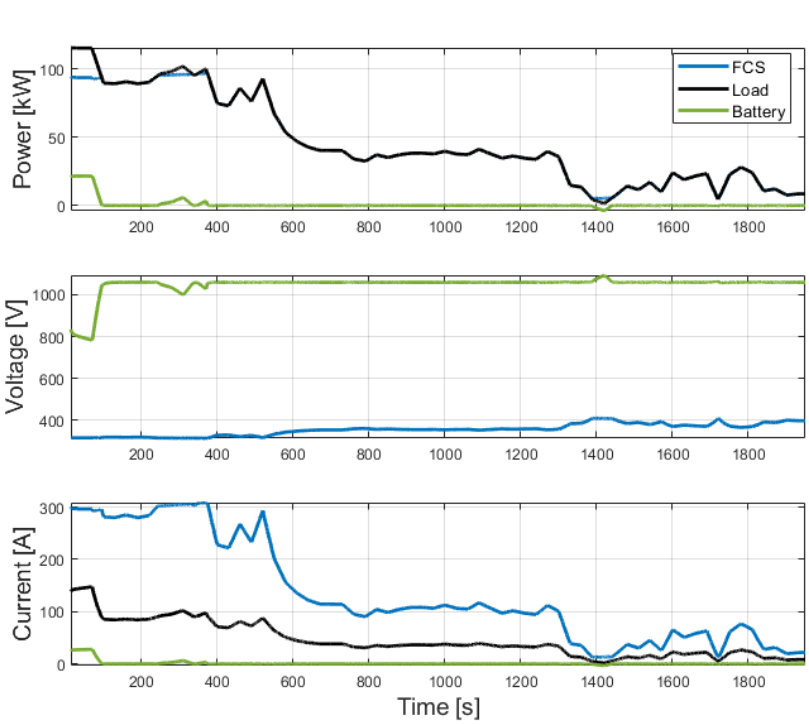

(a) Power sharing between fuel cell system and battery.

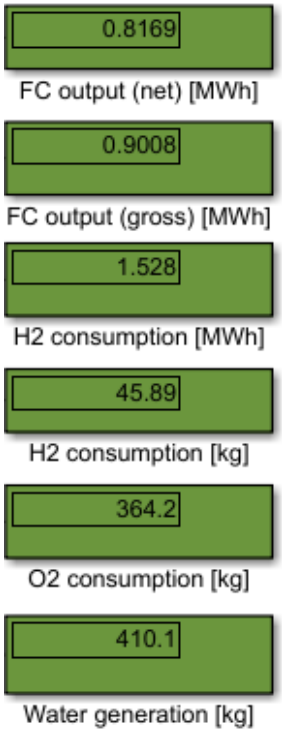

(b) Fuel cell energy.

Figure E.2: Mission characteristics for the short-range flight.

Figure E.3 shows the mission characteristics for the standard mission profile for the optimal hybrid case.

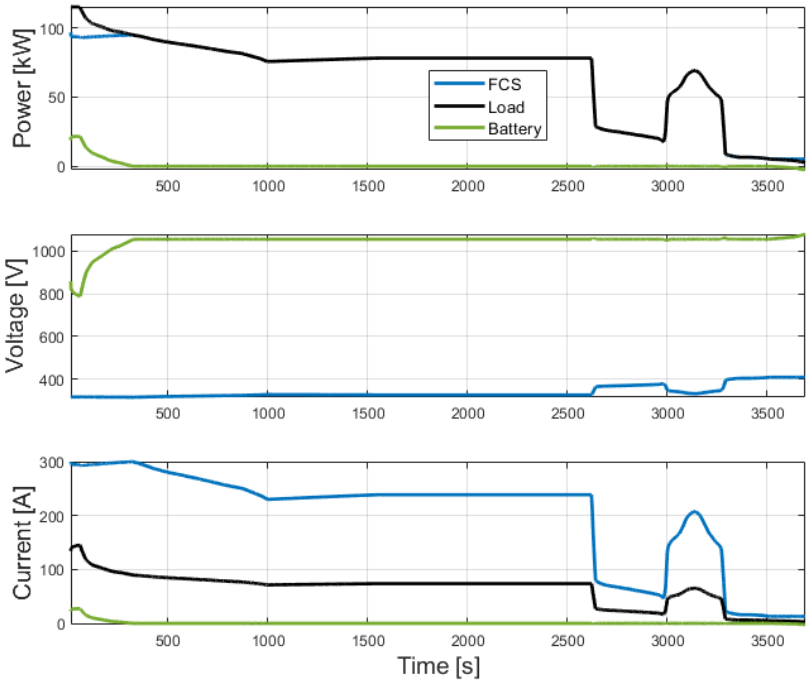

(a) Power sharing between fuel cell system and battery.

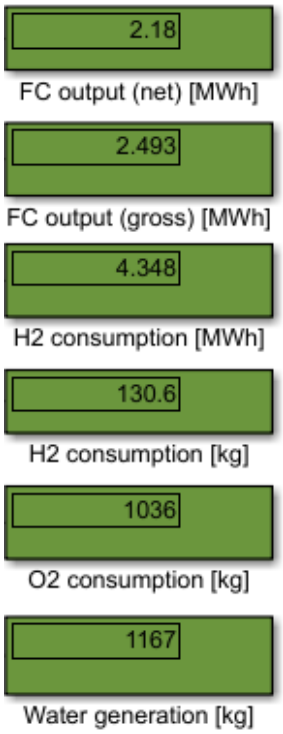

(b) Fuel cell energy.

Figure E.3: Mission characteristics for the standard flight.

Appendix F

Numerical Code

Some of the developed scripts are attached in this Appendix. More code, instructions and explanations can be provided from the author by request.

F.1 Mission Profile Calculation

This script is used to obtain the power, altitude and speed profiles from logging data. The data is averaged at a common sampling rate.

```
function [t_vec_sample, speed_vec_sample, altitude_vec_sample,
    P_vec_sample] = getMission2Simulink_v3(mission_profile, m_aircraft,
    t_sample, plot_or_not)
%% Mission profile
[speed, altitude, time_vec, h_start] = getLoggingData(mission_profile);
if altitude(1) == 0
altitude(1) = h_start; %Airport height above sea level [m]
end
%% Create vectors for Simulink (sample time: t_sample)
SP1                  = timetable(seconds(time_vec)', speed');
SP2                  = retime(SP1,'regular','linear','SampleRate', 1/
    t_sample);
ALT1                 = timetable(seconds(time_vec)', altitude');
ALT2                 = retime(ALT1,'regular','linear','SampleRate', 1/
    t_sample);
t_vec_sample         = seconds(SP2.Time');
speed_vec_sample     = SP2.Variables';
altitude_vec_sample  = ALT2.Variables';
%% Initialize vectors
V_avg_vec            = zeros(1, length(t_vec_sample));
d_v_vec              = zeros(1, length(t_vec_sample));
d_t_vec              = zeros(1, length(t_vec_sample));
d_h_vec              = zeros(1, length(t_vec_sample));
alpha_vec            = 0*pi/180*ones(1, length(t_vec_sample));
```

```
m_vec                   = m_aircraft*ones(1, length(t_vec_sample));
%% Parameters for rho_air calculation
%rho_amb                 = 1.225;              %kg/m^3
M                       = 0.0289654;          %molar mass of dry air [kg/mol]
R                       = 8.31447;            %ideal gas constant [J/(K*mol)]
p_0                     = 101325;             %standard atm. pressure [Pa]
T_0                     = 288.15;             %standard temp. [K]
L                       = 0.0065;             %temperature lapse rate [K/m]
g                       = 9.81;               %m/s^2
%% Q300 parameters
A_wing                  = 56.20;
A_ratio                 = 13.36;
e                       = 0.85;
C_D0                    = 0.02;
A_prop                  = pi*(3.96/2)^2*2;
%% Functions
rho_air = @(h) p_0*M/(R*T_0)*(1-L.*h/T_0).^(g*M/(R*L)-1);
C_lift  = @(m,gamma, h, V) m.*g.*cos(gamma)./(0.5.*rho_air(h).*V.^2.*
    A_wing);
C_drag  = @(m,gamma, h, V) C_D0 + C_lift(m, gamma, h, V).^2./(pi.*
    A_ratio.*e);
Gx      = @(m,gamma) m*g.*sin(gamma);
Fd      = @(m,gamma, h, V) 0.5.*rho_air(h).*V.^2.*C_drag(m, gamma, h, V)
    .*A_wing;
FL      = @(m,gamma, h, V) 0.5.*rho_air(h).*V.^2.*C_lift(m, gamma, h, V)
    *A_wing;
sum_Fx  = @(m,a) m.*a;
Thrust  = @(m,gamma,h,V,a,alpha) (Gx(m, gamma)+Fd(m,gamma,h,V)+sum_Fx(m,
    a))./cos(alpha);
c_T     = @(T,h,V) T./(0.5.*rho_air(h).*V.^2*A_prop);
eta_F   = @(T,h,V) 2./(1+sqrt(1+c_T(T,h,V)));
Power   = @(T,h,V) abs(T).*V./eta_F(T,h,V);
%% Create relevant vectors
for it = 1:length(t_vec_sample)-1
    V_avg_vec(it)    = (speed_vec_sample(it)+speed_vec_sample(it+1))/2;
    d_v_vec(it)      = speed_vec_sample(it+1) - speed_vec_sample(it);
    d_t_vec(it)      = t_vec_sample(it+1) - t_vec_sample(it);
    d_h_vec(it)      = altitude_vec_sample(it+1) - altitude_vec_sample(
        it);
    m_vec(it)        = m_vec(it)-(2e6/33.3e3/0.5)/length(t_vec_sample)*
        it;
end
%% Set last vector element equal to second last element
V_avg_vec(end)       = V_avg_vec(end-1);
d_v_vec(end)         = d_v_vec(end-1);
d_t_vec(end)         = d_t_vec(end-1);
d_h_vec(end)         = d_h_vec(end-1);
```

```
m_vec(end)            = m_vec(end-1);
%% Calculate power
gamma_vec     = asin(d_h_vec./(V_avg_vec.*d_t_vec));
a_vec         = d_v_vec./d_t_vec;
T_vec         = Thrust(m_vec, gamma_vec, altitude_vec_sample, V_avg_vec,
   a_vec, alpha_vec);
P_vec_sample = Power(T_vec, altitude_vec_sample, V_avg_vec);

%% Constructing takeoff phase
P_takeoff             = 3.6e6;
t_takeoff             = 60; %[s]
n_steps               = ceil(t_takeoff/t_sample);
if t_takeoff <= t_sample
    t_vec_sample      = [0 t_takeoff t_vec_sample+t_takeoff+t_sample];
else
t_vec_sample          = [0:t_sample:t_takeoff t_vec_sample+t_takeoff+
   t_sample];
end
speed_0               = 0; %[m/s]
inc_speed             = (speed_vec_sample(1)-speed_0)/(n_steps+1);
speed_vec_sample      = [speed_0:inc_speed:(speed_vec_sample(1)-inc_speed
   ) speed_vec_sample];
altitude_vec_sample   = [altitude_vec_sample(1)*ones(1, n_steps+1)
   altitude_vec_sample(1)+(altitude_vec_sample(2)-altitude_vec_sample
   (1))/2 altitude_vec_sample(2:end)];
P_vec_sample          = [P_takeoff*ones(1, n_steps+1) P_vec_sample];
end
```

F.2 Optimization Scripts

Costs Script

This script calculate the costs of the power devices based on the sizing obtained from the scripts below. The script estimates the FC lifetime based on the FC sizing and the relevant mission profile.

```
tot_inv_opt = inf;
%% Test different FC sizings;
P_size_fc_vec_vec = 3.2e6;
for it_size = 1:length(P_size_fc_vec_vec)
P_size_fc_vec     = P_size_fc_vec_vec(it_size);
p_step            = 0.1e6;
P_high_vec        = [P_size_fc_vec+1.8e6:0.05e6:P_size_fc_vec+2.1e6];
cell_step         = 275;
L_Pt_vec = [0.6:-0.1:0.3];
for it_Pt = 1:length(L_Pt_vec)
```

```
L_Pt = L_Pt_vec(it_Pt);
for iter = 1:length(P_high_vec)
   P_high            = P_high_vec(iter);
   P_low             = 0;
optimization_on_mission();
E_fuel_consump_vec(iter) = E_rq_h2_opt+E_batt_Wh_used;
E_fuel_tank_vec(iter)    = E_h2_tank_opt;
opt_weight_vec(iter)     =  opt_weight;

fc_scale     = 1;
N_cells_tot  = N_cells_opt*fc_scale;
N_cells      = 455;
N_stacks_tot = N_cells_tot/N_cells;
P_load_stack = P_load_fc/N_stacks_tot;
P_cell_prof  = P_load_stack/N_cells;
m_fcs_hex    = m_fcs_hex_opt/(N_cells_opt/N_cells);
%% Get all relevant parameters
init_parameters();
%% For ECSA loss calculations
kT0               = 5e-5;
kU0               = 1e-5;
EaT               = 28600;
%% Get BoL vectors
ECSA                   = 50;
[~, P_cell_net_vec, ~] = getVectors_v3(0, 0, 0);
P_cell_net_nominal_BOL_check = P_cell_net_vec(nominal_index);
P_cell_net_nominal_BOL = max(P_load_fc)/N_cells_opt;
P_cell_net_max_BOL     = P_cell_net_nominal_BOL*oversize_factor;

%%
dt                  = t_vec_sample(2)-t_vec_sample(1);
yearly_flights      = 365*6;
step_n              = 6*7/2;
N_flights_vec       = [1:step_n:10000];
ECSA_vec            = [ECSA, NaN*ones(1, length(N_flights_vec)-1)];
for it0 = 1:length(N_flights_vec)
%% Check end-of-life criteria
if P_cell_net_vec(nominal_index) < 0.9*P_cell_net_nominal_BOL
    L = N_flights_vec(it0)/yearly_flights;
    break;
elseif max(P_cell_net_vec) < max(P_cell_prof)
    L = N_flights_vec(it0)/yearly_flights;
    break;
elseif max(T_stack_prof_wc)>(273+95)
    L = N_flights_vec(it0)/yearly_flights;
    break;
end
```

```
%% Update vectors
V_cell_vec              = getV_cell(T_cell, pair, j_0_vec/A_cell, ECSA,
    R_eq, R_Pt); %update voltage curve based on ECSA
V_cell_vec              = real(V_cell_vec(abs(imag(V_cell_vec)) < 0.00001))
    ;          %Adjust for complex numbers (only consider real part of
    vectors)
j_0_vec                 = j_0_vec(1:length(V_cell_vec));
P_cell_vec              = V_cell_vec.*j_0_vec;

for it_1 = 1:length(t_vec_sample)
    if abs(altitude_vec_sample(it_1)-h_flight)>250 || it_1 == 1
h_flight                = altitude_vec_sample(it_1);
P_cell_comp_vec         = P_comp(j_0_vec, I_max, 1, h_flight, ECSA, pair,
    R_eq, R_Pt);
P_cell_exp_vec          = P_exp(T_cell, j_0_vec, 1, h_flight, pair);
P_cell_pump_vec         = Pc_pump(T_cell, pair, j_0_vec/A_cell, ECSA, R_eq,
    R_Pt, j_0_vec, I_max, h_flight, 1, d_Tc);
P_cell_aux_vec          = max(P_cell_comp_vec - P_cell_exp_vec, 1000/455) +
    P_cell_pump_vec;
P_cell_net_vec          = max(P_cell_vec-P_cell_aux_vec,1e-3);
[~, Pmax_indx]          = max(P_cell_net_vec);
eff_stack_vec           = V_cell_vec/V_LHV;
eff_fcs_vec             = eff_stack_vec.*P_cell_net_vec./P_cell_vec;
    end
[~, indx]               = min(abs(P_cell_net_vec(1:Pmax_indx)-P_cell_prof(
    it_1))); %Make sure to avoid operation beyond MPP!
V_cell_prof(it_1)       = V_cell_vec(indx);
i_fc_prof(it_1)         = j_0_vec(indx);
P_fc_prof(it_1)         = P_cell_net_vec(indx)*N_cells;
eff_prof(it_1)          = eff_fcs_vec(indx);
Q_fcs_prof(it_1)        = Q_fcs(T_cell, pair, i_fc_prof(it_1)/A_cell, ECSA,
    R_eq, R_Pt, i_fc_prof(it_1), I_max, h_flight, N_cells);
hex_limit_wc            = (m_fcs_hex*(T_stack_prof_wc(it_1)-T_amb(h_flight)
    )/(80-40)-1.504)*1000/0.407;
hex_limit               = (m_fcs_hex*(T_stack_prof_wc(it_1)-(T_amb(h_flight
    )-25))/(80-40)-1.504)*1000/0.407;
cool_limit_wc           = min(Q_cool_max, hex_limit_wc);
cool_limit              = min(Q_cool_max, hex_limit);
Q_cool_ref_wc           = Q_fcs_prof(it_1)*(T_stack_prof_wc(it_1)<T_cell)+
    cool_limit*(T_stack_prof_wc(it_1)>T_cell);
Q_cool_ref              = Q_fcs_prof(it_1)*(T_stack_prof(it_1)<T_cell)+
    cool_limit*(T_stack_prof(it_1)>T_cell);
Q_rej_wc(it_1)          = min(Q_cool_ref_wc, cool_limit_wc);
Q_rej(it_1)             = min(Q_cool_ref, cool_limit);
if it_1 < length(P_cell_prof)
T_stack_prof_wc(it_1+1) = T_stack_prof_wc(it_1)+(Q_fcs_prof(it_1)-
    Q_rej_wc(it_1))/m_stack/cp_fc*dt;
```

```
T_stack_prof(it_1+1)     = T_stack_prof(it_1)+(Q_fcs_prof(it_1)-Q_rej(
    it_1))/m_stack/cp_fc*dt;
end
end
%% ECSA calculation
kU_vec           = kU0*exp(-0.5*2*F/R./T_stack_prof_wc.*(0.98-V_cell_prof
    ));
kT_vec           = kT0*exp(-EaT/R*(1./T_stack_prof_wc-1/298));
ECSAdot_vec      = (kU_vec+kT_vec)*ECSA/3600;
ECSA             = ECSA - sum(ECSAdot_vec*dt)*step_n;
if it0 < length(N_flights_vec)
ECSA_vec(it0+1) = ECSA;
end
end
%% Cost of fuel cell
K_watt           = interp1(Pt_loading, K_vector, L_Pt);
K_fc_vec(iter)    = K_watt*(P_cell_net_max_BOL*N_cells_tot);
%% Cost of battery:
K_cell = 5.14;
K_pack = K_cell/102*137;
if m_batt_opt ~= 0
    K_batt_vec(iter) = K_pack*(N_ser*N_par);
elseif m_batt_opt == 0
    K_batt = 0;
end
%% Calculate total cost (investment and re-investments)
r                = 0.04;
T                = 15;
L_batt           = 1000/yearly_flights;
tot_inv_batt     = getInvestment(K_batt_vec(iter), r, T, L_batt);
tot_inv_fc(iter) = getInvestment(K_fc_vec(iter), r, T, L);
tot_inv(iter)    = tot_inv_fc(iter) + tot_inv_batt;
lifetime_vec(iter) = N_flights_vec(it0)*t_vec_sample(end)/3600;
%% Fuel and tank costs
w_h2               = 33.3*10^3; %Specific energy of hydrogen [Wh/kg]
K_h2               = 6;         %$/kg (FCH 2 JU target)
K_tank             = 500;       %$/kg (FCH 2 JU target)
K_tank_vec(iter)   = K_tank*E_fuel_tank_vec(iter)/w_h2;
K_h2_vec(iter)     = K_h2*E_fuel_consump_vec(iter)/w_h2;
tot_inv_tank(iter) = getInvestment(K_tank_vec(iter), r, T, T);
tot_inv_fuel(iter) = getInvestment(K_h2_vec(iter), r, T, 1/
    yearly_flights);
end
end
if min(tot_inv) < tot_inv_opt
tot_inv_opt = min(tot_inv);
P_fc_share_opt = P_size_fc_vec;
```

```
end
end
```

Fuel Cell Sizing Script

This scripts iterates through different FC sizings to find the optimality in terms of FCS and storage mass.

```
function [m_fcs_comps, Q_fcs_max, oversize_factor, tot_fcs_mass_vec,
    P_range] = get_FCS_mass_slow(t_vec_sample, P_load_fc_sample,
    altitude_vec_sample, P_fc_size, geometry, type, P_low, P_high,
    cell_step, plot_or_not)
V_LHV              = 1.253;                        %LHV
A_cell             = 180;                          %[cm^2]
j_0_vec            = [1:1:4.0*A_cell];             %[A]
%% FC parameters
T_cell      = 273.15+80;                  %Cell/stack temp. [K]
pamb        = 101325;                     %Ambient pressure [Pa]
pair        = pamb+1.0e5;                 %Pressure of air at cathode [Pa]
i_0_s_ref   = 18.6e-7;                    %Spec. exch. current density [A/
    cm2]
a_c         = 0.495+2.3e-3*(T_cell-300); %Cathodic charge transfer coeff.
i_x         = 5e-3;                       %H2 crossover current density [A
    /cm2]
L_Pt        = 0.40;                       %Pt loading [mgPt/cm2]
ECSA        = 50;                         %ECSA [m2/gPt]
gamma       = 0.54;                       %Kinetic reaction order of ORR
R           = 8.314;                      %[J/(mol*K)]
F           = 96485.33;                   %Faraday's constant [C/mol]
pref        = 101325;                     %Atmospheric pressure (def.) [Pa
    ]
pH2_g       = 0.2e5;                      %Partial pressure H2 diff. [Pa]
%% Fitting ohmic resistance
R_ohm       = 0.018;                      %Estimated/fitted [Ohm*cm2]
%% Transport resistance
[R_eq, R_Pt]   = get_R_transport_interp(pair); %Pressure-dependent R_T
    values
R_T            = @(ECSA, R_eq, R_Pt) 200/103.5638*(R_eq+R_Pt./(ECSA.*L_Pt
    *10)); %[s/m]
%% Adjust exchange current density (based on pressure and temperature)
Tref        = 353.15;
Ec_rev      = 67e3;
i_0_s       = @(pO2, T_cell) i_0_s_ref*(pO2/pref)^gamma*exp(-Ec_rev/(R*
    T_cell)*(1-T_cell/Tref));

%% Other parameters
Th0                = 273+15;              %Ambient temp. at sea-level [K]
```

```
Ph0                 = 101325;               %Ambient pressure at sea-level [
    Pa]
L_T                 = -0.0065;              %[K/m]
g                   = 9.81;                 %[m/s^2]
R_spec              = 287.058;              %[J/(kg*K)] (for dry air)
eta_min             = 0.75*0.9;             %Compressor+motor efficiency
eta_max             = 0.75*0.9;             %Compressor+motor efficiency
eta_exp             = 0.8;                  %Expander efficiency
lambda_O2           = 2.0;                  %Air excess ratio
lambda_H2           = 1.0;                  %Hydrogen excess ratio (~1.0)
m_Mair              = 28.97/1000;           %[kg/mol]
cp_air              = 1000;                 %[J/(kg*K)]
k                   = 1.4;                  %Ratio of specific heats
eta_pump            = 0.58;
rho_cool            = 1036;                 %50/50 WEG (Kabza) [kg/m3]
cp_cool             = 3530;                 %50/50 WEG (Kabza) [J/(kg*K)]
d_Tc                = 10;                   %Coolant temp. difference [K]
%% Functions
%Ambient temp. and pressure
T_amb               = @(h) Th0 + L_T.*h;
p_amb               = @(h) Ph0.*(T_amb(h)./Th0).^(-g/(L_T*R_spec));
%Mass flow rate
M_O2dot             = @(I, N_cells) N_cells*I/(4*F);
m_airdot            = @(I, N_cells) M_O2dot(I, N_cells)*m_Mair*lambda_O2
    /0.21;
%Pressure in stack
delta_p_stack       = @(j_0, ECSA, R_eq, R_Pt) R.*T_cell./(4.*F).*R_T(ECSA
    , R_eq, R_Pt).*j_0.*100^2;
p_air_ch            = @(j_0, ECSA, p_air, R_eq, R_Pt) p_air+delta_p_stack(
    j_0, ECSA, R_eq, R_Pt);
%Compressor and expander:
P_comp              = @(I, I_max, N_cells, h, ECSA, p_air, R_eq, R_Pt)
    m_airdot(I, N_cells).*cp_air.*T_amb(h)./eta_max.*((p_air_ch(I./
    A_cell, ECSA, p_air, R_eq, R_Pt)./p_amb(h)).^(1-1/k)-1);
Q_comp              = @(I, I_max, N_cells, h, ECSA, p_air, R_eq, R_Pt)
    P_comp(I, I_max, N_cells, h, ECSA, p_air, R_eq, R_Pt).*(1-eta_max);
P_exp               = @(T_cell, I, N_cells, h, p_air) m_airdot(I, N_cells)
    .*cp_air.*T_cell.*(1-(p_amb(h)./(p_air)).^(1-1/k))*eta_exp;
Q_exp               = @(T_cell, I, N_cells, h, p_air) P_exp(T_cell, I,
    N_cells, h, p_air)/eta_exp*(1-eta_exp);

%% Voltage loss functions
E                   = @(T_cell, p_air) 1.229 - 0.85e-3*(T_cell-298.15)+2*R
    *T_cell/(4*F)*(log((p_air+pH2_g)/pref)+0.5*log(0.21*p_air/pref));
                                                                %OCV
n_ORR               = @(T_cell, j_0, ECSA, p_air) R.*T_cell./(a_c.*F).*log
    ((j_0+i_x)./(i_0_s(0.21*p_air, T_cell)*L_Pt*ECSA*10));
```

```
    %Act. loss
deltaU_O2           = @(T_cell, j_0, ECSA, R_eq, R_Pt, p_air) R*T_cell/F
    *(1/4+gamma/a_c)*log((0.21*p_air_ch(j_0, ECSA, p_air, R_eq, R_Pt)
    ./100^2-R*T_cell./(4*F)*R_T(ECSA, R_eq, R_Pt).*j_0)./(0.21*p_air_ch(
    j_0, ECSA, p_air, R_eq, R_Pt)./100^2)); %Con. loss
V_ohm               = @(j_0) R_ohm.*j_0;

    %Ohmic losses
getV_cell           = @(T_cell, p_air, j_0, ECSA, R_eq, R_Pt) E(T_cell,
    p_air) - n_ORR(T_cell, j_0, ECSA, p_air) + deltaU_O2(T_cell, j_0,
    ECSA, R_eq, R_Pt, p_air) - V_ohm(j_0);
                                    %Combined
%% Power, heat and cooling functions
%Electric power
P_el                = @(T_cell, p_air, j_0, ECSA, R_eq, R_Pt, I, N_cells)
    getV_cell(T_cell, p_air, j_0, ECSA, R_eq, R_Pt).*I.*N_cells;
%Heat power FC
Q_fc                = @(T_cell, p_air, j_0, ECSA, R_eq, R_Pt, I, N_cells)
    (V_LHV-getV_cell(T_cell, p_air, j_0, ECSA, R_eq, R_Pt)).*I.*N_cells;
%Heat power FCS (neglecting the heat from the cooling system pumps)
Q_fcs               = @(T_cell, p_air, j_0, ECSA, R_eq, R_Pt, I, I_max, h,
     N_cells) Q_fc(T_cell, p_air, j_0, ECSA, R_eq, R_Pt, I, N_cells) +
    Q_comp(I, I_max, N_cells, h, ECSA, p_air, R_eq, R_Pt) + Q_exp(T_cell
    , I, N_cells, h, p_air);
%Mass flow coolant [kg/s]
m_cooldot           = @(T_cell, p_air, j_0, ECSA, R_eq, R_Pt, I, I_max, h,
     N_cells, d_Tc) Q_fcs(T_cell, p_air, j_0, ECSA, R_eq, R_Pt, I, I_max
    , h, N_cells)./(cp_cool*d_Tc);
%Pressure drop cooling circuit [Pa]
delta_p_cool        = @(T_cell, p_air, j_0, ECSA, R_eq, R_Pt, I, I_max, h,
     N_cells, d_Tc) 0.45e5.*m_cooldot(T_cell, p_air, j_0, ECSA, R_eq,
    R_Pt, I, I_max, h, N_cells, d_Tc)/3.7896;
%Pumping power coolant [W]
Pc_pump             = @(T_cell, p_air, j_0, ECSA, R_eq, R_Pt, I, I_max, h,
     N_cells, d_Tc) delta_p_cool(T_cell, p_air, j_0, ECSA, R_eq, R_Pt, I
    , I_max, h, N_cells, d_Tc).*m_cooldot(T_cell, p_air, j_0, ECSA, R_eq
    , R_Pt, I, I_max, h, N_cells, d_Tc)./(eta_pump*rho_cool);
%Radiator-side cooling system weight
m_rad               = @(T_cell, p_air, j_0, ECSA, R_eq, R_Pt, I, h,
    N_cells) (0.407/1000*Q_fcs(T_cell, p_air, j_0, ECSA, R_eq, R_Pt, I,
    I_max, h, N_cells) + 1.504)*(80-40)/(T_cell-273.15-40);

%% Calculate efficiency
%% Find max. net power output at sea-level (initial calculation before
    for-loop)
h_flight            = 0;
```

```
V_cell_vec          = getV_cell(T_cell, pair, j_0_vec/A_cell, ECSA, R_eq,
    R_Pt);
%Adjust for complex numbers (only consider real part of vectors)
V_cell_vec          = real(V_cell_vec(abs(imag(V_cell_vec)) < 0.00001));
j_0_vec             = j_0_vec(1:length(V_cell_vec));
P_cell_vec          = V_cell_vec.*j_0_vec;
P_cell_comp_vec     = P_comp(j_0_vec, I_max, 1, h_flight, ECSA, pair, R_eq
    , R_Pt);
P_cell_exp_vec      = P_exp(T_cell, j_0_vec, 1, h_flight, pair);
P_cell_pump_vec     = Pc_pump(T_cell, pair, j_0_vec/A_cell, ECSA, R_eq,
    R_Pt, j_0_vec, I_max, h_flight, 1, d_Tc) + Prad_pump(T_cell, pair,
    j_0_vec/A_cell, ECSA, R_eq, R_Pt, j_0_vec, h_flight, 1);
P_cell_other_vec    = 0;
P_cell_aux_vec      = max(P_cell_comp_vec - P_cell_exp_vec, 1000/455) +
    P_cell_pump_vec + P_cell_other_vec;
P_cell_net_vec      = max(P_cell_vec-P_cell_aux_vec,1e-3);
eff_stack_vec       = V_cell_vec/V_LHV;
eff_fcs_vec         = eff_stack_vec.*P_cell_net_vec./P_cell_vec;
[P_cell_net_max, Pmax_indx_0]       = max(P_cell_net_vec);
Pmax_indx = Pmax_indx_0;
P_cell_net_0 = P_cell_net_vec; %save inital vector

%% Relevant parameters
p_comp                          = 533;        %[W_comp/kg]
p_cool                          = 3410;       %[W_heat/kg] Based on
    Ballard FCS.
P_FC_max                        = max(P_load_fc_sample);

m_fcs_optimal = inf; m_fcs_hex_opt = 1e10;
for iti = 1:length(N_cells_vec)
    N_cells = N_cells_vec(iti);
    P_cell_prof         = P_load_fc_sample/N_cells;
if N_cells*P_cell_net_max < P_FC_max
    tot_fcs_mass_vec(iti) = NaN;
    continue;
end
for it = 1:length(P_cell_prof)
    if abs(altitude_vec_sample(it)-h_flight)>250
h_flight            = altitude_vec_sample(it);
P_cell_comp_vec     = P_comp(j_0_vec, I_max, 1, h_flight, ECSA, pair, R_eq
    , R_Pt);
P_cell_exp_vec      = P_exp(T_cell, j_0_vec, 1, h_flight, pair);
P_cell_pump_vec     = Pc_pump(T_cell, pair, j_0_vec/A_cell, ECSA, R_eq,
    R_Pt, j_0_vec, I_max, h_flight, 1, d_Tc);
P_cell_aux_vec      = max(P_cell_comp_vec - P_cell_exp_vec, 1000/455) +
    P_cell_pump_vec + P_cell_other_vec;
P_cell_net_vec      = max(P_cell_vec-P_cell_aux_vec,1e-3);
```

```
[~, Pmax_indx]     = max(P_cell_net_vec);
eff_fcs_vec        = eff_stack_vec.*P_cell_net_vec./P_cell_vec;
    end
[~, indx]          = min(abs(P_cell_net_vec(1:Pmax_indx)-P_cell_prof(it))
   ); %Make sure to avoid operation beyond MPP.
V_cell_prof(it)    = V_cell_vec(indx);
i_fc_prof(it)      = j_0_vec(indx);
P_fc_prof(it)      = P_cell_net_vec(indx)*N_cells;
eff_prof(it)       = eff_fcs_vec(indx);
end
%% Cooling
[I_mpp, t_indx]    = max(i_fc_prof);
Q_fcs_max          = Q_fcs(T_cell, pair, I_mpp/A_cell, ECSA, R_eq, R_Pt,
   I_mpp, I_max, altitude_vec_sample(t_indx), N_cells);
%% Compression
P_comp_prof              = P_comp(i_fc_prof, I_max, N_cells,
   altitude_vec_sample, ECSA, pair, R_eq, R_Pt)-P_exp(T_cell, i_fc_prof
   , N_cells, altitude_vec_sample, pair);
%% Estimate mass
m_fc                     = N_cells/455*42; %P Stack = 42 kg
m_comp                   = max(P_comp_prof)/p_comp;
m_cool                   = Q_fcs_max/p_cool;
E_rq_h2                  = trapz(t_vec_sample, P_load_fc_sample./eff_prof
   )/3600;
[m_h2, m_tank, ~, ~]     = get_h2_and_tank_mass(E_rq_h2, 1.0, geometry,
   type, fuel_margin);
m_fcs_hex                = (0.407/1000*Q_fcs_max + 1.504)*(80-40)/(80-40)
   ;
m_fcs_comps              = [m_fc, m_comp, m_cool, m_h2, m_tank];
oversize_factor          = N_cells*P_cell_net_max/P_FC_max;
if sum(m_fcs_comps)+m_fcs_hex < m_fcs_optimal+m_fcs_hex_opt &&
   oversize_factor >= 1
    m_fcs_optimal        = sum(m_fcs_comps);
    m_fcs_comps_opt      = m_fcs_comps;
    oversize_factor_opt  = oversize_factor;
    Q_fcs_max_opt        = Q_fcs_max;
    m_fcs_hex_opt        = m_fcs_hex;
    N_cells_opt          = N_cells;
    E_rq_h2_opt          = E_rq_h2;
    E_h2_tank_opt        = E_rq_h2*fuel_margin;
end
tot_fcs_mass             = sum(m_fcs_comps) + m_fcs_hex;
tot_fcs_mass_vec(iti)    = tot_fcs_mass;
end
m_fcs_comps     = m_fcs_comps_opt;
oversize_factor = oversize_factor_opt;
Q_fcs_max       = Q_fcs_max_opt;
```

```
end
```

F.2.1 Battery Sizing Script

This scripts calculates the required number of battery cells to meet the assigned power requirement for given hybridization factors.

```
function [m_batt, Q_heat_batt, E_batt_tot] = get_battery_mass_v2(
   t_vec_sample, P_load_batt, old_or_new, e_batt)
if sum(P_load_batt) == 0
    m_batt = 0; Q_heat_batt = 0; E_batt_tot = 0;
    return;
end
%% A123 LiFePO4 cell specifications (MathWorks)
cell2pack = 0.672;
Q_cell    = 2.3;
V_cell    = 3.3;
V_cutoff  = 2.475;
E_cell    = 3.4265;
R_cell    = 0.014;
A_cell    = 0.38019;
K_cell    = 0.00064489;
B_cell    = 26.5487;
i_max     = 70;
m_cell    = 70/1000; %[kg]

%% Functions
getN_ser  = @(V_tot) V_tot/V_cell;
getN_par  = @(Q_tot) Q_tot/Q_cell;
R         = @(N_ser, N_par) R_cell*N_ser/N_par;
Q         = @(N_par) Q_cell*N_par;
E         = @(N_ser) E_cell*N_ser;
A         = @(N_ser) A_cell*N_ser;
getK      = @(N_ser, N_par) K_cell*N_ser/N_par;
getB      = @(N_par) B_cell/N_par;
%% Battery requirements
V_tot     = 1000;
E_rq      = trapz(t_vec_sample, P_load_batt)/3600;
margin_Q  = 1;
m_step    = 0.01;
Q_tot     = E_rq/V_tot*margin_Q; %Minimum capacity requirement
%% Create vectors
i_prof    = zeros(1, length(t_vec_sample));
V_prof    = zeros(1, length(t_vec_sample));
%% Find initial cell number
N_ser     = getN_ser(V_tot);
N_par     = getN_par(Q_tot);
```

```
while  min(V_prof)/N_ser < V_cutoff || q_used > 0.999*Q_tot || max(
    i_prof) > i_max*N_par || max(P_prof-P_load_batt) > 10e3
q_used    = 0.01*Q_tot;
Q_tot     = Q_tot*margin_Q;
margin_Q  = margin_Q+m_step;
N_par     = getN_par(Q_tot);
R_tot     = R(N_ser, N_par);
K         = getK(N_ser, N_par);
B         = getB(N_par);
Q_tot     = Q(N_par);
E_tot     = E(N_ser);
A_tot     = A(N_ser);
V_batt    = @(q_used, i_f, i) E_tot - K*Q_tot/(Q_tot-q_used)*q_used -
    R_tot*i + A_tot*exp(-B*q_used) - K*Q_tot/(Q_tot-q_used)*i_f;
t_step    = t_vec_sample(2)-t_vec_sample(1);
%% Create vectors
i_prof        = zeros(1, length(t_vec_sample));
V_prof        = zeros(1, length(t_vec_sample));
P_loss        = zeros(1, length(t_vec_sample));
SOC_prof      = zeros(1, length(t_vec_sample));
q_used_vec    = zeros(1, length(t_vec_sample));
i_range       = [0:1:i_max*N_par];
for iter = 1:length(t_vec_sample)
    [~, indx]         = min(abs(V_batt(q_used, i_range, i_range).*i_range
        -P_load_batt(iter)));
    i                 = i_range(indx);
    %% NEW LINE:
    i_f = i;
    i_prof(iter)      = i;
    V_prof(iter)      = V_batt(q_used, i_f, i);
    SOC_prof(iter)    = (Q_tot-q_used)/Q_tot*100;
    q_used            = q_used+i*t_step/3600;
    q_used_vec(iter)  = q_used;
    P_loss(iter)      = max(R_tot*i^2, (E(N_ser)-V_prof(iter))*i);
end
P_prof    = V_prof.*i_prof;
end
%% Output
m_batt           = (N_par*N_ser)*m_cell/cell2pack;
Q_heat_batt      = max(P_loss);
E_batt_tot       = Q_tot*V_tot;
end
```

Bibliography

[1] H. Schefer, L. Fauth, T. H. Kopp, R. Mallwitz, J. Friebe, and M. Kurrat, "Discussion on electric power supply systems for all electric aircraft," *IEEE Access*, vol. 8, pp. 84188–84216, 2020.

[2] A. Schäfer, S. Barrett, K. Doyme, L. Dray, A. Gnadt, R. Self, A. O'Sullivan, A. Synodinos, and A. Torija, "Technological, economic and environmental prospects of all-electric aircraft," *Nature Energy*, vol. 4, 02 2019.

[3] "Fch2 ju, clean sky 2 study on hydrogen powered aviation," *Fuel Cells Bulletin*, vol. 2020, no. 7, pp. 5–6, 2020.

[4] Airbus, "Airbus reveals new zero-emission concept aircraft." Toulouse, France: September 2020.

[5] "Zeroavia conducts uk's first commercial-scale electric flight with hyflyer test at cranfield," *Fuel Cells Bulletin*, vol. 2020, no. 6, p. 1, 2020.

[6] DOE, "3.4 Fuel Cells," 2016. US Department of Energy: Multi-Year Research, Development, and Demonstration Plan, 2016.

[7] T. Kadyk, C. Winnefeld, R. Hanke-Rauschenbach, and U. Krewer, "Analysis and design of fuel cell systems for aviation," *Energies*, vol. 11, 02 2018.

[8] T. Kadyk, R. Schenkendorf, S. Hawner, B. Y1ld1z, and U. Römer, "Design of fuel cell systems for aviation: Representative mission profiles and sensitivity analyses," *Frontiers in Energy Research*, vol. 7, 2019.

[9] J. Kammermann, I. Bolvashenkov, K. Tran, H. G. Herzog, and I. Frenkel, "Feasibility study for a full-electric aircraft considering weight, volume, and reliability requirements," in *2020 International Conference on Electrotechnical Complexes and Systems (ICOECS)*, pp. 1–6, 2020.

[10] B. Jux, S. Foitzik, and M. Doppelbauer, "A standard mission profile for hybrid-electric regional aircraft based on web flight data," in *2018 IEEE International Conference on Power Electronics, Drives and Energy Systems (PEDES)*, pp. 1–6, 2018.

[11] J. M. Collins and D. McLarty, "All-electric commercial aviation with solid oxide fuel cell-gas turbine-battery hybrids," *Applied Energy*, vol. 265, p. 114787, 2020.

[12] NCE MARITIME CLEANTECH, "Norwegian future value chains for liquid hydrogen," 2019. [Accessed 9-June-2021].

[13] E. Rivard, M. Trudeau, and K. Zaghib, "Hydrogen storage for mobility: A review," *Materials*, vol. 12, no. 12, 2019.

[14] "Hydrogen Storage," 2017. US Department of Energy: Energy Efficiency Renewable Energy.

[15] "Target Explanation Document: Onboard Hydrogen Storage for Light-Duty Fuel Cell Vehicles." US Department of Energy: Energy Efficiency Renewable Energy.

[16] V. Fredheim, *International Conference on Marine Renewable Energy and Maritime Hydrogen Technology*. HEXAGON, 2018.

[17] A. Züttel, "Materials for hydrogen storage," *Materials Today*, vol. 6, no. 9, pp. 24–33, 2003.

[18] M. Gardiner, "Energy requirements for hydrogen gas compression and liquefaction as related to vehicle storage needs," 2009. US Department of Energy: Hydrogen and Fuel Cells Program Record.

[19] D. Berstad, G. Skaugen, and Ø. Wilhelmsen, *Concepts for efficient hydrogen liquefaction*. SINTEF and NTNU, 2019.

[20] T. P. Dever, K. Duffy, A. Provenza, P. L. Loyselle, B. Choi, C. Morrison, and A. M. Lowe, "Assessment of technologies for noncryogenic hybrid electric propulsion," 2015.

[21] J. K. Nøland, "Hydrogen electric airplanes: A disruptive technological path to clean up the aviation sector," *IEEE Electrification Magazine*, vol. 9, pp. 92–102, 03 2021.

[22] A. F. Nygaard, "A preliminary study on pem fuel cells for aircraft applications," project report in TET4520, Department of Electric Power Engineering, NTNU – Norwegian University of Science and Technology, Dec. 2020.

[23] X.-Z. Yuan and H. Wang, *PEM Fuel Cell Fundamentals*, pp. 1–87. London: Springer London, 2008.

[24] S. Tong, D. Qian, and C. Huo, *Hydrogen-Air PEM Fuel Cell : Integration, Modeling, and Control*. De Gruyter, 2018.

[25] D. A. Kabza, "Fuel cell formulary," 12 2020. `http://pemfc.de/FCF_A4.pdf`.

[26] A. Kneer, J. Jankovic, D. Susac, A. Putz, N. Wagner, M. Sabharwal, and M. Secanell, "Correlation of changes in electrochemical and structural parameters due to voltage cycling induced degradation in pem fuel cells," *Journal of The Electrochemical Society*, vol. 165, pp. F3241–F3250, 01 2018.

[27] P. Zihrul, I. Hartung, S. Kirsch, G. Huebner, F. Hasché, and H. A. Gasteiger, "Voltage cycling induced losses in electrochemically active surface area and in h2/air-performance of PEM fuel cells," *Journal of The Electrochemical Society*, vol. 163, no. 6, pp. F492–F498, 2016.

[28] A. Kneer and N. Wagner, "A semi-empirical catalyst degradation model based on voltage cycling under automotive operating conditions in PEM fuel cells," *Journal of The Electrochemical Society*, vol. 166, no. 2, pp. F120–F127, 2019.

[29] PowerCell Sweden, *PowerCellution P Stack*, 2021. Version. 121.

[30] L. M. Pant, M. R. Gerhardt, N. Macauley, R. Mukundan, R. L. Borup, and A. Z. Weber, "Along-the-channel modeling and analysis of pefcs at low stoichiometry: Development of a 1+2d model," *Electrochimica Acta*, vol. 326, p. 134963, 2019.

[31] K. Neyerlin, W. Gu, J. Jorne, and H. Gasteiger, "Determination of catalyst unique parameters for the oxygen reduction reaction in a pemfc," *Journal of The Electrochemical Society*, vol. 153, pp. A1955–A1963, 10 2006.

[32] F. Barbir, "Chapter five - fuel cell operating conditions," in *PEM Fuel Cells (Second Edition)* (F. Barbir, ed.), pp. 119–157, Boston: Academic Press, second edition ed., 2013.

[33] F. Barbir, "Chapter three - fuel cell electrochemistry," in *PEM Fuel Cells (Second Edition)* (F. Barbir, ed.), pp. 33–72, Boston: Academic Press, second edition ed., 2013.

[34] M. L. Perry, "Chapter eleven - durability of polymer electrolyte fuel cells," in *PEM Fuel Cells (Second Edition)* (F. Barbir, ed.), pp. 435–467, Boston: Academic Press, second edition ed., 2013.

[35] F. Barbir, "Chapter nine - fuel cell system design," in *PEM Fuel Cells (Second Edition)* (F. Barbir, ed.), pp. 305–372, Boston: Academic Press, second edition ed., 2013.

[36] M. H. Bargal, M. A. Abdelkareem, Q. Tao, J. Li, J. Shi, and Y. Wang, "Liquid cooling techniques in proton exchange membrane fuel cell stacks: A detailed survey," *Alexandria Engineering Journal*, vol. 59, no. 2, pp. 635–655, 2020.

[37] S. Yu and D. Jung, "Thermal management strategy for a proton exchange membrane fuel cell system with a large active cell area," *Renewable Energy*, vol. 33, no. 12, pp. 2540–2548, 2008.

[38] G. Romeo, E. Cestino, F. Borello, and G. Correa, "Engineering method for air-cooling design of two-seat propeller-driven aircraft powered by fuel cells," *Journal of Aerospace Engineering*, vol. 24, pp. 79–88, 2011.

[39] A. Carozza, *Heat Exchangers in the Aviation Engineering*. 04 2017.

[40] H. Kellermann, A. L. Habermann, and M. Hornung, "Assessment of aircraft surface heat exchanger potential," *Aerospace*, vol. 7, no. 1, 2020.

[41] R. Stroman, M. Schuette, and G. Page, "Cooling system design for pem fuel cell powered air vehicles," p. 51, 06 2010.

[42] NASA, *Earth Atmosphere Model Metric Units*, 2021. Nancy Hall, Glenn Research Center.

[43] P. Thounthong and P. Sethakul, "Analysis of a fuel starvation phenomenon of a pem fuel cell," in *2007 Power Conversion Conference - Nagoya*, pp. 731–738, 2007.

[44] A. Taniguchi, T. Akita, K. Yasuda, and Y. Miyazaki, "Analysis of electrocatalyst degradation in pemfc caused by cell reversal during fuel starvation," *Journal of Power Sources*, vol. 130, no. 1, pp. 42 – 49, 2004.

[45] "DOE Technical Targets for Fuel Cell System Humidifiers and Air Compression Systems." US Department of Energy: Energy Efficiency Renewable Energy. Retrieved 04 2021.

[46] O. Bethoux, "Hydrogen fuel cell road vehicles: State of the art and perspectives," *Energies*, vol. 13, p. 5843, 11 2020.

[47] PowerCell Sweden, *MS-100 Fuel Cell System - Technical description*. Datasheet.

[48] Z. Qi, *Electrochemical Methods for Catalyst Activity Evaluation*, pp. 547–607. London: Springer London, 2008.

[49] Eckert, Peter. (2019). "D6.3: Results from demonstration of the range extender." Zenodo.

[50] Oyarce Barnett, Alejandro. (2017). "D1.2: Protocols of experiments and validation activities." Zenodo.

[51] J. Li, *Catalyst Layer Degradation, Diagnosis and Failure Mitigation*, pp. 1041–1094. London: Springer London, 2008.

[52] T. Bednarek and G. Tsotridis, "Assessment of the electrochemical characteristics of a polymer electrolyte membrane in a reference single fuel cell testing hardware," *Journal of Power Sources*, vol. 473, p. 228319, 2020.

[53] D. Guilbert, A. Gaillard, A. Mohammadi, A. N'diaye, and A. Djerdir, "Investigation of the interactions between proton exchange membrane fuel cell and interleaved dc/dc boost converter in case of power switch faults," *International Journal of Hydrogen Energy*, vol. 40, pp. 519–537, 01 2015.

[54] M. Rubio, A. Urquia, R. Kuhn, and S. Dormido, "Electrochemical parameter estimation in operating proton exchange membrane fuel cells," *Journal of Power Sources*, vol. 183, no. 1, pp. 118 – 125, 2008.

[55] F. Zenith and S. Skogestad, "Control of fuel cell power output," *Journal of Process Control*, vol. 17, no. 4, pp. 333–347, 2007.

[56] R. Ferrero, M. Marracci, and B. Tellini, "Single pem fuel cell analysis for the evaluation of current ripple effects," *IEEE Transactions on Instrumentation and Measurement*, vol. 62, no. 5, pp. 1058–1064, 2013.

[57] G. Fontes, C. Turpin, S. Astier, and T. A. Meynard, "Interactions between fuel cells and power converters: Influence of current harmonics on a fuel cell stack," *IEEE Transactions on Power Electronics*, vol. 22, no. 2, pp. 670–678, 2007.

[58] B. Wahdame, L. Girardot, D. Hissel, F. Harel, X. Francois, D. Candusso, M. C. Pera, and L. Dumercy, "Impact of power converter current ripple on the durability of a fuel cell stack," in *2008 IEEE International Symposium on Industrial Electronics*, pp. 1495–1500, 2008.

[59] M. Gerard, J.-P. Poirot-Crouvezier, D. Hissel, and M.-C. Péra, "Ripple Current Effects on PEMFC Aging Test by Experimental and Modeling," *Journal of Fuel Cell Science and Technology*, vol. 8, 11 2010. 021004.

[60] F. Sergi, G. Brunaccini, A. Stassi, A. Di Blasi, G. Dispenza, A. Aricò, M. Ferraro, and V. Antonucci, "Pem fuel cells analysis for grid connected applications," *International Journal of Hydrogen Energy*, vol. 36, no. 17, pp. 10908 – 10916, 2011. International Conference on Hydrogen Production (ICH2P)-2010.

[61] R. S. Gemmen, "Analysis for the Effect of Inverter Ripple Current on Fuel Cell Operating Condition ," *Journal of Fluids Engineering*, vol. 125, pp. 576–585, 06 2003.

[62] H. M. Bye, "Investigation of a 200kw sic-based ibc for high-speed hydrogen ferries," master's thesis in TET4900, Department of Electric Power Engineering, NTNU – Norwegian University of Science and Technology, June 2019.

[63] X. Li, W. Zhang, H. Li, R. Xie, M. Chen, G. Shen, and D. Xu, "Power management unit with its control for a three-phase fuel cell power system without large electrolytic capacitors," *IEEE Transactions on Power Electronics*, vol. 26, no. 12, pp. 3766–3777, 2011.

[64] R. Bambang, A. Syaichu-Rohman, C. Dronkers, R. Ortega, and A. Sasongko, "Energy management of fuel cell/battery/supercapacitor hybrid power sources using model predictive control," *IEEE Transactions on Industrial Informatics*, vol. 10, 11 2014.

[65] R. C. Bolam, Y. Vagapov, and A. Anuchin, "Review of electrically powered propulsion for aircraft," in *2018 53rd International Universities Power Engineering Conference (UPEC)*, pp. 1–6, 2018.

[66] A. Hentunen, J. Forsström, S. Jenu, S. Tuurala, A. Manninen, and S. Bjarghov, "Battery techno-economics tool - d6.2 invade h2020," Mar. 2018.

[67] M. Warncke, S. Fahlbusch, and K. F. Hoffmann, "Dc/dc-converter for fuel cell integration in more electric aircraft applications," in *2017 19th European Conference on Power Electronics and Applications (EPE'17 ECCE Europe)*, pp. P.1–P.10, 2017.

[68] L. Palma and P. Enjeti, "Analysis of common mode voltage in fuel cell power conditioners connected to electric utility," in *2006 IEEE International Conference on Industrial Technology*, pp. 200–205, 2006.

[69] N. Langmaack, G. Tareilus, and M. Henke, "Sic boost converter with high power density for a battery electric sports car," 02 2014.

[70] R. Jansen, C. Bowman, A. Jankovsky, R. Dyson, and J. Felder, "Overview of nasa electrified aircraft propulsion research for large subsonic transports," 2017.

[71] G. Bravo, N. Praliyev, and Veress, "Performance analysis of hybrid electric and distributed propulsion system applied on a light aircraft," *Energy*, vol. 214, p. 15, 09 2020.

[72] H. Kim, A. Perry, and P. Ansell, "A review of distributed electric propulsion concepts for air vehicle technology," 07 2018.

[73] Ø. Arntsen, J. Reimers, and A. Hadhazy, "Introduction of electric aviation in norway," 2018.

[74] A. Kolli, A. Gaillard, A. De Bernardinis, O. Bethoux, D. Hissel, and Z. Khatir, "A review on dc/dc converter architectures for power fuel cell applications," *Energy Conversion and Management*, vol. 105, pp. 716–730, 2015.

[75] Bombardier, *Bombardier Q300*, 2006. Datasheet.

[76] J. Edgren, "Blir det största vätgasdrivna passagerarflygplanet i trafik." NyTeknik, 2020.

[77] M. F. Niţă, "Aircraft design studies based on the ATR 72," project work towards a thesis, Department of Automotive and Aeronautical Engineering, Hamburg University of Applied Sciences, June 2008.

[78] M. H. Sadraey, *Aircraft Design: A Systems Engineering Approach*, ch. 4, pp. 93–159. John Wiley Sons, Ltd.

[79] P. M. Sforza, "Direct calculation of zero-lift drag coefficients and (l/d)max in subsonic cruise," *Journal of aircraft*, vol. 57, no. 6, pp. 1224–1228, 2020.

[80] HandWiki, "Engineering:Bombardier Dash 8," 2021. [Accessed 3-June-2021].

[81] EASA, *Type-certificate data sheet*, 2019. De Havilland Aircraft Company of Canada.

[82] D. R. Stroebel, "Approach to Provide a Metallic Bipolar Plate Module to the Industry," 2017. [Accessed 8-June-2021].

[83] D. T. Tingelöf, "Hydrogen fuel cells in transport applications," 2017. [Accessed 8-June-2021].

[84] B. D. James, J. M. Huya-Kouadio, and C. Houchins, "2017 DOE Hydrogen and Fuel Cells Program Review - Fuel Cell Systems Analysis," 2017. [Accessed 8-June-2021].

[85] O. Gröger, H. Gasteiger, and P. Suchsland, "Review—electromobility: Batteries or fuel cells?," *Journal of The Electrochemical Society*, vol. 162, pp. A2605–A2622, 01 2015.

[86] J. Litt, D. Frederick, and T.-H. Guo, "The case for intelligent propulsion control for fast engine response," *AIAA Infotech at Aerospace Conference and Exhibit and AIAA Unmanned...Unlimited Conference*, 04 2009.

[87] F. Cells and H. J. Undertaking, "STATE-OF-THE-ART AND FUTURE TARGETS (KPIS)," 2017. [Accessed 9-June-2021].

[88] Nedstack, *NEDSTACK FCS 10-XXL PEM FUEL CELL STACK*, 2019. Datasheet: Version: November 2019.

[89] J. W. Chapman, H. Hasseeb, and S. Schnulo, "Thermal management system design for electrified aircraft propulsion concepts," in *2020 AIAA/IEEE Electric Aircraft Technologies Symposium (EATS)*, pp. 1–23, 2020.

[90] Ballard, *Fuel Cell Power Module for Heavy Duty Motive Applications*, 2018. Datasheet: FCveloCity-HD.

[91] PowerCell Sweden, *PowerCellution Heavy Duty System 100*, 2021. Datasheet: Version. 121.

[92] M. Boll, M. Corduan, S. Biser, M. Filipenko, Q. H. Pham, S. Schlachter, P. Rostek, and M. Noe, "A holistic system approach for short range passenger aircraft with cryogenic propulsion system," *Superconductor Science and Technology*, vol. 33, p. 044014, mar 2020.

[93] J. Pratt, J. Brouwer, and G. Samuelsen, "Performance of proton exchange membrane fuel cell at high-altitude conditions," *Journal of Propulsion and Power - J PROPUL POWER*, vol. 23, pp. 437–444, 03 2007.

[94] T. Hordé, P. Achard, and R. Metkemeijer, "Pemfc application for aviation: Experimental and numerical study of sensitivity to altitude," *International Journal of Hydrogen Energy*, vol. 37, no. 14, pp. 10818–10829, 2012.

[95] TOYOTA, *Challenging toward the realization of a hydrogen-based society*. Toyota Industries Corporation, 2014.

[96] C. Winnefeld, T. Kadyk, B. Bensmann, U. Krewer, and R. Hanke-Rauschenbach, "Modelling and designing cryogenic hydrogen tanks for future aircraft applications," *Energies*, vol. 11, no. 1, 2018.

[97] N. Manthey, "Zeroavia completes maidenflight with hydrogen aircraft." Electrive.com, 2020.

[98] A123 SYSTEMS, *High Power Lithium Ion ANR26650M1*, 2006. MD100001-001.

[99] MathWorks®, "Generic battery model." Simscape Electrical, Battery (R2021a).

[100] O. Tremblay and L.-A. Dessaint, "Experimental validation of a battery dynamic model for ev applications," *World Electric Vehicle Journal*, vol. 3, no. 2, pp. 289–298, 2009.

[101] H. Löbberding, S. Wessel, C. Offermanns, M. Kehrer, J. Rother, H. Heimes, and A. Kampker, "From cell to battery system in bevs: Analysis of system packing efficiency and cell types," *World Electric Vehicle Journal*, vol. 11, pp. 1–16, 12 2020.

[102] *ANR26650M1-B, LithiumWerks Nanophosphate® 3.3V 2.5Ah Lithium Iron Phosphate Battery*, 2021.

[103] BloombergNEF, *Battery Pack Prices Cited Below $100/kWh for the First Time in 2020, While Market Average Sits at $137/kWh*, 12 2020.

[104] B. G. Pollet, S. S. Kocha, and I. Staffell, "Current status of automotive fuel cells for sustainable transport," *Current Opinion in Electrochemistry*, vol. 16, pp. 90–95, 2019. Electrochemical Materials and Engineering • Sensors and Biosensors.

[105] D. Sartori, G. Catalano, M. Genco, C. Pancotti, E. Sirtori, S. Vignetti, and C. D. Bo, "Guide to cost-benefit analysis of investment projects. economic appraisal tool for cohesion policy 2014-2020," 2014.

[106] Hydrogen Council, "Path to hydrogen competitiveness - A cost perspective," 2020. [Accessed 8-June-2021].

[107] P. Thounthong, S. Raël, B. Davat, and I. Sadli, "A control strategy of fuel cell/battery hybrid power source for electric vehicle applications," in *2006 37th IEEE Power Electronics Specialists Conference*, pp. 1–7, 2006.

[108] Federal Aviation Administration, *Power or Thrust Response*, 2011. Title 14, Part 33.73.

[109] P. Gazdzicki, J. Mitzel, A. Dreizler, M. Schulze, and K. Friedrich, "Impact of platinum loading on performance and degradation of polymer electrolyte fuel cell electrodes studied in a rainbow stack," *Fuel Cells*, vol. 18, 10 2017.

[110] European Aviation Safety Agency, "Notice of Proposed Amendment 2016-06 (C) - Fuel planning and management ," 2016, url =.

[111] T. Fletcher and K. Ebrahimi, "The effect of fuel cell and battery size on efficiency and cell lifetime for an l7e fuel cell hybrid vehicle," *Energies*, vol. 13, p. 5889, 11 2020.

[112] J.-S. Kim, D.-c. Lee, J.-J. Lee, and C. Kim, "Optimization for maximum specific energy density of a lithium-ion battery using progressive quadratic response surface method and design of experiments," *Scientific reports*, vol. 10, p. 15586, 09 2020.

[113] C. Bonnet, L. Franck-Lacaze, B. Huang, Y. Chatillon, G. Valentin, and F. Lapicque, "Aging of polymer electrolyte membrane fuel cells (pemfc): General features and investigation of two typical examples," *Journal of Applied Electrochemistry*, vol. 42, 09 2012.

[114] R. Ma, Z. Li, E. Breaz, C. Liu, H. Bai, P. Briois, and F. Gao, "Data-fusion prognostics of proton exchange membrane fuel cell degradation," *IEEE Transactions on Industry Applications*, vol. 55, no. 4, pp. 4321–4331, 2019.

[115] E. Breaz, F. Gao, A. Miraoui, and R. Tirnovan, "A short review of aging mechanism modeling of proton exchange membrane fuel cell in transportation applications," in *IECON 2014 - 40th Annual Conference of the IEEE Industrial Electronics Society*, pp. 3941–3947, 2014.

[116] S. Touhami, L. Dubau, J. Mainka, J. Dillet, M. Chatenet, and O. Lottin, "Anode aging in polymer electrolyte membrane fuel cells i: Anode monitoring by electrochemical impedance spectroscopy," *Journal of Power Sources*, vol. 481, p. 228908, 2021.

[117] J. Zhang and J. Zhang, *Catalyst Layer/MEA Performance Evaluation*, pp. 965–1002. London: Springer London, 2008.

[118] W. Liu and D. Zuckerbrod, "In situ detection of hydrogen peroxide in PEM fuel cells," *Journal of The Electrochemical Society*, vol. 152, no. 6, p. A1165, 2005.

[119] J. Kim, J. Lee, and B. H. Cho, "Equivalent circuit modeling of pem fuel cell degradation combined with a lfrc," *IEEE Transactions on Industrial Electronics*, vol. 60, no. 11, pp. 5086–5094, 2013.

[120] S. Ye, *Reversal-tolerant Catalyst Layers*, pp. 835–860. London: Springer London, 2008.

[121] Z. Jiang, L. Gao, and R. A. Dougal, "Adaptive control strategy for active power sharing in hybrid fuel cell/battery power sources," *IEEE Transactions on Energy Conversion*, vol. 22, no. 2, pp. 507–515, 2007.

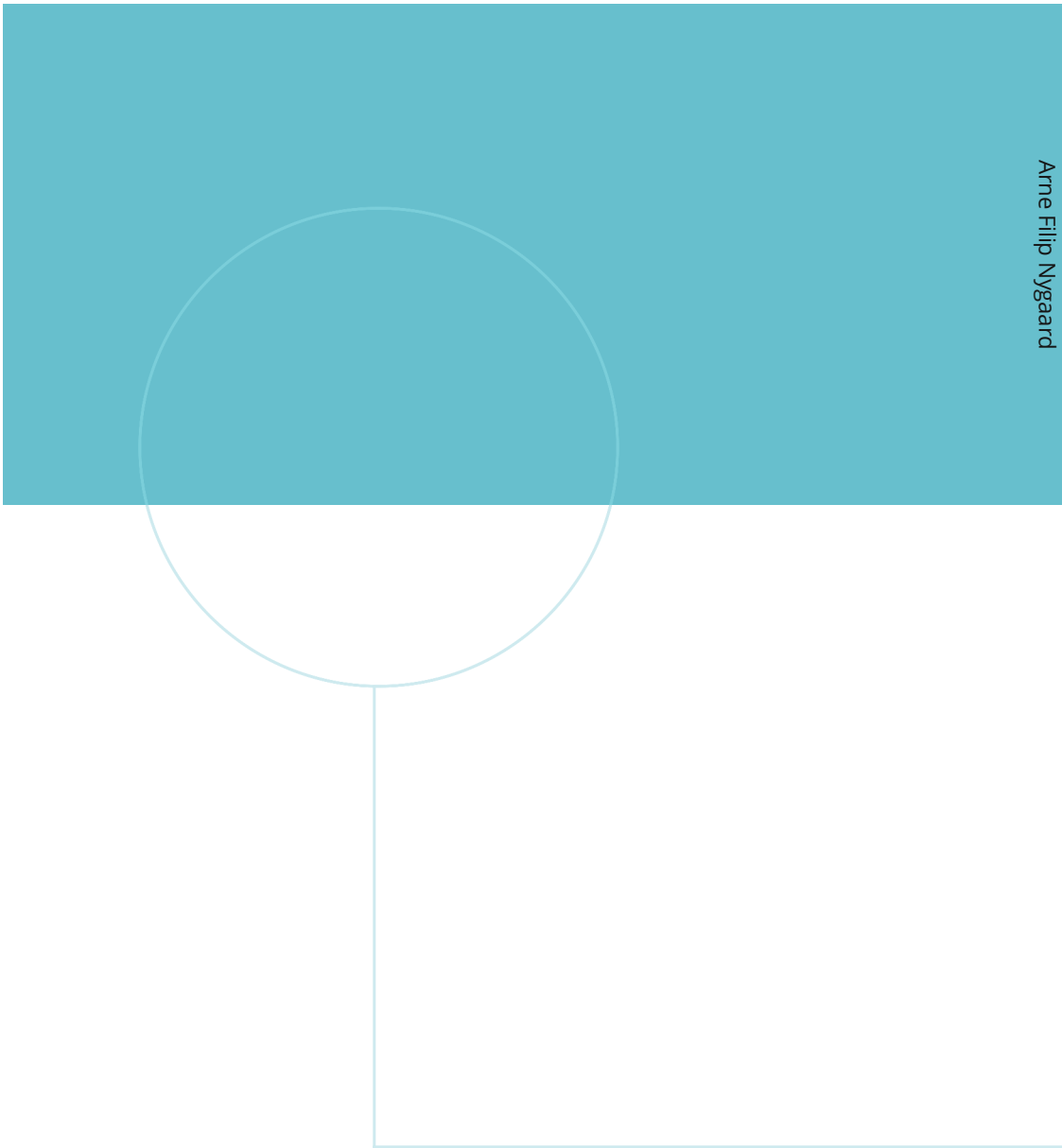

Arne Filip Nygaard

NTNU
Norwegian University of
Science and Technology